Reduced model of macro-scale stochastic plasticity identification by Bayesian inference: Application to quasi-brittle failure of concrete

Adnan Ibrahimbegovic, Hermann G. Matthies, Emir Karavelić

Version of Record: https://www.sciencedirect.com/science/article/pii/S0045782520306137
Manuscript_7e33933a23ce626316bcf00fc2de9a54

Reduced model of macro-scale stochastic plasticity identification by Bayesian inference in application to quasi-brittle failure of concrete

Adnan Ibrahimbegovic[a,b,*], Hermann G. Matthies[c], Emir Karavelić[a,d]

[a] *Université de Technologie de Compiègne - Alliance Sorbonne Université, Laboratoire Roberval de Mécanique, Centre de Recherche Royallieu, 60200 Compiègne, France*
[b] *Institut Universitaire de France (IUF)*
[c] *Institute of Scientific Computing, Technische Universität Braunschweig, 38092 Braunschweig, Germany*
[d] *University of Sarajevo, Faculty of Civil Engineering, 71000 Sarajevo, Bosnia and Herzegovina*

Abstract

In this paper we deal with a probability-based scale bridging for concrete material when passing the detailed information at the meso-scale (the scale where the aggregate vs. cement microstructure is visible) with a Voronoi-cell based microstructure representation towards the chosen reduced model at the macro-scale (the scale where the concrete is a homogenized continuum) with a stochastic plasticity model for localized failure. This is accomplished by using Bayesian inference providing the probability distributions of the macro-scale model parameters expressed as random variables (RV) in order to compensate for the model reduction from the meso-scale, where parameters are expressed as random fields (RF). The original aspect of this approach is in the resulting macro-scale stochastic plasticity model, which can best quantify the uncertainty due to data loss in terms of the corresponding probability distribution of its parameters. The proposed procedure is illustrated in detail for the concrete meso-scale model presented in Part I of this paper (see [41]), both for the simple elastic response, as well as for the plastic response with hardening in the fracture process zone (FPZ), followed by a softening response in the localized failure phase. This context of localized failure implies that the classical homogenization procedure no longer applies, and should be replaced by a macro-scale reduced model defined with respect to a quantity of interest (QoI), which is not necessarily the same for each particular response phase. The complete set of results for the parameter identification are combined together at the macro-scale in terms of a solid finite element with embedded discontinuity (ED-FEM), granting it very powerful predictive properties. The particular choice of ED-FEM for the macro-scale reduced model allows one to compute the QoI at an element-level, either as strain energy for the elastic response, or as plastic dissipation for each failure mode. Thus, the Bayesian inference computation of the probability distributions of the RVs representing the macro-scale model parameters, performed by matching such QoI results computed for the macro-scale and the meso-scale models, reduces to a homogenization-type procedure within a probabilistic setting that can successfully handle any case where the separation of scales no longer applies.

Keywords: stochastic plasticity, model reduction with Bayesian inference, parameter probability distribution, concrete model with full-set of 3D failure modes, localized failure, finite element with embedded discontinuity

Abbreviations (in alphabetic order): ED-FEM — finite element method with embedded discontinuity ; FPZ — fracture process zone ; GMKF — Gauss-Markov-Kálmán filter ; KLE — Karhunen-Loève expansion ; MCMC — Markov Chain Monte Carlo ; PCE — Polynomial Chaos Expansion ; POD — proper orthogonal decomposition ; QoI — Quantity of Interest ; RF — random field ; RV — random variable

1. Introduction and motivation

Of special interest for this work are stochastic models that can capture localized failure sensitivity to initial and induced defects for structures built of heterogeneous composite material, such as concrete. The potential scientific

*Corresponding author

gain provided by such models is in better prediction of crack spacing and opening, which can be used to improve concrete durability. The latter is of direct interest and benefit to many industrial applications, given that concrete is probably the most used material in construction and that many such structures are rapidly ageing. From the standpoint of constructing predictive stochastic plasticity fracture models, this kind of composite material has rather favorable features with: two-phase microstructure with aggregate vs. cement paste visible at meso-scale, non-local dimension brought by typical fracture modes of massive structures with significant contribution of the fracture process zone (FPZ), and a fabrication that is comparable to large-scale additive-manufacturing, where the complete structure is cast with the same material rather than an assembly of various components. The latter is the crucial hypothesis to make the proposed macro-scale stochastic plasticity model feasible in terms of predicting probability-distribution-based estimates of structure properties.

Although upscaling has been considered, especially in the form of homogenization for reversible behaviour already for a long time, cf. for an account from a mathematical [80] resp. mechanical side [103], next to periodic also for heterogeneous media (e.g. [95, 10]), and also for cement-based composites (e.g. [98, 99]), the main novelty here is seen in the fact that all scales are to be treated probabilistically, and our approach is to capture not only the average response on the larger scale. In fact, one purpose here is to be able to reflect the meso-scale variability — also here termed *aleatoric uncertainty* — as well as possible on the macro-scale. This is particularly important for the testing of heterogeneous cement-based composites, where the scales in the test specimen are in general not well separated. Such is the case when testing reduced-size specimen with respect to meso-structure heterogeneities, where significant variability occurs in the test results due to small-scale uncertainty [93]. Yet, more important for these quasi-brittle composite materials is the fracture sensitivity to small-scale defects that trigger crack coalescence and accelerate structural failures. This is especially visible under non-proportional loading (e.g. see [12] with simulation results for the Nooru-Mohamed test on a double-edge notched specimen), where only fine-scale models representing material heterogeneities can provide sufficiently predictive results, whereas those based upon homogenization, employing average properties, typically fail predictions in the tests where several failure mechanisms are active (e.g. see [22] and references therein). Therefore, despite ample literature (e.g. see [28] or [61] for a summary), the fully predictive macro-scale model for localized failure of concrete remains a somewhat elusive goal, due to a number of uncertainties that influence the nonlinear response.

In this work, which continues the development of [26, 27, 36, 56, 81, 77, 83, 82, 84], we focus in particular on the uncertainty propagation across the scales, which allows to connect the inelasticity at multiple scales, starting from the fine scale (here the meso-scale for concrete) where the heterogeneous composite failure mechanisms and the variability of model parameters can be captured much better by a corresponding representation of different phases (here aggregate vs. cement paste). The main goal is to provide a corresponding macro-scale reduced model, which can significantly increase the computational efficiency and make the analysis of complex structures feasible. The proposed approach can be considered as a part of a scale-coarsening strategy, but much different from ad-hoc choices ([4]). Namely, once the crack pattern at the meso-scale has stabilized, we will use an efficient Bayesian updating, replacing subsequently the meso-scale, where the heterogeneity is modelled by random fields (RFs), by a macro-scale generalized ED-FEM element where the parameters of the material model are random variables (RVs). The stochastic variability of the parameters on the coarse or macro-scale reflect the aleatoric uncertainty of the fine or meso-scale as it is visible on the macro scale, as well as the epistemic uncertainties of the modeling error involved by fixing a type of continuum mechanics model on the macro scale for the purpose of model reduction, the loss of spatial resolution, and any other epistemic errors involved in the upscaling and identification procedure. With such an approach one can recover a probabilistic reduced model on the macro-scale that defines the probability distributions of the fracture parameters describing localized failure with both volume and surface dissipation ([34], [32]). Such a 'mechanics-based' model reduction is fundamentally different from the vast majority of recent works ([9, 66, 8, 46, 48]) using statistical modes with either POD—proper orthogonal decomposition or PGD—proper generalized decomposition. Moreover, one can recover any probability distribution of structure failure modes for advanced safety evaluations, contrary to pre-defined distributions currently used: log-normal distribution to construct fragility curves ([87]), uniform to construct bounds ([45]), Weibull to account for weakest link failure ([47]), or ad-hoc combination of power law and Gaussian as two asymptotic values ([3]).

One may note that providing a Reduced Order Model (ROM) by Bayesian inference is an original approach to coarse-scaling, resulting in a novel concept of quantifying uncertainty through inelasticity at multiple scales. This is an off-line probability computation that uses efficient Bayesian updates with many realizations to assimilate information

on the microstructure evolution, obtained by either simulations or measurements, in order to provide probability distribution of coarse-scale fracture parameters expressed as RVs or RFs. Higher computational efficiency is obtained by a polynomial chaos spectral version of the Gauss-Markov-Kálmán filter (GMKF) [67, 74, 68, 69] that simplifies these Bayesian updates. This is a generalization [57, 58] of the classical Kálmán filter (KF) [40] to nonlinear and non-Gaussian situations, without the assumptions of Gaussianity which are used in other variants like the Monte Carlo sampling based Ensemble Kálmán filter (EnKF) [19, 20]. It is important to note that such a ROM is not seeking to provide a detailed representation of microstructure initial defects, but only their effects on a Quantity-of-Interest (QoI), here typically either stored energy or dissipation. Similar off-line probability computations are also used for an original scale-coarsening strategy, which can account for induced defects during a particular loading program in order to provide a mechanics-based model reduction; the proposed reduced model can replace stabilized meso-scale crack patterns by a generalized ED-FEM model with parameters (element arrays) defined as RVs or RFs.

Our main focus in this work is on the model reduction from meso-scale to macro-scale, which defines a generalized ED-FEM in a probability framework, and allows for stochastic coarse graining. This is illustrated in switching from meso-scale to macro-scale, in order to provide a replacement with a generalized ED-FEM once the crack pattern inside the corresponding meso-scale element is stabilized. Namely, the goal is to then replace the meso-scale computation with the corresponding stochastic macro-scale model of such an ED-FEM. We will illustrate this idea on a plasticity model, where such parameters also include yield stress (for defining the fracture process zone — FPZ) and ultimate stress (for defining localized failure).

Two different methods for Bayesian inference have been tested and compared in the proposed approach, both based on Bayes's theorem that allows incorporating new information generated in a particular loading program. Each unknown parameter of the reduced model is modeled as a random variable. Such a description has two constituents, the measurable function representing the random variable RV, and the measure. Markov chain Monte Carlo (MCMC) (e.g. [23, 21]) updates the measure, whereas the various filters (e.g. [40, 74, 69, 19]) change resp. update the measurable function. We formulate both methods as functional spectral approximations of stochastic problems, and introduce especially in combination with the second method a new procedure which does not need any sampling, hence works with the subsequent update in a deterministic manner. It also seems to be the fastest and more reliable when compared with other methods. We show by example that the spectral resp. polynomial chaos version of the GMKF also works for highly nonlinear non-smooth problems with non-Gaussian measures.

The outline of the paper is as follows: In Section 2 we briefly describe the meso-scale of [41], and then propose its extension to the case when the model parameters are defined as random fields (RF). In Section 3, we present the macro-scale plasticity model for concrete, and indicate its transformation to the stochastic plasticity case. Considerations of Bayesian inference being used for the inverse problem by a directly coupled mechanics-probability problem are given in Section 4. The results for several numerical examples are presented in Section 5. In Section 6 we state some closing remarks.

2. Plasticity at multiple scales: meso-scale model for failure analysis of concrete with parameters as random fields

2.1. Meso-scale model for failure analysis of concrete

In Part I of this paper ([41]) we developed a fine-scale constitutive model of concrete that can represent the complete set of 3D failure mechanisms. The price to pay is to start with the microstructure at a meso-scale that is able to distinguish between aggregate and cement paste and construct its Voronoi cell representation (see Figure 1) with cohesive links, which allows to explicitly handle the failure at the aggregate-cement interface.

The typical failure modes at the interface are described by multi-surface criteria set in a local frame:

$$\begin{aligned} \phi_{u,n+1} &:= t_{u,n+1} - (\sigma_{u,t} - q_{u,n}) \leq 0 \\ \phi_{v,n+1} &:= \left|t_{v,n+1}\right| - (\tau_{u,v} - q_{v,n}) \leq 0 \\ \phi_{w,n+1} &:= \left|t_{w,n+1}\right| - (\tau_{u,w} - q_{w,n}) \leq 0, \end{aligned} \tag{1}$$

where $\sigma_{u,t}$, $\tau_{u,v}$ and $\tau_{u,w}$ are the fracture stress values in mode I, mode II, and mode III, respectively. The variability of interface fracture parameters of the meso-scale model is here quantified in terms of random fields, $p(x,\omega) = \sigma_{u,t}(x,\omega)$, $\tau_{u,v}(x,\omega)$ and $\tau_{u,w}(x,\omega)$, with their probability distributions constructed as further explained in this section.

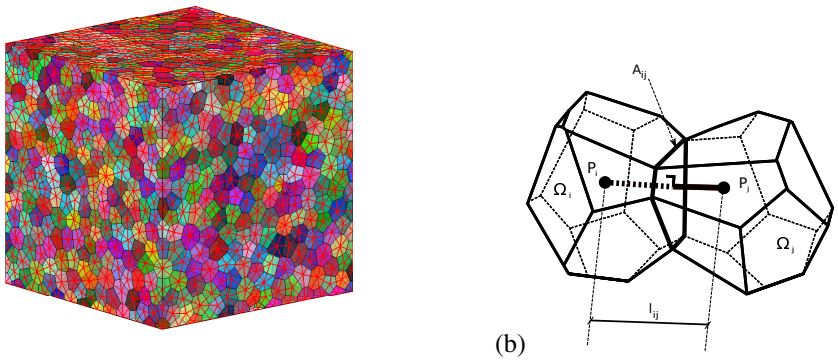

(a) (b)

Figure 1: (a) Structure of a discrete lattice model with Voronoi cells as units; (different colors indicate variability of cohesive links failure parameters for heterogeneous material expressed as RF; (b) two neighboring Voronoi cells and corresponding cohesive links between them (modeled with beam elements capable of representing localized failure modes I, II, and III

It is interesting to note that the fracture stress in tension does not vary much with respect to the variation of the aggregate volume fraction, since only one failure surface at the aggregate-cement interface is needed for the complete fracture of the complete element (see Figure 2). Moreover, the fracture stress does not vary much for tension tests in 3 different directions (see Figure 3), which indicates that concrete can statistically be considered as an isotropic material.

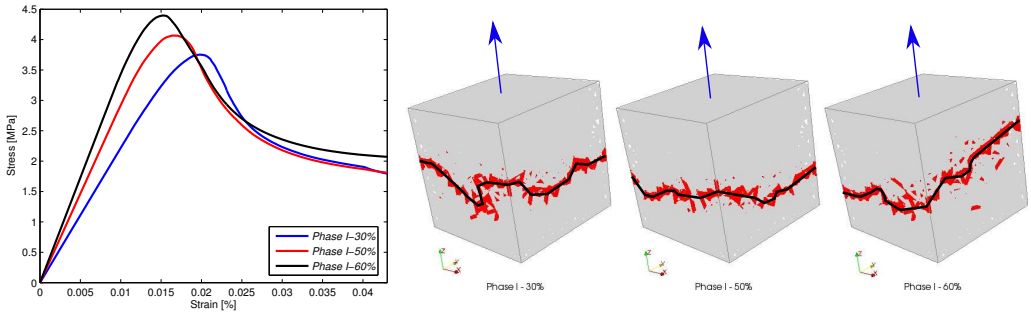

Figure 2: i) Meso-scale model response in uniaxial tension test for different aggregate volume fraction values; ii) Crack contours at the end of uniaxial tension test; cohesive links in failure (beam elements in softening) are marked with red color

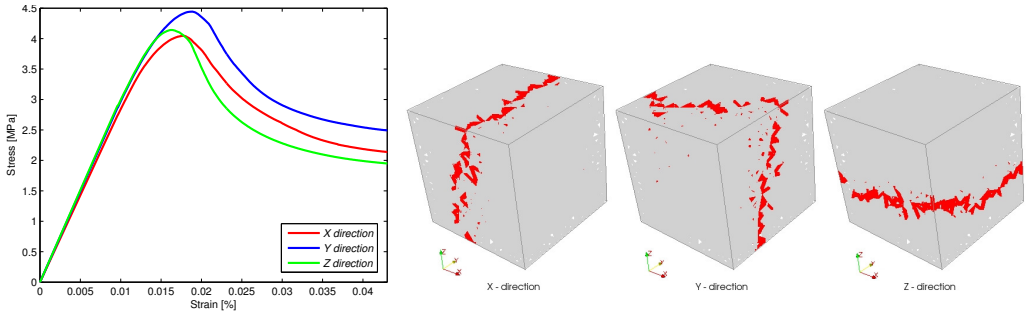

Figure 3: i) Meso-scale model response in a uniaxial tension test (for an aggregate volume fraction of 50%) for three different directions; ii) Crack contours at the end of a uniaxial tension test; cohesive links in failure (beam elements in softening) are marked with red color

Thus, for a given distribution of the fracture stress, it remains to clarify subsequently how to carry on with the computation of a single realization for different parameter values, and how to obtain the uncertainty propagation of

the computed response. The failure modes prediction for a single realization is discussed in detail in Part I of this work ([41]) in terms of the deterministic computation requiring the solution to the following set of equations:

$$\begin{aligned} \boldsymbol{r} &:= \mathop{\mathrm{A}}_{e=1}^{n_{el}} \left(\boldsymbol{f}^{int,(e)} - \boldsymbol{f}^{ext} \right) = 0, \\ \boldsymbol{h}^{(e)} &:= \int_0^{l_e} \overline{\boldsymbol{G}}^T \boldsymbol{\sigma} \, \mathrm{d}x + \boldsymbol{t} = 0, \quad \forall e \in [1, n_{el}^e]; \end{aligned} \tag{2}$$

where $\mathop{\mathrm{A}}_{e=1}^{n_{el}}$ denotes the standard finite element assembly procedure over the total number of elements n_{el}, and $\boldsymbol{f}^{int,(e)} = \int_0^{l_e} \boldsymbol{B}^T \boldsymbol{\sigma} \, \mathrm{d}x$ is the standard internal force vector obtained from the internal stress resultants $\sigma = (N, V, M)$, while the enhanced part $\boldsymbol{h}^{(e)}$ is added for every beam with an active failure mode for which the yield condition in (1) applies. Thus, for any such beam $e \in [1, n_{el}^e]$ with an active micro-crack, we first have to compute the current crack opening $\boldsymbol{\alpha}_{n+1}^{(i,j)}$ in agreement with the current displacement value $\boldsymbol{u}_{n+1}^{(i)}$, and then obtain the corresponding traction value.

$$\begin{aligned} \phi^{trial}(t_{n+1}^{(i)}, \boldsymbol{\alpha}_{n+1}^{(j)}) > 0 \Rightarrow \Delta \boldsymbol{t}_{n+1}^{(j,i)} &= \boldsymbol{K}_{d,n+1}^{(j,i)} \Delta \boldsymbol{u}_{n+1}^{(i)} + \boldsymbol{K}_{\alpha,n+1}^{(j,i)} \Delta \boldsymbol{\alpha}_{n+1}^{(j,i)} \qquad j = 1, 2, \ldots \\ \boldsymbol{\alpha}_{n+1}^{(j+1,i)} &= \boldsymbol{\alpha}_{n+1}^{(j,i)} + \Delta \boldsymbol{\alpha}_{n+1}^{(j,i)} \\ \phi(t_{n+1}^{(j+1,i)}, \boldsymbol{\alpha}_{n+1}^{(i+1)}) &\leq 0 \qquad (i) \leftarrow (j+1), \end{aligned} \tag{3}$$

where $\boldsymbol{K}_{d,n+1}^{(j,i)}$ and $\boldsymbol{K}_{\alpha,n+1}^{(j,i)}$ are the consistent tangent stiffness for the discontinuity (see [41]).

In order to solve the nonlinear problem in (2), we carry out a new iterative sweep providing new iterative values of nodal displacements

$$\begin{aligned} \mathop{\mathrm{A}}_{e=1}^{n_{el}} \widehat{\boldsymbol{K}}_{n+1}^{e} \Delta \boldsymbol{u}_{n+1}^{(i)} &= \mathop{\mathrm{A}}_{e=1}^{n_{el}} \left[\boldsymbol{f}_{n+1}^{ext,e} - \boldsymbol{f}_{n+1}^{int,e,(i)} \right] \\ \Longrightarrow \; \boldsymbol{u}_{n+1}^{(i+1)} &= \boldsymbol{u}_{n+1}^{(i)} + \Delta \boldsymbol{u}_{n+1}^{(i)}. \end{aligned} \tag{4}$$

$$\widehat{\boldsymbol{K}}_{n+1}^{e,(i)} = \boldsymbol{K}_{n+1}^{e,(i)} - (\boldsymbol{F}_{n+1}^{e,(i)})^T (\boldsymbol{H}_{n+1}^{e,(i)} + \boldsymbol{K}_{\alpha,n+1}^{(i)})^{-1} (\boldsymbol{F}_{v,n+1}^{e,(i)} + \boldsymbol{K}_{d,n+1}^{(i)}). \tag{5}$$

$$\begin{aligned} \boldsymbol{K}_{n+1}^{e,(i)} &= \int_0^{l_e} \boldsymbol{B}^T \boldsymbol{C}_{n+1}^{(i)} \boldsymbol{B} \, \mathrm{d}x, \qquad \boldsymbol{F}_{n+1}^{e,(i)} = \int_0^{l_e} \boldsymbol{B}^T \boldsymbol{C}_{n+1}^{(i)} \overline{\boldsymbol{G}} \, \mathrm{d}x, \\ \boldsymbol{F}_{v,n+1}^{e,(i)} &= \int_0^{l_e} \overline{\boldsymbol{G}}^T \boldsymbol{C}_{n+1}^{(i)} \boldsymbol{B} \, \mathrm{d}x, \qquad \boldsymbol{H}_{n+1}^{e,(i)} = \int_0^{l_e} \overline{\boldsymbol{G}}^T \boldsymbol{C}_{n+1}^{(i)} \overline{\boldsymbol{G}} \, \mathrm{d}x, \end{aligned} \tag{6}$$

where $\boldsymbol{C}_{n+1}^{(i)} = \mathrm{diag}(EA, GA, GA, GI_p, EI_{11}, EI_{22})$ is the tangent stiffness for a 3D Timoshenko beam.

2.2. Meso-scale model parameter definition in terms of random fields (RF)

In Part I of this work [41], the material parameters on the meso-scale are considered as constant, the randomness was entirely due to a random geometrical arrangement of the aggregate. Here, we will generalize this development to the case where the fracture parameters of the meso-scale plasticity model can be considered as random fields (RF). In other words, the probability distribution of meso-scale parameters might be changing from point-to-point, which is intuitively clear given that for a two-phase representation at the meso-scale the fracture parameters are affected by uncertainties at the interface between aggregate and cement phase (see Figure 4).

How to obtain the probability distribution of these random fields? The most rigorous approach to provide probability distributions of meso-scale model parameters for fracture would be in terms of a computational procedure of stochastic upscaling from an even smaller scale. Namely, due to concrete meso-scale heterogeneities (aggregate vs. cement), one cannot predict the exact finer-scale (cement) microstructure evolution of initial defects influencing the meso-scale fracture parameters, unless assuming a prior geometry distribution at the meso-scale of the aggregate-cement phase-interfaces. We could further find the solution to such a multi-physics problem of cement hydration which involves probability-based simulations of chemical reactions by using the NIST computational model [6] (where the uncertainty stems from the chain of chemical reactions produced by the mixing of water with cement powder), combined with hydro-mechanics computations of cement-paste-drying next to aggregates [79] (where the uncertainty stems from the random distribution of the aggregate), all resulting with self-desiccation induced micro-cracks and initial defects at the interface. Such computational results could then be used to improve the distribution of

meso-scale fracture parameters as a posterior probability through Bayesian inference. This could be done in off-line probability computations performed as a pre-processing step, where one could use many different microstructure simulations to construct a predictive posterior distribution of meso-scale fracture parameters expressed as random fields. Since it appears to be rather difficult to always control the uncertainties in the multi-physics process of cement hydration and drying, an alternative approach is to use corresponding destructive or non-destructive measurements (e.g. [49]) to directly observe the self-diseccation cracks, and quantify the corresponding phase-interface fracture parameters as random fields. The upscaling process just alluded to is another example of a stochastic upscaling procedure, in principle completely analogous to the one from meso- to macro-scale described here. In this work, we assume that the meso-scale parameters are in either way defined as random fields, and their probabilistic description is assumed as given.

Subsequently, it remains to deal with the given uncertainties on the meso-scale and how they influence the macro-scale in order to provide the corresponding variability in the response of a structure — here a macro-scale solid element with ED-FEM discrete approximation. The uncertainty propagation starting from such meso-scale parameter probability distributions is handled through scale-coarsening resulting in a mechanics-based reduced model at the macro-scale that can achieve computational efficiency, as described later in Sections 3 and 4. Presently, the parameters at the macro-scale are considered as spatially constant, i.e. they are modelled as random variables.

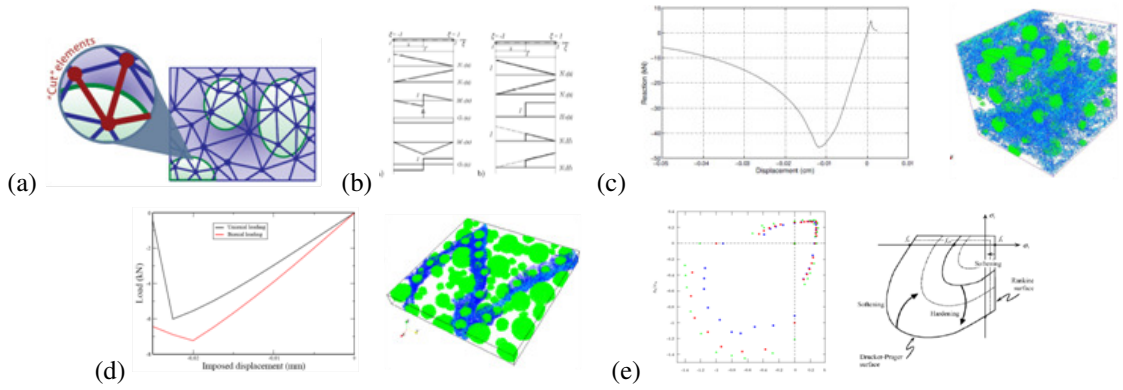

Figure 4: (a) two-phase concrete model meso-scale representation ([5], [41]): aggregate (white) vs. cement paste (violet); (b) cohesive links at meso-scale with structured mesh (keeping the same mesh for different realizations in probability computations) requiring both strain and displacement discontinuity implemented within ED-FEM with the same number of parameters as X-FEM, but a more clear role for each parameter resulting in higher computational efficiency ([33]); (c) uniaxial compression force-displacement and failure mode with cohesive links failure; (d) biaxial compression (confirming compressive strength increase from uniaxial case) and failure mode; (e) replacing failure criterion for different failure modes under biaxial stress (colors: showing increased resistance in compression for higher aggregate volume fraction, dots: providing computed value of fracture energy for corresponding failure mode) and comparison against classical Rankin-Drucker-Prager multi-surface plasticity criteria ([34]).

The first step in building such a coupled meso-scale-probability model concerns representing the source of uncertainty, here the fracture stress parameters at the phase-interface, described as random fields $p(x,\omega)$. At a fixed point of the macro-element domain $x \in \mathcal{V} \subseteq \mathbb{R}^d$, each parameter p is a random variable (RV) on a suitable probability space $(\Omega, \mathfrak{U}, \mathbb{P})$ (see e.g. [37]), where Ω is the set of all elementary random events, $\mathfrak{U}$ is the σ-algebra of measurable subsets $S \subseteq \Omega$ to which a probability $\mathbb{P}(S)$ can be assigned. For $p(x,\omega) : \mathcal{V} \times \Omega \to \mathbb{R}$ as a random field (RF), one may identify Ω with the set of all possible values of the parameters, i.e. all realizations. Alternatively, $p(x,\omega)$ can be seen as a collection of real-valued random variables $p_{\bar{x}}(\omega)$ indexed by $\bar{x} \in \mathcal{V}$. The expectation of a random variable via the probability measure is given by $\mu_p(x) = \mathbb{E}(p(x,\cdot)) := \int_\Omega p(x,\omega)\ \mathbb{P}(\mathrm{d}\omega)$, this is the most basic characterization of such a random field (RF) through its *mean-value* function $\mu_p(x)$. The covariance function $C_p(x,x') = \mathbb{E}\left((p(x,\cdot)-\mu_p(x))(p(x',\cdot)-\mu_p(x'))\right)$ is a characterisation of the spatial variation of the field. In case the field is Gaussian, i.e. the RVs $p(x,\cdot)$ are Gaussian at each $x \in \mathcal{V}$, knowledge of the mean and covariance is sufficient to determine the RF completely. But we will here consider a more general case with the parameters $p(x,\omega)$ as non-Gaussian fields (e.g. log-normal), which may be expressed directly as functions of Gaussian fields (see e.g. [25, 55]), that is $p(x,\omega) = \Upsilon(x,\gamma(x,\omega))$, where Υ is a point-wise transformation, and $\gamma(x,\omega)$ is a Gaussian random field.

In a computational setting this field must be discretized. Two main approaches for this have emerged (see e.g. [55]), which may be combined. One is the polynomial chaos expansion (PCE) ([37]), which goes back to N. Wiener and states in its basic form that any RV $q(\omega)$ of finite variance — $q \in L_2(\Omega, \mathfrak{U})$ — may be expanded in polynomials of *standard* (mean zero and unit variance) *independent* Gaussian RVs $\boldsymbol{\eta}(\omega) = (\eta_1(\omega), \dots, \eta_j(\omega), \dots)$: $q(\omega) = \sum_{\boldsymbol{\alpha}\in\mathcal{N}} q^{\boldsymbol{\alpha}} H_{\boldsymbol{\alpha}}(\boldsymbol{\eta}(\omega))$. Here $\boldsymbol{\alpha} = (\alpha_1, \dots, \alpha_j, \dots) \in \mathcal{N} := \mathbb{N}_0^{(\mathbb{N})}$ is a multi-index of usually infinite length, where only finitely many $\alpha_j \neq 0$, and the $H_{\boldsymbol{\alpha}}(\boldsymbol{\eta}(\omega))$ are multivariate Hermite polynomials $H_{\boldsymbol{\alpha}}(\boldsymbol{\eta}(\omega)) = \prod_{j=1}^{\infty} h_{\alpha_j}(\eta_j(\omega))$, namely products of univariate Hermite polynomials $h_{\alpha_j}(\eta_j(\omega))$. As the univariate Hermite polynomials h_{α_j} are orthogonal w.r.t. the one-dimensional Gaussian measure $\Gamma(\mathrm{d}t) = (2\pi)^{-1/2}\exp(-t^2/2)\mathrm{d}t$, i.e. $\int_{\mathbb{R}} h_{\alpha_j}(t)h_{\alpha_k}(t)\,\Gamma(\mathrm{d}t) = \delta_{jk}\alpha_j!$, one easily [37] concludes that the multivariate Hermite polynomial are orthogonal w.r.t. to the Gaussian product measure: $\mathbb{E}(H_{\boldsymbol{\alpha}}(\boldsymbol{\eta}(\cdot))H_{\boldsymbol{\beta}}(\boldsymbol{\eta}(\cdot))) = \delta_{\boldsymbol{\alpha}\boldsymbol{\beta}}\boldsymbol{\alpha}!$, where for a multi-index the factorial is defined as $\boldsymbol{\alpha}! := \prod_{j=0}^{\infty}\alpha_j!$. In computations an approximation is used, where the range of the multi-indices is constricted to a finite subset $\mathcal{J} \subset \mathcal{N}$.

In case of a random field $p(x, \omega)$, one may use this expansion at each $x \in \mathcal{V}$, where now the coefficients $p^{\boldsymbol{\alpha}}(x)$ become functions of the spatial point $x \in \mathcal{V}$ to give the PCE expansion of RFs:

$$p(x,\omega) = \sum_{\boldsymbol{\alpha}\in\mathcal{N}} p^{\boldsymbol{\alpha}}(x)H_{\boldsymbol{\alpha}}(\boldsymbol{\eta}(\omega)), \qquad \text{with } p^{\boldsymbol{\alpha}}(x) = \frac{1}{\sqrt{\boldsymbol{\alpha}!}}\mathbb{E}(p(x,\cdot)H_{\boldsymbol{\alpha}}(\boldsymbol{\eta}(\cdot))) \text{ and } p^{\mathbf{0}}(x) = \mu_p(x). \tag{7}$$

The computational cost is usually quite high with this approach, as the PCE representation is completely general and no rule is employed to pick the basic RVs η_k, and an excessive number of RVs $(\eta_1(\omega), \dots, \eta_k(\omega), \dots)$ and number of terms in (7) may be needed to give an accurate enough approximation when the above PCE representation is truncated to some finite subset $\boldsymbol{\alpha} \in \mathcal{J} \subset \mathcal{N}$.

The choice of basic RVs is facilitated by the second approach to be discussed, the Karhunen-Loève expansion (KLE), which is a very useful tool for a more concise spectral representation of the random field (e.g. see [55, 54]). In this case, we can write the KLE spectral representation of the meso-model parameters as:

$$p(x,\omega) = \mu_p(x) + \sum_{i=1}^{\infty}\sqrt{\lambda_i}\theta_i(\omega)\varphi_i(x), \tag{8}$$

where $\theta_i(\omega)$ is a set of uncorrelated RVs of zero mean and unit variance, the λ_i are positive eigenvalues ordered in a descending order, and $\varphi_i(x)$ are the orthonormal eigenfunctions obtained by solving a self-adjoint Fredholm integral equation with the covariance function as the integral kernel (see e.g. [55] for more details).

The KLE is very closely connected to the singular value decomposition, and may similarly serve as a device for dimension reduction. The variance of the $i-th$ term in (8) is λ_i, and hence by truncating the sum in (8) at some N_θ, the error in variance of the approximation is simply given by $\sum_{i=N_\theta+1}^{\infty}\lambda_i$. The RVs $\theta_i(\omega)$ are furthermore defined by the RF $p(x, \omega)$ through simple projection (due to the orthonormality):

$$\theta_i(\omega) = \frac{1}{\sqrt{\lambda_i}}\int_{\mathcal{V}}\Big(p(x,\omega) - \mu_p(x)\Big)\varphi_i(x)\,\mathrm{d}x. \tag{9}$$

Obviously, if the field is Gaussian, then the θ_i are jointly Gaussian, and hence not only uncorrelated but actually *independent*, and in that case the KLE (8) is actually a PCE (7) as only linear polynomials are needed.

For more complex physical domains computing the eigenfunctions analytically is usually not feasible, and one has to discretize the covariance spatially according to chosen grid points (in the finite element mesh). The resulting covariance is a symmetric and positive definite matrix $\boldsymbol{C}_p$, and the Fredholm equation results in a symmetric matrix defining the corresponding eigenvalue problem, where the eigenfunctions $\varphi_i(x)$ are replaced by eigenvectors $\boldsymbol{\varphi}_i$. An eigenvalue problem of this kind can be solved by a Krylov subspace method (see e.g. [70, 29]).

With the descending sequence of eigenvalues truncated after N_θ terms, this leads to the discrete approximation

$$\boldsymbol{p}(\omega) = \boldsymbol{\mu}_p + \sigma_c\sum_{i=1}^{N_\theta}\sqrt{\lambda_i}\theta_i(\omega)\boldsymbol{\varphi}_i, \tag{10}$$

which has the same mean as the original field and will also have the correct total variance—only distributed on the modes $\boldsymbol{\varphi}_j$ with $j \leq N_\theta$ with the correction factor $\sigma_c = \sqrt{\sigma_t^2/(\sigma_t^2 - \sigma_r^2)}$; here $\sigma_t^2 = \sum_{i=1}^{\infty}\lambda_i$ and $\sigma_t^2 = \sum_{i=1}^{N_\theta}\lambda_i$. Thus,

such a spatial semi-discretization is optimal in the sense that the mean square error resulting from a truncation after the N_θ-th term is minimized.

It remains to discretize the RVs $\theta_i(\omega)$ in the non-Gaussian case. Here one may use the PCE of each $\theta_i(\omega) = \sum_{\boldsymbol{\alpha}\in\mathcal{N},\boldsymbol{\alpha}\neq 0} \theta_i^{\boldsymbol{\alpha}} H_{\boldsymbol{\alpha}}(\boldsymbol{\xi}(\omega))$; and inserting this into the KLE (8) gives

$$p(x,\omega) = \mu_p(x) + \sum_{i=1}^{\infty} \sqrt{\lambda_i}\left(\sum_{\boldsymbol{\alpha}\in\mathcal{N},\boldsymbol{\alpha}\neq 0} \theta_i^{\boldsymbol{\alpha}} H_{\boldsymbol{\alpha}}(\boldsymbol{\xi}(\omega))\right)\varphi_i(x) = \mu_p(x) + \sum_{\boldsymbol{\alpha}\in\mathcal{N},\boldsymbol{\alpha}\neq 0}\left(\sum_{i=1}^{\infty} \theta_i^{\boldsymbol{\alpha}} \sqrt{\lambda_i}\varphi_i(x)\right) H_{\boldsymbol{\alpha}}(\boldsymbol{\xi}(\omega)), \tag{11}$$

As $H_0 \equiv 1$, comparison with (7) shows that one has $p^0(x) = \mu_p(x)$, and generally $p^{\boldsymbol{\alpha}}(x) = \sum_{i=1}^{\infty} \theta_i^{\boldsymbol{\alpha}} \sqrt{\lambda_i}\varphi_i(x)$. The advantage of this combination of KLE and PCE is that upon truncation as in (10), the discretization may be completed to

$$\boldsymbol{p}(\boldsymbol{\xi}(\omega)) = \boldsymbol{\mu}_p + \sigma_c \sum_{i=1}^{N_\theta} \sqrt{\lambda_i}\left(\sum_{\boldsymbol{\alpha}\in\mathcal{J},\boldsymbol{\alpha}\neq 0} \theta_i^{\boldsymbol{\alpha}} H_{\boldsymbol{\alpha}}(\boldsymbol{\xi}(\omega))\right)\boldsymbol{\varphi}_i = \sum_{\boldsymbol{\alpha}\in\mathcal{J}} \boldsymbol{p}^{\boldsymbol{\alpha}} H_{\boldsymbol{\alpha}}(\boldsymbol{\xi}(\omega)), \tag{12}$$

with $\boldsymbol{p}^0 = \boldsymbol{\mu}_p$, and otherwise $\boldsymbol{p}^{\boldsymbol{\alpha}} = \sigma_c \sum_{i=1}^{N_\theta} \theta_i^{\boldsymbol{\alpha}} \sqrt{\lambda_i}\boldsymbol{\varphi}_i$, and where the finite subset $\mathcal{J} \subset \mathcal{N}$ is such that it involves only non-zero indices α_k with $k \leq N_\theta$ and hence only a finite number of Gaussian RVs $\xi_k(\omega), (k = 1, \ldots, N_\theta)$, which in terms of variance carry the main probabilistic contribution.

In summary, the vector of model parameters $\boldsymbol{p}(\boldsymbol{\xi}(\omega))$ represents now the discretized spatial field $p(x,\omega)$ which is described by a limited number N_θ of independent Gaussian random variables $\boldsymbol{\xi}(\omega) = (\xi_1(\omega), \ldots, \xi_{N_\theta}(\omega))^T$. Hence, any response of the discretized system has also a random nature and can be expressed in terms of the same random variables $\boldsymbol{\xi}(\omega)$. In particular, of special interest for the macro-scale reduced model computation via Bayesian inference are the RVs of strain energy or dissipation in the volume $\mathcal{V}$., which can be computed as explained later in the next Subsection 2.3.

2.3. The discrete stochastic problem

Taking for example the displacement vector of the system, $\tilde{\boldsymbol{u}}(\omega) = (u_1(\omega), \ldots, u_i(\omega), \ldots, u_M(\omega))^T \in \mathbb{R}^M$, this can be written as

$$\tilde{\boldsymbol{u}}(\boldsymbol{\xi}(\omega)) = \sum_{\boldsymbol{\alpha}\in\mathcal{J}} \boldsymbol{d}_{\boldsymbol{\alpha}}\, H_{\boldsymbol{\alpha}}(\boldsymbol{\xi}(\omega)) = \boldsymbol{d}\cdot\boldsymbol{H}(\boldsymbol{\xi}), \quad \text{with} \quad \boldsymbol{d} = \sum_{\boldsymbol{\alpha}\in\mathcal{J}} \boldsymbol{d}_{\boldsymbol{\alpha}} \otimes \boldsymbol{e}_{\boldsymbol{\alpha}}, \tag{13}$$

where $\boldsymbol{d}_{\boldsymbol{\alpha}} = (\ldots d_{\alpha,i} \ldots)^T \in \mathbb{R}^M$ is a vector of PCE coefficients, $\boldsymbol{e}_{\boldsymbol{\alpha}} \in \mathbb{R}^{N_J}$ are the canonical unit vectors with $N_J = |\mathcal{J}|$ the size or cardinality of the set $\mathcal{J} \subset \mathcal{N}$, and $\boldsymbol{H}(\boldsymbol{\xi}) = \sum_{\boldsymbol{\alpha}\in\mathcal{J}} H_{\boldsymbol{\alpha}}(\boldsymbol{\xi})\boldsymbol{e}_{\boldsymbol{\alpha}}$ is a N_J-dimensional vector of Hermite polynomials.

One interpretation of this choice for the construction of a surrogate model is in terms of discrete approximation, where the probability set Ω is transported to $\boldsymbol{\Xi} := \boldsymbol{\xi}(\Omega) = \mathbb{R}^{N_\theta}$ with a Gaussian product measure $\boldsymbol{\Gamma}(\mathrm{d}\boldsymbol{t}) = \bigotimes_{k=1}^{N_\theta} \Gamma(\mathrm{d}t_k)$, $(\boldsymbol{t} = (t_1, t_2, \ldots, t_{N_\theta}) \in \mathbb{R}^{N_\theta})$, and is treated as an approximation domain over which we choose a p-method mesh refinement (e.g.[102]). In other words, the whole N_θ-dimensional domain $\boldsymbol{\Xi}$ is discretized with multi-variate Hermite polynomials $H_{\boldsymbol{\alpha}}$ by a finite number of terms $\boldsymbol{\alpha} \in \mathcal{J}$. Thus, the complete discrete approximation of the displacement field combining the finite element (h-method) and the PCE (p-method) can be written as

$$\boldsymbol{u}^h(x,\boldsymbol{\xi}) = \boldsymbol{N}(x)\cdot\tilde{\boldsymbol{u}}(\xi) = \boldsymbol{N}(x)\cdot\boldsymbol{d}\cdot\boldsymbol{H}(\boldsymbol{\xi}), \tag{14}$$

where $\boldsymbol{N}(x) = (N_1(x), \ldots, N_M(x))$ are standard FE shape functions and the unknowns are the entries of the matrix $\boldsymbol{d}$.

With a chosen appropriate discretization over the spatial and probability domains, the response is further obtained by the Stochastic Galerkin method ([55]), resulting in a system of algebraic equations for the unknowns $\boldsymbol{d}$. Considering the elastic case for simplicity, we can first write the end-product of the spatial discretization for each particular realization $\hat{\omega}$ of the parameters $\boldsymbol{p}(\hat{\boldsymbol{\xi}}) = \boldsymbol{p}(\boldsymbol{\xi}(\hat{\omega}))$,

$$\boldsymbol{K}\left(\boldsymbol{p}(\hat{\boldsymbol{\xi}})\right)\tilde{\boldsymbol{u}}(\hat{\boldsymbol{\xi}}) = \boldsymbol{f}(\hat{\boldsymbol{\xi}}). \tag{15}$$

By approximating the nodal response by its PCE truncated representation $\tilde{\boldsymbol{u}}$ given in (14), and applying the Galerkin weighting residual procedure over the probability set $\boldsymbol{\Xi}$, one arrives at:

$$\begin{aligned} &\mathbb{E}\left(\boldsymbol{K}\left(p(\cdot)\right)\otimes\left[\boldsymbol{H}(\cdot)\otimes\boldsymbol{H}(\cdot)\right]\right):\boldsymbol{d}=\mathbb{E}\left(\boldsymbol{f}(\cdot)\otimes\boldsymbol{H}(\cdot)\right)=:\boldsymbol{g}\,;\\ &\boldsymbol{g}:=\mathbb{E}\left(\boldsymbol{f}(\cdot)\otimes\boldsymbol{H}(\cdot)\right)=\int_{\Omega}\boldsymbol{f}(\boldsymbol{\xi}(\boldsymbol{\omega}))\otimes\boldsymbol{H}(\boldsymbol{\xi}(\boldsymbol{\omega}))\,\mathbb{P}(\mathrm{d}\omega)=\int_{\boldsymbol{\Xi}}\boldsymbol{f}(\boldsymbol{\xi})\otimes\boldsymbol{H}(\boldsymbol{\xi})\,\boldsymbol{\Gamma}(\mathrm{d}\boldsymbol{\xi}), \end{aligned} \tag{16}$$

where the colon ':' denotes as usual the double contraction. One may note that the expansion and approximation of the parameter RF in (12) results in an analogous expansion and approximation of the random stiffness matrix in (15):

$$\begin{aligned} \boldsymbol{K}(\boldsymbol{\xi}):=\boldsymbol{K}\left(\boldsymbol{p}(\boldsymbol{\xi}(\omega))\right)\approx\hat{\boldsymbol{K}}(\hat{\boldsymbol{p}}(\boldsymbol{\xi}(\omega)))=\bar{\boldsymbol{K}}+\sum_{i=1}^{N_\theta}\sqrt{\lambda_i^{(K)}}\,\vartheta_i^{(K)}(\boldsymbol{\xi}(\omega))\,\boldsymbol{K}_i\\ \approx\sum_{\boldsymbol{\alpha}\in\mathcal{J}}\boldsymbol{K}^{\boldsymbol{\alpha}}H_{\boldsymbol{\alpha}}(\boldsymbol{\xi}(\omega)),\ \text{with}\ \boldsymbol{K}^{\boldsymbol{\alpha}}:=\frac{1}{\sqrt{\boldsymbol{\alpha}!}}\,\mathbb{E}(\boldsymbol{K}(\cdot)H_{\boldsymbol{\alpha}}(\cdot)) \end{aligned} \tag{17}$$

When (17) is substituted in (16) above, it results in the final product of the Stochastic Galerkin method, a system of $M\times N_J$ algebraic equations for the unknowns $\boldsymbol{d}$:

$$\begin{aligned} &\left[\textstyle\sum_{\boldsymbol{\alpha}\in\mathcal{J}}\boldsymbol{K}^{\boldsymbol{\alpha}}\otimes\boldsymbol{\Delta}_{\boldsymbol{\alpha}}\right]:\boldsymbol{d}=\boldsymbol{g};\\ &\boldsymbol{\Delta}_{\boldsymbol{\alpha}}:=\mathbb{E}(H_{\boldsymbol{\alpha}}(\cdot)[\boldsymbol{H}(\cdot)\otimes\boldsymbol{H}(\cdot)])=\int_{\boldsymbol{\Xi}}H_{\boldsymbol{\alpha}}(\boldsymbol{\xi})[\boldsymbol{H}(\boldsymbol{\xi})\otimes\boldsymbol{H}(\boldsymbol{\xi})\,\boldsymbol{\Gamma}(\mathrm{d}\boldsymbol{\xi}). \end{aligned} \tag{18}$$

The solution of this set of algebraic equations provides the PCE coefficients $\boldsymbol{d}$ corresponding to the displacement field in (13), and subsequently any other dependent variables.

It is clear that the number of terms of the PCE expansion may increase quite fast, if only the maximum degree of polynomials N_p and/or the dimensions N_θ of $\xi(\omega)\in\mathbb{R}^{N_\theta}$ are used as controlling parameters; after all this is a *high-dimensional* problem, and one feels the *curse of dimensions*. A finer control of the number of variables is usually called for. The number of random variables is already reduced by using uncorrelated variables $\theta(\omega)$ from the KLE. These variables are related to eigenvalues of different magnitude expressing the importance of particular eigenmodes. Another possibility to decrease N_J is to neglect terms in the PCE representation, where less important variables ξ_i are in higher orders ([55]). The maximal degree of polynomials N_p can be also reduced e.g. by a sub-division of the modeled domain V as presented e.g. by [54]. Other computational savings can be achieved by formulating (10) in tensorial instead of matrix notation ([55]), and solved using low-rank tensor methods [60, 97, 17]. These methods effectively create a 'sparse' surrogate or proxy model — in contrast to the 'full' proxy or surrogate computed in (18) — containing the PCE representations of the forward model outputs [13]. This model approximation needs less data and is faster to evaluate than (18), and both may be evaluated orders of magnitude quicker than the 'direct' evaluation containing the full forward problem. Due to the abstract Galerkin structure, all of this can be combined in a fully spatially-stochastically adaptive approach [14] with corresponding error estimators, balancing the spatial and stochastic error optimally.

Given the solution $\boldsymbol{d}$ to the stochastic Galerkin procedure, one may now easily define e.g. the expected value of strain energy of this meso-scale model as:

$$\hat{y}:=\mathbb{E}[Y_m(\omega)]=\frac{1}{2}\,\boldsymbol{d}:\left(\sum_{\boldsymbol{\alpha}\in\mathcal{J}}\boldsymbol{K}^{\boldsymbol{\alpha}}\otimes\boldsymbol{\Delta}_{\boldsymbol{\alpha}}\right):\boldsymbol{d}=\frac{1}{2}\,\boldsymbol{d}:\boldsymbol{g}. \tag{19}$$

Somewhat more elaborate computations are needed to obtain the expected meso-scale model plastic dissipation (see [65] for details). Both of these results are needed to provide for the 'measurements' in the Bayesian inference used to identify the probability distribution of the macro-scale reduced model parameters (see Section 4).

3. Plasticity at multiple scales: macro-scale reduced ED-FEM model for localized failure analysis of concrete

We can see in Figure 4 (see also Part I in [41]) that none of the classical plasticity criteria for concrete, (e.g. [28]), can fully match the result accuracy obtained by the meso-scale model. Yet there is the need for a concrete macro-scale

model that can make the analysis of full-scale structures computationally feasible. Hence, our first goal is to provide computational plasticity multi-surface criteria for concrete that are more comprehensive than any classical criteria in representing the full set of failure modes, localization, and appearance of cracks. For concrete cracks representation, one can choose between two dominantly used methods: extended finite element or X-FEM [63], which uses a global displacement discontinuity representing a single (connected) crack, and embedded discontinuity finite element method or ED-FEM [32], which uses an element-wise displacement discontinuities representing multiple, disconected cracks (one in each element). The latter is chosen here, not only for being more appropriate to describe the real crack patterns in concrete, with multiple rather than a single crack, but also for its sound theoretical formulation that fits within the framework of nonequilibrium statistical thermodynamics [18], by assuming that the time scale of evolution for internal variables (here micro-cracks represented by FPZ hardening plasticity and macro-cracks represented by ED-FEM softening plasticity) remains much shorter than the time scale of stress evolution. The latter is valid hypothesis when we apply quasi-static loading where the stress increase/decrease has to match the external loading through equilibrium equations. Within chosen thermodynamics framework for ED-FEM, the embedded-discontinuity-crack representation (or 'thermodynamic flux') does not split the concrete domain (as with X-FEM model), but considers 'continuous' representation of a gradual decrease of bearing stress (or 'thermodynamic force') until complete failure. The latter is defined through fracture energy G_f, which is by far the most reliable material parameter for fracture representing the energy needed to completely 'break' the material by reducing the bearing stress capacity to zero for any particular failure mode (e.g. $G_{f,t}$ in tension or $G_{f,c}$ in compression). This choice of ED-FEM allows to compute both FPZ and softening plastic dissipations independently in each particular macro-scale element for later comparison against the corresponding values computed by the meso-scale model (e.g. [65]). Our second goal is to enhance the predictive capabilities of such a model in terms of stochastic plasticity, with its parameters replaced by random variables. The probability distribution of these random variables is obtained by an efficient procedure of Bayesian inference, which is detailed in Section 4.

To simplify our discussion, first consider the deterministic case in the Euclidean setting and corresponding tensor notation [34], with the displacement vector $\boldsymbol{u}$ as a function of both space position $\boldsymbol{x}$ and pseudo-time t:

$$\boldsymbol{u}(\boldsymbol{x}, t) = u_i(\boldsymbol{x}, t)\, \boldsymbol{e}_i; \qquad \boldsymbol{x} = x_i\, \boldsymbol{e}_i$$

Linearized kinematics is used to define the total strain tensor, $\boldsymbol{\epsilon}$, as the symmetric part of the displacement gradient

$$\boldsymbol{\epsilon} = \nabla^s \boldsymbol{u}; \qquad \epsilon_{ij}\, \boldsymbol{e}_i \otimes \boldsymbol{e}_j = \frac{1}{2}\left(\frac{\partial u_i}{\partial x_j} + \frac{\partial u_j}{\partial x_i}\right) \boldsymbol{e}_i \otimes \boldsymbol{e}_j$$

The same hypothesis on small displacement gradients allows us to express the equilibrium equations directly in the initial configuration in terms of Cauchy or true stress, $\boldsymbol{\sigma} = \sigma_{ij}\, \boldsymbol{e}_i \otimes \boldsymbol{e}_j$, the dual variable to strain.

In the presence of plastic deformation, the stress is computed not from the total, but only from the elastic deformation. Namely, by assuming the independence of the elastic response on plastic flow, the total deformation can be split additively into an elastic $\boldsymbol{\epsilon}^e$ and a plastic part $\boldsymbol{\epsilon}^p$,

$$\boldsymbol{\epsilon} = \boldsymbol{\epsilon}^e + \boldsymbol{\epsilon}^p.$$

By further assuming that the elastic response remains linear, reducing to Hooke's law in the absence of plastic deformation, we can construct the free energy potential as a quadratic form in terms of the deformation tensor

$$\psi(\boldsymbol{\epsilon}, \boldsymbol{\epsilon}^p, \zeta) := \tfrac{1}{2}(\boldsymbol{\epsilon} - \boldsymbol{\epsilon}^p) : \boldsymbol{C} : (\boldsymbol{\epsilon} - \boldsymbol{\epsilon}^p)) + \Xi(\zeta), \tag{20}$$

where $\boldsymbol{C}$ is elasticity tensor and $\Xi(\zeta)$ is the hardening potential. With concrete as a statistically isotropic material we can fully characterize the elasticity tensor from two parameters only, such as the bulk modulus K and the shear modulus G. When crossing into the inelastic regime, where stress states trigger creation of the fracture process zone (FPZ) or localized failure, one has to define a corresponding macro-scale plasticity yield criterion. The latter has to be defined as multi-surface plasticity in order to fully capture the full set of 3D failure modes for concrete (e.g. [42]). In particular, we take the Drucker-Prager model for representing shear failure:

$$\phi_y(\boldsymbol{\sigma}, q) := \|\mathrm{dev}\, \boldsymbol{\sigma}\| + \frac{1}{3}\tan(\varphi)\, \mathrm{tr}\, \boldsymbol{\sigma} - \sqrt{\frac{2}{3}}\,(\sigma_y - q) = 0; \quad \mathrm{dev}\, \boldsymbol{\sigma} = \boldsymbol{\sigma} - \frac{1}{3}(\mathrm{tr}\, \boldsymbol{\sigma})\mathbf{1}, \tag{21}$$

where $\|\text{dev}\,\boldsymbol{\sigma}\| := \sqrt{\text{dev}\,\boldsymbol{\sigma} : \text{dev}\,\boldsymbol{\sigma}}$ is the norm of the deviatoric part of the stress tensor dev $\boldsymbol{\sigma}$, $\tan(\varphi)$ is a material parameter that characterizes the internal friction, σ_y is the uni-axial yield stress identified from a tension test, and q is a thermodynamic force dual to the hardening variable ζ in (20).

By specifying the three fundamental results in (3), (20), and (21), we can completely define the stress tensor computation as well as the evolution of internal variables for the activation of the shear failure mode. In the hardening regime, we simply use the local form of the second principle of thermodynamics, maximizing the plastic dissipation rate (e.g. [34]):

$$0 \leq D^p := (\boldsymbol{\sigma} - \frac{\partial \psi}{\partial \boldsymbol{\epsilon}}) : \dot{\boldsymbol{\epsilon}} - \frac{\partial \psi}{\partial \boldsymbol{\epsilon}^p} : \dot{\boldsymbol{\epsilon}}^p - \frac{\partial \psi}{\partial \zeta} \cdot \dot{\zeta}$$

In the elastic case with $\phi < 0$, the plastic dissipation remains equal to zero ($D^p = 0$), which allows to define the constitutive equations:

$$\boldsymbol{\sigma} := -\frac{\partial \psi}{\partial \boldsymbol{\epsilon}^p} = \boldsymbol{C} : (\boldsymbol{\epsilon} - \boldsymbol{\epsilon}^p)\,; \quad q := -\frac{\partial \psi}{\partial \zeta} = -K\zeta$$

By assuming that the constitutive equations above remain valid in the plastic case with $\phi = 0$, we can obtain the final expression for the plastic dissipation:

$$\phi = 0 \Rightarrow 0 < D^p := \boldsymbol{\sigma} : \dot{\boldsymbol{\epsilon}}^p + q \cdot \dot{\zeta}$$

The principle of maximum plastic dissipation may be invoked, stating that among all the admissible stress states (for which $\phi_y(\boldsymbol{\sigma}, q) = 0$) , one ought to choose the one which maximizes the plastic dissipation. This problem of computing the maximum under the plastic admissibility constraint can be transformed into a corresponding unconstrained minimization problem (see [34])

$$L^p(\boldsymbol{\sigma}, q, \dot{\gamma}) = \max_{\dot{\gamma}^* \geq 0} \min_{\boldsymbol{\sigma}^*, q^*} [\, L^p(\boldsymbol{\sigma}^*, q^*, \dot{\gamma}^*) \,]\,; \quad L^p(\boldsymbol{\sigma}, q, \dot{\gamma}) := -D^p(\boldsymbol{\sigma}, q) + \dot{\gamma}\phi_y(\boldsymbol{\sigma}, q).$$

The associated Kuhn-Tucker optimality conditions lead to evolution equations for internal variables:

$$\begin{aligned} 0 &= \frac{\partial L^p(\boldsymbol{\sigma}, q, \dot{\gamma})}{\partial \boldsymbol{\sigma}} = -\dot{\boldsymbol{\epsilon}}^p + \dot{\gamma}\frac{\partial \phi_y(\boldsymbol{\sigma}, q)}{\partial \boldsymbol{\sigma}}; \\ 0 &= \frac{\partial L^p(\boldsymbol{\sigma}, q, \dot{\gamma})}{\partial q} = -\dot{\zeta} + \dot{\gamma}\frac{\partial \phi_y(\boldsymbol{\sigma}, q)}{\partial q}; \\ \dot{\gamma} &\geq 0; \quad \phi_y(\boldsymbol{\sigma}, q) \leq 0; \quad \dot{\gamma}\phi_y(\boldsymbol{\sigma}, q) = 0 \end{aligned} \tag{22}$$

We can further generalize such a plasticity criterion for a concrete-like material to the case where the dilatancy of plastic flow develops, which requires a non-associative plasticity framework, where the plastic potential function is different than the yield function (e.g. [42]):

$$\phi_p(\boldsymbol{\sigma}, q) := \|\text{dev}\,\boldsymbol{\sigma}\| + \tfrac{1}{3}\tan(\psi)\,\text{tr}\,\boldsymbol{\sigma}, \tag{23}$$

where $\tan(\psi)$ is a material parameter describing the angle of dilatancy. It is important to note that such a choice can further lead to material instability phenomena even in hardening (e.g. see [34]). We will rather deal with the more typical case of material instability which occurs as the result of macro-scale cracks in concrete for either tension or compression failure leading to softening, where stress decreases for increasing strain. One can accommodate the softening phenomena within associative plasticity framework, by making two appropriate modifications. First one needs the strong discontinuity approach to represent the steep strain gradients in softening phenomena both in tension and compression, and second one needs a non-local form of the second principle of thermodynamics that is suitable for including plastic dissipation resulting from cracks in concrete. This will further be discussed for the chosen multi-surface plasticity criterion of St. Venant that can handle the localized failure both in tension and in compression in a unified framework ([34]). The latter is provided by defining a corresponding three surface criterion in strain space,

which is further recast in standard format in stress space leading to:

$$\phi_1(\boldsymbol{\sigma}) = \frac{3K+G}{9KG}\sigma_1 - \frac{3K-2G}{18KG}(\sigma_2+\sigma_3) - (\sigma_u - q) \leq 0$$
$$\phi_2(\boldsymbol{\sigma}) = \frac{3K+G}{9KG}\sigma_2 - \frac{3K-2G}{18KG}(\sigma_1+\sigma_3) - (\sigma_u - q) \leq 0$$
$$\phi_3(\boldsymbol{\sigma}) = \frac{3K+G}{9KG}\sigma_3 - \frac{3K-2G}{18KG}(\sigma_1+\sigma_2) - (\sigma_u - q) \leq 0,$$

where we have chosen the reference value of the elasticity limit obtained from hydrostatic tension test. By combining such a St. Venant multi-surface criterion with the one of Drucker-Prager, the macro-scale model can represent three different deformation stages: linear elastic, hardening and localized softening, which is the typical behavior of massive structures for failure in compression with a FPZ with micro-cracks and softening behavior with macro-cracks. Figure 5 shows a graphic illustration of the proposed macro-scale multi-surface plasticity criterion in the space of the principal axes of the stress tensor and cut in the meridian plane. One may note that the elastic region in tension, also defined by the St. Venant multi-surface criterion, is directly followed by softening. The latter, however, has an order-of-magnitude smaller dissipation from ductile failure with fracture process zone and softening in compression.

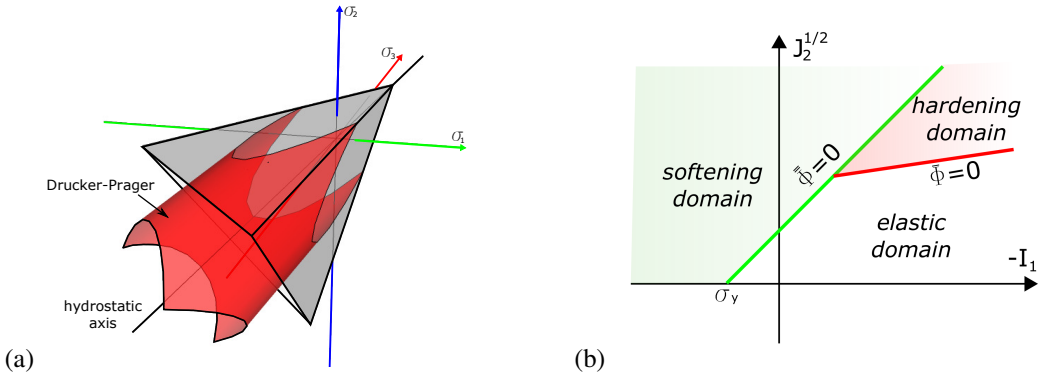

Figure 5: Multi-surface macro-scale plasticity criterion combining Drucker-Prager and St. Venant that can capture both hardening and softening (a) illustration in principal stress space (b) illustration in meridian plane

It is now well understood that softening phenomena require a special finite element interpolation referred to as embedded discontinuity [88, 39], which can provide a sharp representation of the crack. What is less well understood is the kind of modification that such an embedded discontinuity approach provides to the representation of the total plastic dissipation: 'smeared' in the fracture process zone (FPZ) and 'sharp' over a macro-crack [31]. In order to provide an appropriate interpretation of the localized plastic deformation, we consider the macro-element domain $\mathcal{V} = \mathcal{V}^e$ as split into two sub-domains $\mathcal{V}^+$ and $\mathcal{V}^-$ by a crack as a surface of discontinuity. The total displacement field $\boldsymbol{u}$ is written as the sum of a smooth regular part $\bar{\boldsymbol{u}}$ and the displacement discontinuity $\bar{\bar{\boldsymbol{u}}}$, centered at the discontinuity Γ_s. For the surface of discontinuity, one can define at each point a unit exterior normal vector $\boldsymbol{n}$, a tangential vector $\boldsymbol{m}$, and the binormal vector $\boldsymbol{b}$. The discontinuous displacement field can then be written as

$$\boldsymbol{u}(\boldsymbol{x},t) = \bar{\boldsymbol{u}}(\boldsymbol{x},t) + \bar{\bar{\boldsymbol{u}}}(t) M_{\Gamma_s}(\boldsymbol{x}); \qquad M_{\Gamma_s}(\boldsymbol{x}) = H_{\Gamma_s}(\boldsymbol{x}) - N_{\tilde{\mathcal{V}}^+}(\boldsymbol{x}),$$

where $H_{\Gamma_s}(\boldsymbol{x})$ is the Heaviside function being equal to 1 in $\mathcal{V}^+$ and to 0 in $\mathcal{V}^-$, whereas $N_{\tilde{\mathcal{V}}^+}(\boldsymbol{x})$ is the sum of chosen shape functions which leaves only the regular part of the displacement field at the nodes. It is important to note that such a representation of a macro-crack can in general never match the rough surface of the true crack at the fine-scale (see Figure 6); however, the proposed macro-scale model can rather match the corresponding plastic dissipation, which is a typical choice for a Quantity of Interest (QoI) in comparing these two models at different scales.

The deformation field in an element with embedded discontinuity can be decomposed into a regular and a singular part:

$$\boldsymbol{\epsilon}(\boldsymbol{x},t) = \underbrace{\nabla^s \bar{\boldsymbol{u}}(\boldsymbol{x},t) + \bar{\boldsymbol{G}}(\boldsymbol{x})\bar{\bar{\boldsymbol{u}}}(t)}_{\bar{\boldsymbol{\epsilon}}=\bar{\boldsymbol{\epsilon}}^e+\bar{\boldsymbol{\epsilon}}^p} + \underbrace{(\bar{\bar{\boldsymbol{u}}}(t)\otimes\boldsymbol{n})^s}_{\bar{\bar{\boldsymbol{\epsilon}}}^p=\alpha\boldsymbol{m}\otimes\boldsymbol{n}} \delta_\Gamma(\boldsymbol{x}); \qquad \bar{\boldsymbol{G}}(\boldsymbol{x}) = -\nabla^s N_{\tilde{\mathcal{V}}}(\boldsymbol{x}),$$

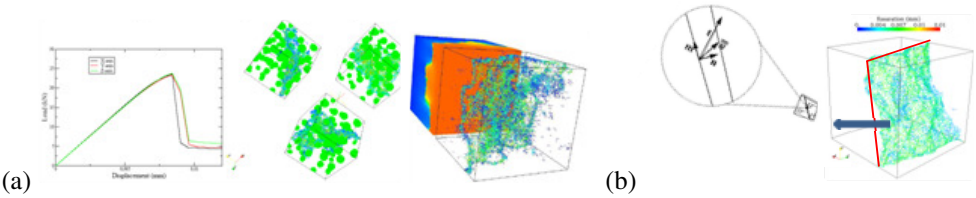

Figure 6: (a) simple tension test force-displacement diagram (statistically isotropic=same in any direction) and the failure mode in tension illustrated with displacement contours and cohesive link failure; (b) replacement of tension failure mode at the meso-scale (rough surface) with a discontinuity (plane) at macro-scale with ED-FEM, not matching perfectly the crack but rather the fracture energy material parameter $G_{f,t}$.

where the singular part is used to represent the localized plastic deformation by means of the Dirac-delta function $\delta_\Gamma(\boldsymbol{x})$. The element strain energy in this case can be written as:

$$\Psi_{\tilde{\mathcal{V}}} := \int_{\tilde{\mathcal{V}}} \psi(\boldsymbol{\epsilon}, \bar{\zeta}, \bar{\bar{\zeta}})\, \mathrm{d}V = \int_{\tilde{\mathcal{V}}} \underbrace{\bar{\psi}^e(\boldsymbol{\epsilon}^e, \bar{\zeta})}_{regular}\, \mathrm{d}V + \int_{\Gamma_s} \bar{\bar{\Xi}}(\bar{\bar{\zeta}})\, \mathrm{d}A, \tag{24}$$

where the first term is the elastic energy with hardening, and the second term is the contribution of the softening mechanisms. The total plastic dissipation is computed from the non-local form of the second principle of thermodynamics applied over the macro-scale element, which can be formulated as:

$$0 \leq D^p_{\tilde{\mathcal{V}}} = \int_{\tilde{\mathcal{V}}} \left[\boldsymbol{\sigma} \cdot \dot{\boldsymbol{\epsilon}} - (\dot{\psi}^e(\boldsymbol{\epsilon}^e) + \dot{\bar{\bar{\Xi}}}(\bar{\zeta}))\right] \mathrm{d}V + \int_{\Gamma_s} [\boldsymbol{t} \cdot \boldsymbol{m}]\, \dot{\alpha}\, \mathrm{d}A - \int_{\Gamma_s} \dot{\bar{\bar{\Xi}}}(\bar{\bar{\zeta}})\, \mathrm{d}A.$$

Provided we enforce the weak form of the Cauchy principle connecting the stress in the fracture process zone with the traction at the discontinuity

$$\int_{\tilde{\mathcal{V}}} \boldsymbol{\sigma} \cdot \tilde{\boldsymbol{G}} \boldsymbol{m} \dot{\alpha}\, \mathrm{d}V + \int_{\Gamma_s} (\boldsymbol{t} \cdot \boldsymbol{m})\, \dot{\alpha}\, \mathrm{d}A = 0, \tag{25}$$

we can further obtain the additive decomposition of the total plastic dissipation into a regular part in the fracture process zone (FPZ) in $\mathcal{V}$, and a singular part at the crack surface Γ_s:

$$D^p_{\tilde{\mathcal{V}}} = \int_{\tilde{\mathcal{V}}} \left(\boldsymbol{\sigma} \cdot \dot{\boldsymbol{\epsilon}}^p + \bar{q}\dot{\bar{\zeta}}\right) \mathrm{d}V + \int_{\Gamma_s} \bar{\bar{q}}\dot{\bar{\bar{\zeta}}}\, \mathrm{d}A. \tag{26}$$

The yield condition controlling the evolution of the inelastic deformation at the discontinuity is set directly in terms of the traction vector:

$$\bar{\bar{\phi}}(t_m, \bar{\bar{q}}) = |\underbrace{\boldsymbol{t} \cdot \boldsymbol{m}}_{t_m}| - (\sigma_y - \bar{\bar{q}}), \tag{27}$$

where σ_y is a localized failure threshold, and $\bar{\bar{q}}$ is the internal variable for softening. When choosing the exponential constitutive law for softening, we define a stress like internal variable for softening plasticity as:

$$\bar{\bar{q}} = \sigma_y \left(1 - \exp\left(-\bar{\bar{\zeta}} \frac{\sigma_y}{G_f}\right)\right), \tag{28}$$

where G_f is the corresponding value of the fracture energy. At the level of the meso-scale model, the compressive and the tension failure mechanisms are reproduced according to the same fracture mode driven by the principal tensile strains. However, at the present macro-scale, the corresponding amount of fracture energy can be quite different due to the number of cracks created in those two cases. This can be handled by modifying in (28) how to compute the fracture energy change from a value in tension $G_{f,t}$ to that in compression $G_{f,c}$ in agreement with the dominant elastic strain:

$$G_f = \frac{G_{f,c} + G_{f,t}}{2} - \frac{G_{f,c} - G_{f,t}}{2} \tanh(c\, \mathrm{tr}\, [\boldsymbol{\epsilon}^e]),$$

where c is a constant value that can be taken different from one in order to ensure a more rapid transition towards the correct value of fracture energy with $-1 \leq \tanh(x) \leq +1$. In the case where the fracture process zone and the macro crack are both active, we assume the most general form of plastic deformation with the plastic multiplier that takes the form $\dot{\gamma} = \dot{\bar{\gamma}} + \dot{\bar{\bar{\gamma}}}\delta_{\Gamma_s}$. The principle of maximum plastic dissipation has to now be enforced in a non-local form (for the complete macro-scale element domain V), which includes the embedded-discontinuity crack representation

$$\bar{\bar{L}}^p_{\mathcal{V}}(\boldsymbol{\sigma}, \bar{q}, \bar{\bar{q}}, \dot{\bar{\bar{\gamma}}}) = \max_{\dot{\bar{\bar{\gamma}}} \geq 0} \min_{(t^*, \bar{\bar{q}}^*)} \left[\bar{\bar{L}}^p_{\mathcal{V}}(\boldsymbol{\sigma}^*, \bar{q}^*, \bar{\bar{q}}^*, \dot{\bar{\bar{\gamma}}}^*) \right] = -D^{loc}_{\mathcal{V}} + \int_{\mathcal{V}} \dot{\bar{\gamma}} \bar{\Phi} \, \mathrm{d}V + \int_{\Gamma_s} \dot{\bar{\bar{\gamma}}} \bar{\bar{\Phi}} \, \mathrm{d}A.$$

The corresponding Kuhn-Tucker optimality condition will provide the global form of the evolution equations for both hardening variables:

$$\begin{aligned} 0 &= \int_{\mathcal{V}} \left(-\dot{\bar{\boldsymbol{\epsilon}}}^p + \dot{\bar{\gamma}} \frac{\partial \bar{\phi}}{\partial \boldsymbol{\sigma}} \right) \mathrm{d}V; \\ 0 &= \int_{\mathcal{V}} \left(-\dot{\bar{\zeta}}^p + \dot{\bar{\gamma}} \frac{\partial \bar{\phi}}{\partial \bar{q}} \right) \mathrm{d}V; \end{aligned} \tag{29}$$

and for the softening internal variable

$$0 = \int_{\Gamma_s} \left(-\dot{\bar{\bar{\zeta}}} + \dot{\bar{\bar{\gamma}}} \frac{\partial \bar{\bar{\phi}}}{\partial \bar{\bar{q}}} \right) \mathrm{d}A.$$

The plastic multiplier governing the softening can be computed from enforcing the plastic consistency condition, resulting in:

$$\int_{-_f} \dot{\bar{\bar{\gamma}}} \dot{\bar{\bar{\phi}}} \, \mathrm{d}A = 0 \quad \Rightarrow \quad \dot{\bar{\bar{\gamma}}} = \frac{1}{\bar{\bar{K}}} \int_{\mathcal{V}} \dot{\boldsymbol{\sigma}} \cdot \bar{\boldsymbol{G}} \boldsymbol{m} \, \mathrm{d}V.$$

The finite element implementation of such a macro-scale model in a deterministic setting is based on a standard semi-discretization procedure [34], with the finite-element-based displacement approximation over a single element domain $\mathcal{V}$ given by:

$$\boldsymbol{u}(\boldsymbol{x}, t)\,|_{\mathcal{V}} = \sum_{a=1}^{n_{en}} \boldsymbol{N}^e_a(\boldsymbol{x}) \boldsymbol{u}_a(t) \;\Rightarrow\; \boldsymbol{\epsilon}(\boldsymbol{x}, t)\,|_{\mathcal{V}} = \sum_{a=1}^{n_{en}} \boldsymbol{B}^e_a(\boldsymbol{x}) \boldsymbol{u}_a(t),$$

where n_{en} is the total number of element nodes, $\boldsymbol{N}^e_a(\boldsymbol{x})$ are the finite element shape functions, $\boldsymbol{B}^e_a(\boldsymbol{x})$ are the symmetric part of their gradients, and $\boldsymbol{u}_a(t)$ are the nodal displacements. By replacing this discrete approximation into the weak form of the equilibrium equations, and integrating with respect to the space variables $\boldsymbol{x}$, one can trace the pseudo-time history of the state variables in agreement with a given loading program:

$$\boldsymbol{r}_u(t) := \mathop{\mathrm{A}}_{e=1}^{n_{el}} \left\{ \int_{\mathcal{V}^e} \boldsymbol{B}^{eT}_a(\boldsymbol{x}) \boldsymbol{\sigma}(\boldsymbol{\epsilon}(\boldsymbol{x}, t), \boldsymbol{\epsilon}^p(\boldsymbol{x}, t), \zeta(\boldsymbol{\xi}, t)) \, \mathrm{d}V - \int_{\mathcal{V}^e} \boldsymbol{N}^e_a(\boldsymbol{x}) \cdot \boldsymbol{b}(\boldsymbol{x}, t) \, \mathrm{d}V - \int_{\Gamma_\sigma} \boldsymbol{N}^e_a(\boldsymbol{x}) \cdot \boldsymbol{t}(\boldsymbol{x}, t) \, \mathrm{d}A \right\} = \boldsymbol{0}.$$

By further choosing a Gauss quadrature rule with n_{in} points, with abscissas $\boldsymbol{\xi}_\ell$, and integration weights w_ℓ, one can significantly reduce the computation for the evolution of internal variables to a finite number of numerical integration points:

$$\boldsymbol{r}_u(t) := \mathop{\mathrm{A}}_{e=1}^{n_{el}} \left\{ \sum_{\ell=1}^{n_{in}} w_\ell \left(\boldsymbol{B}^{eT}_a(\boldsymbol{\xi}_\ell) \boldsymbol{\sigma}(\boldsymbol{\epsilon}(\boldsymbol{\xi}_\ell, t), \boldsymbol{\epsilon}^p(\boldsymbol{\xi}_\ell, t), \zeta(\boldsymbol{\xi}_\ell, t)) - \boldsymbol{N}^e_a(\boldsymbol{\xi}_\ell) \cdot \boldsymbol{b}(\boldsymbol{\xi}_\ell, t) \right) j(\boldsymbol{\xi}_\ell) - \sum_{\ell=1}^{n_{in}} w_\ell \boldsymbol{N}^e_a(\boldsymbol{\xi}_\ell) \cdot \boldsymbol{t}(\boldsymbol{\xi}_\ell, t) j_\Gamma(\boldsymbol{\xi}_\ell) \right\} = \boldsymbol{0}. \tag{30}$$

where $j(\boldsymbol{\xi}_\ell)$ and $j_\Gamma(\boldsymbol{\xi}_\ell)$ are, respectively, volume and surface Jacobian values needed for change to isoparametric coordinates; see [34]. In the softening phase, the finite element approximation should be enhanced by taking into account a displacement discontinuity evolution $\boldsymbol{\alpha}(t)$, which can be done by using the incompatible mode methods [30]; namely, first we choose:

$$\boldsymbol{u}^h(\boldsymbol{x}, t)|_{\mathcal{V}} = \sum_{a=1}^{n_{en}} \boldsymbol{N}_a(\boldsymbol{x}) \boldsymbol{u}_a(t) + \boldsymbol{M}(\boldsymbol{x}) \boldsymbol{\alpha}(t),$$

where $\boldsymbol{M}(\boldsymbol{x})$ are the discontinuous interpolation functions. With such a discrete approximation, we can construct the finite element approximations of the real and virtual strain fields:

$$\boldsymbol{\epsilon}^h(\boldsymbol{x},t)|_{\mathcal{V}^e} = \boldsymbol{B}(\boldsymbol{x})\boldsymbol{u}_a(t) + \boldsymbol{G}_v(\boldsymbol{x})\boldsymbol{\alpha}(t); \quad \delta\boldsymbol{\epsilon}^h(\boldsymbol{x})|_{\mathcal{V}^e} = \boldsymbol{B}(\boldsymbol{x})\delta\boldsymbol{u}_a + \delta\boldsymbol{\alpha}\boldsymbol{G}_v(\boldsymbol{x}); \qquad \int_{\mathcal{V}^e} \boldsymbol{G}_v(\boldsymbol{x})\,\mathrm{d}V = 0,$$

where $\delta\boldsymbol{u}_a$ and $\delta\boldsymbol{\alpha}$ denote, respectively, the virtual displacement field and incompatible modes variations, and $\boldsymbol{G}_v(\boldsymbol{x})$ is a strain-incompatible-modes matrix, which needs to be modified for interpolation of the virtual strain field in order to pass the patch test [34]. The corresponding part of the residual related to the embedded discontinuity evolution in each element with active crack can be written as:

$$\boldsymbol{r}_\alpha(t) := \left\{ \sum_{\ell=1}^{n_{in}} w_\ell \left(\boldsymbol{G}_v^{eT}(\boldsymbol{\xi}_\ell)\,\boldsymbol{\sigma}(\boldsymbol{\epsilon}(\boldsymbol{\xi}_\ell,t), \boldsymbol{\epsilon}^p(\boldsymbol{\xi}_\ell,t), \zeta(\boldsymbol{\xi}_\ell,t))\, j(\boldsymbol{\xi}_\ell) - \boldsymbol{t}_a^e(\boldsymbol{\xi}_\ell) \right) \right\} = \boldsymbol{0}. \tag{31}$$

By gathering all the state variables of the previous model in the variable u, the evolution equations of this kind — depending on the parameter p — can formally be written as: $\partial u(t)/\partial t + A(p;u(t)) = f(p;t)$, cf. (32) in the following section. There such a formulation will be used for the identification of the material parameters.

4. Stochastic identification of macro-scale plasticity model parameters by Bayesian inference

In this section it is explained how to obtain an efficient approximation of the inelastic response computed by the meso-scale model in terms of a macro-scale reduced model of stochastic elasto-plasticity. The elastic part of the macro-scale response will match the elastic response with respect to the strain energy as QoI, thereby achieving with Bayesian inference a homogenization-type result (e.g. [80] or [51]) in a probabilistic setting, which is more appropriate when the separation of scales no longer applies.

The inelastic response is connected with irreversibility, hence with the production of entropy; and as the present model does not include any inertial or thermal effects, the total loss of stored energy appears as dissipation. To match the inelastic response obtained by the meso-scale model with the QoI chosen as plastic dissipation, both as regards the FPZ with plastic hardening and as regards the localized failure in the softening regime, a particular macro-scale ED-FEM stochastic plasticity model provides the most appropriate surrogate. The Bayesian inference for both the elastic and the plastic response will provide the probability distribution of the resulting surrogate model parameters, which are defined as random variables (RV). The latter represent the bulk modulus, shear modulus, yield stress, angle of internal friction, angle of internal dilatancy, ultimate stress, and the fracture energies in tension and in compression, which are denoted respectively as $p(\omega) = (K(\omega), G(\omega), \sigma_y(\omega), \beta(\omega), \tan\phi(\omega), \tan\psi(\omega), \sigma_u(\omega), G_{f,t}(\omega), G_{f,c}(\omega))$. In the computational setting, we rather consider a $\log(\cdot)$-transformation of each parameter — i.e. we consider and identify for example $K_l(\omega) := \log(K(\omega)/K_0)$ instead of the bulk modulus $K(\omega)$, where K_0 is some reference value — in order to accommodate the constraint that $K(\omega) > 0$. The log-quantity K_l is a free variable without any constraint, and in the mechanical computation one uses the point-wise back-transformation, e.g. $K(\omega) = K_0 \exp(K_l(\omega))$.

In Bayesian inference computations, meso- and macro-scale models are matched in terms of their representation of the QoI, which is chosen as a functional (of the reduced model parameters) and further denoted as $Y(\cdot)$, which should obviously be defined of comparable nature at both scales. This inverse problem of determining which value of $p(\omega)$ caused an observed response in general is often an ill-posed optimization approach, which requires regularization procedures when approached in a deterministic framework, see e.g. [15, 16, 43]. In the Bayesian approach [94] the problem is well posed; but the cost for this is that the problem size is vastly increased due to a stochastic formulation, so that efficient numerical approximations are necessary [57]. When viewed vis-a-vis deterministic optimisation approaches it can in the simplest cases be regarded as an alternative manner of a regularization.

4.1. The identification set-up

The situation presents itself in the following way: On the meso-scale, one has the evolution of a system which was described in Section 2 — the mechanical description summarized in Subsection 2.1 and in more detail in [41, 65], and the stochastic modelling in terms of random fields (RFs) in Subsection 2.2 — under a given loading program, which, as it happens computationally, may be viewed as a virtual experiment. The quantities at the meso-scale will

be labelled with a subscript m — like for example p_m to describe the meso-scale parameter RFs. For the macro-scale behaviour and system which we want to identify from an upscaling the subscript M will be used. As already indicated in the previous Section 3, both systems can be written as an abstract evolution equation

$$\frac{\partial u(t)}{\partial t} + A\left(p(\omega); u(t)\right) = f\left(p(\omega); t\right), \tag{32}$$

where the loadings or actions f describe the virtual experiment. The parameters p_m on the meso-scale are known, whereas the parameters p_M for the upscaled reduced order model have to be identified. One part of these parameters one may envision as being known and signify 'controls' on both scales, i.e. something one can influence and hence it is known exactly. The other part, denoted by $q \in \mathcal{Q}$, is that component of the parameters p_M which we cannot control and where we are uncertain about their best value in order to match the response of the meso-scale. To be more specific, these parameters are needed to carry out the macro-scale prediction computation by solving the set of evolution equation for the state $u(t) \in \mathcal{U}$ at time $t \in [0, T]$ in the weak form in (30) and (31), and internal variable flow equations in (22), for any loading program. In the following we shall only track the dependence on the uncertain part q, trying to obtain their probability distribution and thus reduce their uncertainty.

To reduce the uncertainty about q means to match the response as given from the values of the meso-scale model for stored and dissipated energy in each loading increment. As the models are of very different nature — e.g. the meso scale model does not even have a quantity like a continuous stress — the QoI have been chosen as something which will be present in any physics-based model, namely the thermodynamic resp. statistical mechanics quantities of stored and mechanically dissipated energy in each loading increment. Abstractly, the 'measurements' are $\hat{y} \in \mathcal{Y}$, where $\mathcal{Y}$ is the space of all possible measurements, typically some $\mathbb{R}^k$, assuming that the measurement consists of k real numbers each time it is observed. In addition to the mathematical model (32) describing the state evolution, one has to make a corresponding model for the observations or measurements. Hence the mathematical model for the observation is defined as a quantity of interest (QoI) as a function of the state of the system. For the two scales together with the respective evolution equations they are

$$\frac{\partial u_m(p_m(\omega); t)}{\partial t} + A_m\left(p_m(\omega); u_m(p_m(\omega); t)\right) = f_m\left(p_m(\omega); t\right), \tag{33}$$

$$\left(t, p_m(\omega)\right) \to Y_m(t, u_m(p_m(\omega); t), p_m(\omega)) \in \mathcal{Y}, \tag{34}$$

$$\frac{\partial u_M(q(\omega, \vartheta, \epsilon); t)}{\partial t} + A_M\left(q(\omega, \vartheta, \epsilon); u_M(q(\omega, \vartheta, \epsilon); t)\right) = f_M\left(q(\omega, \vartheta, \epsilon); t\right), \tag{35}$$

$$\left(t, q(\omega, \vartheta, \epsilon), \epsilon\right) \to Y_M(t, u_M(q(\omega, \vartheta, \epsilon); t), q(\omega, \vartheta, \epsilon), \epsilon) \in \mathcal{Y}. \tag{36}$$

Here (33) is the more detailed form of (32) of the meso-scale evolution as described in Subsection 2.2, and (34) is the mathematical model describing the possible observations $\hat{y}_m$ of the meso-scale model. We recall that the variable ω describes the aleatoric randomness on the meso-scale, so this means that (33) and (34) are a mathematical model which takes into account a *whole ensemble* or *all possible realizations* of meso-structures. This also means that the response of the meso-structure is a random variable, which can be computationally represented in different ways. If one were to identify just *one specimen*, this would be the case of (33) and (34) for one fixed value of $\varpi \in \Omega$. On the other hand, (35) is the more detailed form of (32) of the macro-scale evolution as described in Section 3, and (36) is the mathematical model describing the quantity on the macro-scale which has to match the one on the meso-scale in (34). The term $\epsilon = \epsilon(\vartheta)$ is a probabilistic error to model discrepancies between the meso- and the macro-scale models, as the upscaled reduced order macro-model will not be able to match the meso-scale model perfectly. As one tries to identify q in (35) from observations of (34), this is the right place to stress the difference between identifying the parameters for a *single* meso-scale specimen or realization — i.e. for a fixed value of the aleatoric variable $\varpi \in \Omega$ [81, 82, 83] — and identifying the parameters for a whole *ensemble* of meso-scale structures, i.e. for *all* values of the aleatoric variable $\omega \in \Omega$ describing the meso-scale variability [77, 84]. In the first case the unknown quantity q will be a random variable due to the epistemic uncertainty modeled by the variable ϑ, whereas in the second case the unknown quantity q will be a random variable due to the aleatoric randomness of the meso-scale described by ω and the probabilistic scale mismatch or model error given by ϵ, as well as the epistemic uncertainty of identification expressed through the variable $\vartheta \in \Theta$, where Θ is some probability space appropriate for the epistemic uncertainties.

One might say that in the first case one obtains an epistemically uncertain *constant*, whereas in the second case one obtains an epistemically uncertain *aleatoric random variable*.

It seems natural that we would be interested in choosing the parameter q such as to make the difference $\hat{y} - Y_M(u_M(q;t), q, \epsilon)$ as small as possible. The task of predicting the state $u_M(q;t)$ for given q and t from (35), and subsequently a prediction or forecast for the observation $Y_M(u_M(q;t), q, \epsilon)$ from (36) is called the forward problem. We shall assume that this is a well-posed problem in the sense of Hadamard for all possible values of $q \in \mathcal{Q}$.

To glean information about q from observing $\hat{y}$, one has to in some way invert the mapping in (34) $q \to Y_M(q)$, where we have neglected the other variables for the sake of concise notation. This is called the *inverse* problem, and as the mapping $q \to Y_M(q)$ is usually not invertible, the inverse problem is ill-posed [15, 16, 94]. To approach ill-posed problems computationally directly is typically ill-advised, as it is numerically unstable and hence would produce unreliable results. This means that one has to add some additional information to the situation for the inverse problem to become reliable and numerically stable. The *regularization* approach, e.g. [15, 16], is a proposed solution to this by making $q \in \mathcal{Q}$ in some way regular — hence the name — by desiring that the parameter be in some more *regular* subset $q \in \mathcal{Q}_0 \subset \mathcal{Q}$, and typically penalizing deviations from $\mathcal{Q}_0$. The regularization proposed here proceeds by widening the problem of finding the best q to a larger class of problems, where the knowledge about q is described probabilistically through the variable $\vartheta \in \Theta$. More precisely, this means that one wants to update the probability distribution describing the knowledge about q to include the new information gained from observing $\hat{y}$. These updates rest on *Bayes's theorem* — e.g. [94] — and are thus called *Bayesian updates*. There are intimate connections between the two approaches, with the main view being that the probabilistic approach gives some explanations of background information for otherwise seemingly ad-hoc decisions which have to be taken in the regularization approach. The description of the general Bayesian updating procedure [75, 57, 76, 58, 59] can be summerized as follows. Proceeding from computed results by the mathematical model in (33), and the measurement or observation operator defined in (34), for simplicity we envisage observations $\hat{y}_n$ at discrete times $0 < t_1 < \cdots < t_n, \cdots \in [0, T]$, different realizations of which can be predicted by the parametric model (35) and the observation prediction operator (36)

$$y_n := Y_M(u(q;t_n), q, \epsilon), \quad n = 1, \ldots. \tag{37}$$

From these observation one would like to obtain at each instant t_n both a new — and hopefully better — estimate for q and for the state $u(q;t_n)$. In the Bayesian framework (e.g. [94]) this is done by modelling the uncertainty about the value of q probabilistically as a random variable $q : \Theta \to \mathcal{Q}$ on a probability space $(\Theta, \mathfrak{A}, \mathbb{P})$. So the observation or measurement is a sequence of samples of Y_m in (34), $\hat{\boldsymbol{y}} = (\hat{y}_1, \ldots, \hat{y}_n, \ldots, \hat{y}_N) \in \mathcal{Y}^N$. With such a sequence of observations, there are different ways how the update can be done. The simplest is to assume that after each observation we perform an update of the knowledge about q; this is one extreme where updating would proceed in a purely sequential manner after each observation:

1. start with the *prior* $q_0(\theta)$ as *forecast* $q_f(\theta, \epsilon) = q_0(\theta)$, and set $n = 0$;
2. **loop** over $n := n + 1$;
3. *forecast* or predict the observation at t_n as a RV $y_f(\theta, \epsilon) = Y_M(u_M(q_{n-1}(\theta, \epsilon), t_n), q_{n-1}(\theta, \epsilon), \epsilon)$ from (37);
4. observe or measure $\hat{y}_n = Y_m(t_n, u_m(t_n), p_m)$ at time t_n as described in (34);
5. from y_f and $\hat{y}_n$ update the *forecast* $q_f(\theta, \epsilon) = q_{n-1}(\theta, \epsilon)$ to the *assimilated* $q_a(\theta, \epsilon)$, and set $q_n(\theta, \epsilon) = q_a(\theta, \epsilon)$;
6. **endloop**

At the extreme other end one could update all in one step after the results of the whole loading programme has been gathered:

1. from the prior or *forecast* $q_f(\theta, \epsilon) = q_0(\theta)$ predict or forecast the observations $\boldsymbol{y}_f(\theta, \epsilon) = (y_1(\theta, \epsilon), \ldots, y_N(\theta, \epsilon))$ from (37) at times $t_1, \ldots, t_N$;
2. observe or measure all the values $\hat{\boldsymbol{y}} = (\hat{y}_1, \ldots, \hat{y}_N)$ at times $t_1, \ldots, t_N$ from (34);
3. from $\hat{\boldsymbol{y}}$ and $\boldsymbol{y}_f(\theta, \epsilon)$ update the *forecast* $q_f(\theta, \epsilon)$ to the *assimilated* $q_a(\theta, \epsilon)$.

The steps 1–3 in this last algorithm are formally analogous to the steps 3–5 of the preceding sequential algorithm, just the forecast and observation vectors are larger in the last all-in-one update procedure. Obviously, it is also possible to mix the purely sequential and the all-in-one procedures by updating in batches several times. The best strategy depends on the particular problem at hand. If we want to identify the probability distribution of parameters

in $q = (K, G, \sigma_y, \beta, \tan(\phi), \tan(\psi), \sigma_u, G_{f,t}, G_{f,c})$, not only can we split the choice of the quantity of interest Y into a corresponding sequence of separating parameters governing the elastic, hardening, and softening response [43], but we can also split the time sequence of realizations and the loading program to privilege a certain type of response. If the updating is used to control the particular loading program and the response of the system (33), one would most probably choose the purely sequential procedure.

Hence we will focus on just one step, knowing the *forecast* RV $q_f(\theta, \epsilon)$, predicting or forecasting the observation RV $\boldsymbol{y}_f(\theta)$ — which may be just $\boldsymbol{y}_f(\theta, \epsilon) = y_n(\theta, \epsilon)$, or $\boldsymbol{y}_f(\theta, \epsilon) = (y_1(\theta, \epsilon), \dots, y_N(\theta, \epsilon))$ — and observing the corresponding measurement $\hat{\boldsymbol{y}}$, we perform the update of the forecast $q_f(\theta, \epsilon)$ to the assimilated $q_a(\theta, \epsilon)$, i.e. the information or knowledge of the observation $\hat{\boldsymbol{y}}$ has been *assimilated* into the system. Two methods of Bayesian updates will be considered: the first is the MCMC (Markov chain Monte Carlo) method [23, 21, 75] which updates the probability measure on Θ and keeps the RV $q(\theta, \epsilon)$, and the second is referred to as the Gauss-Markov-Kálmán filter (GMKF) [75, 57, 76, 58, 59], which keeps the same measure but updates the function $q(\theta, \epsilon)$.

4.2. MCMC Bayesian updating of the measure

Bayes's theorem is considered as the consistent way to update a probabilistic description when new data in the form of observations $\hat{\boldsymbol{y}}$ is available. Probably the best known version of Bayes's theorem is the update of the probability density of q, e.g. [7, 75, 76, 94]. This formulation can be used when all considered quantities have a joint probability distribution [7, 72], which we shall assume from now on. In such case it is possible to state for the *conditional density* $\pi_{(Q|Y)}(q|\boldsymbol{y})$ of q given $\boldsymbol{y}$:

$$\pi_{(Q|Y)}(q|\boldsymbol{y}) = \frac{\pi_{(Q,Y)}(q, \boldsymbol{y})}{\pi_Y(\boldsymbol{y})} = \frac{\pi_{(Y|Q)}(\boldsymbol{y}|q)}{\pi_Y(\boldsymbol{y})}\pi_Q(q), \quad \text{with } \pi_Y(\boldsymbol{y}) = \int_{\mathcal{Q}} \pi_{(Q,Y)}(q, \boldsymbol{y})\, \mathrm{d}q = \int_{\mathcal{Q}} \pi_{(Y|Q)}(\boldsymbol{y}|q)\pi_Q(q)\, \mathrm{d}q, \tag{38}$$

where $\pi_Y(\boldsymbol{y})$ is the pdf of the RV $\boldsymbol{y}$ — the *evidence* — and $\pi_Q(q)$ is the *prior* pdf of q, and $\pi_{(Y|Q)}(\boldsymbol{y}|q)$ is the *likelihood* of $y = Y(q, \epsilon)$ given q. The second part of the equations in (38) comes from factoring the joint density into the likelihood and the prior: $\pi_{(Q,Y)}(q, \boldsymbol{y}) = \pi_{(Y|Q)}(\boldsymbol{y}|q)\pi_Q(q)$, which is how the joint pdf is typically available.

The statements in (38) are formally correct both for the case where one wants to make a parameter update for just one realization or specimen of the meso-scale, and for the case where one seeks to update the parameters for a whole ensemble of aleatoric variable meso-structures, but the interpretation of the terms in (38) will be different. In the first case the likelihood $\pi_{(Y|Q)}(\boldsymbol{y}|q)$ in (38) contains only the epistemic uncertainty, whereas in the second case it contains also the aleatoric uncertainty. The first case, identification without taking aleatoric uncertainty into account, resp. identification for just one realization $\varpi \in \Omega$, is the usual and more familiar case. In computational upscaling it would be possible to "observe" a whole random variable — a function of the aleatoric variable $\omega \in \Omega$ — and use Bayes's formula in such a way. Instead here we shall concentrate on a simple scheme which can be applied also in experimental situations, where one can only observe samples of the aleatoric distribution, although more involved schemes are possible [77, 84]. The proposed scheme builds on employing the usual Bayesian methods for identifying parameters for a single specimen or realisation $\varpi \in \Omega$, so after some general consideration this will be described first.

The Bayes formula for conditioning (38) is used in the following way for an identification of just one specimen, i.e. realization $\varpi \in \Omega$: after observing $\hat{\boldsymbol{y}}$, the *posterior* pdf of q is given by $\pi_{(Q|Y)}(q|\hat{\boldsymbol{y}})$. Observe from (38) that Cromwell's rule — who famously wrote "…consider it possible that you might be mistaken" — is visible here: if $\mathcal{I}_q \subset \mathcal{Q}$ is assigned a vanishing prior pdf, i.e. $\pi_Q(q) = 0$ for $q \in \mathcal{I}_q$, then no matter what the evidence in the Bayes-factor $\pi_{(Y|Q)}(\boldsymbol{y}|q)/\pi_Y(\boldsymbol{y})$ for pdfs, the posterior $\pi_{(Q|Y)}(q|\boldsymbol{y})$ will also always be identically zero on $\mathcal{I}_q \subset \mathcal{Q}$.

Let us point out that to evaluate (35), one may assume that the prior $\pi_Q(q)$ is given. However, to evaluate the conditional pdf or likelihood $\pi_{(Y|Q)}(\boldsymbol{y}|q)$, for each given q one has to solve for the model response and evaluate the forecast measurement in (36). This computational expense is amplified when the evidence $\pi_Y(\boldsymbol{y})$ in (38) has to be evaluated, as it is a often high-dimensional integral over $\mathcal{Q}$, requiring typically many evaluations of the likelihood.

Therefore most computational approaches to determine the pdfs are based on variants which circumvent the direct approach just outlined, and use versions of the Markov-chain Monte Carlo (MCMC) method, e.g. [23, 53, 21, 75], where at least the evidence $\pi_Y(\boldsymbol{y})$ does not have to be evaluated, as these algorithms can evaluate the Bayes-factor directly as a ratio of densities. A simple version of a MCMC algorithm, also known as the Metropolis-Hastings algorithm [23, 21, 62], looks as follows [75]: The main idea is to construct a Markov-chain that has a stationary distribution of states, which will be the posterior distribution one is seeking. For this, the range of possible q's has

to be quantized into X bins of equal background measure, i.e. in case of a Lebesgue background measure of equal Q-volume, with representatives $\{q_\xi\}_{\xi=1}^X$. These representatives of the bins q_ξ are the states of the Markov-chain, which will be denoted by $\{\boldsymbol{\varsigma}_k\}_{k=1,\dots}$ in the order visited at step $k = 1, \dots$ of the Markov-chain. Assuming that $\hat{\boldsymbol{y}}$ has been observed or measured, the Markov-chain steps are the following:

1. draw ξ randomly from $\{1, \dots, X\}$;
2. starting in state q_ξ, set $\boldsymbol{\varsigma}_1 := q_\xi$ and $k := 0$;
3. compute $\rho_\xi := \pi_{(Y|Q)}(\hat{\boldsymbol{y}}|q_\xi)\pi_Q(q_\xi)$; the product of likelihood and prior,
4. **loop** over $k := k + 1$;
5. pick any state q_ζ with $\zeta \neq \xi$ randomly with probability $1/(X-1)$, this is the *proposal*;
6. if not already computed in a previous step, compute $\rho_\zeta := \pi_{(Y|Q)}(\hat{\boldsymbol{y}}|q_\zeta)\pi_Q(q_\zeta)$;
7. let $\alpha = \min\{1, \rho_\zeta/\rho_\xi\}$, this is the *acceptance probability*;
8. accept q_ζ with probability α, i.e. pick a sample of a uniformly distributed RV $U \in [0, 1]$; and
9. **if** $U \leq \alpha$ **then**
10. set $\boldsymbol{\varsigma}_{k+1} = q_\zeta$;
11. **else**
12. set $\boldsymbol{\varsigma}_{k+1} = q_\xi$;
13. **endif**
14. **endloop**

One can then show [62, 23, 53, 21] that after the so-called *burn-in*, i.e. a number of steps which the Markov-chain needs to reach the stationary distribution, the relative frequency with which the states q_ξ are visited is equal to the *posterior* pdf $\pi_{(Q|Y)}(q_\xi|\hat{\boldsymbol{y}})$. One may observe that if the number ρ_ζ in line 6 of the algorithm, the product of likelihood and prior for the proposal state q_ζ is larger than for the current state q_ξ, i.e. $\rho_\zeta \geq \rho_\xi$, one has $\alpha = 1$ in line 7, and the new state is accepted in any case. As the ρ_ξ are proportional to the posterior conditional pdf $\pi_{(Q|Y)}(q_\xi|\hat{\boldsymbol{y}})$ at the representatives q_ξ, it is clear that the algorithm is a probabilistic search for the maximum of the posterior. It moves away from a state to lower posterior values in line 10 of the algorithm according to the posterior ratios. Obviously, one error involved in the algorithm is the quantization into bins and choosing the representatives q_ξ. Due to the required burn-in, one is not sure that the sequence of visited states $\boldsymbol{\varsigma}_k$ is *stationary*, as the equilibrium distribution is only the asymptotic distribution. Estimating that the burn-in period is over has to be tested by looking at the stationarity of the sequence. The main advantages of the method are certainly the simplicity of the formulation and the possibility to directly estimate the posterior conditional pdf $\pi_{(Q|Y)}(q|\hat{\boldsymbol{y}})$. We should warn though, that although the formulation is so simple, to use the method efficiently and correctly may not be. The main drawback of these methods is the potentially expensive step of often having to evaluate the likelihood $\pi_{(Y|Q)}(\hat{\boldsymbol{y}}|q_\zeta)$ in line 6 , and we shall return to this point later. Additionally, the algorithm is a Monte Carlo (MC) method, or more precisely a MC method within a MC-method, meaning that it converges only slowly with the number of samples, so that there will always be a sampling error. In addition, the successive Markov-chain samples are obviously not independent but highly *correlated*. This makes estimating any statistic other than the mean (e.g. the variance) difficult. Also usual statistical formulas for the accuracy of the estimates assume *independent* samples and are not directly applicable. And finally, if the likelihood function and prior pdf differ very much, the acceptance probabilities α in line 7 may be very low, $\alpha \ll 1$, meaning that practically the chain has gets stuck in some state and does not move on.

Assuming that the above MCMC algorithm can successfully be carried out for one particular realization $\varpi \in \Omega$ resp. specimen, we now assume that we have a *Monte Carlo* (MC) sample of such MCMC runs yielding posterior conditional pdfs $\pi_{(Q|Y)}(q|\hat{\boldsymbol{y}}[\omega_z])$ for each MC sample $\omega_z \in \Omega$ for $1 \leq z \leq Z$. For each sample ω_z this is a distribution of $q(\omega_z)$ representing the epistemic uncertainty. The final distribution $\check{\pi}_{(Q|Y)}(q|\hat{\boldsymbol{y}}[\cdot])$ of q representing both the epistemic and aleatoric uncertainty is a *mixture* of the individual MC distributions $\pi_{(Q|Y)}(q|\hat{\boldsymbol{y}}[\omega_z])$, i.e. a *distribution of distributions*. As these are MC samples — each of which carries the same probability $1/Z$ — the mixture distribution is uniform, and this results in

$$\check{\pi}_{(Q|Y)}(q|\hat{\boldsymbol{y}}[\cdot]) = \frac{1}{Z}\sum_{z=1}^{Z} \pi_{(Q|Y)}(q|\hat{\boldsymbol{y}}[\omega_z]). \tag{39}$$

4.3. Bayesian updates with the linear Gauss-Markov-Kálmán filter

Another possibility, which was implicitly already alluded to in the description of the "forecast-observe-assimilate" algorithms above, is to leave the base measure $\mathbb{P}$ resp. pdf $\pi_Q(q)$ unchanged, and to change the RV from the forecast $q_f = q$ to the updated or assimilated q_a. Such algorithms are often called *filters*, as the observation or measurement $\hat{\boldsymbol{y}}$ is filtered to update the forecast q_f to q_a. This is often advantageous if one needs a RV to do further forecast according to (35) and (36), as then the assimilated q_a becomes the new forecast. In these paragraphs it is attempted to sketch the main idea behind the construction of such a filter. More detail can be found e.g. in [57, 7]. It is well known [7, 72, 57] that knowledge of the probability measure $\mathbb{P}$ resp. the pdf $\pi_Q(q)$ is equivalent to knowing the expected values of all reasonable functions $\psi(q)$ of the RV q. The expected value of $\psi(q)$ is defined as usual as

$$\mathbb{E}(\psi(q)) := \int_\Theta \psi(q(\theta))\, \mathbb{P}(\mathrm{d}\theta) = \int_Q \psi(q) \pi_Q(q)\, \mathrm{d}q, \tag{40}$$

and it should be observed that this expectation and the following ones are only carried out by integrating over the probability space Θ describing the epistemic uncertainty; one may regard this whole procedure equally well only carried out for one realization $\varpi \in \Omega$ resp. one specimen, which is the case we consider first just as for the MCMC procedure in the previous Subsection 4.2. From the expectation operator the probability measure can be recovered: the probability of a subset $\mathcal{W} \subset \Theta$ is given by $\mathbb{P}(\mathcal{W}) = \mathbb{E}(\mathbf{1}_\mathcal{W})$, or for a subset $\mathcal{I}_q \subset Q$ by $\mathbb{P}_Q(\mathcal{I}_q) = \mathbb{E}(\mathbf{1}_{\mathcal{I}_q}) = \int_{\mathcal{I}_q} \pi_Q(q)\, \mathrm{d}q$; here $\mathbf{1}_\mathcal{W}(\omega)$ is unity if $\theta \in \mathcal{W}$, and vanishes otherwise. The conditional expectation of the RV $\psi(q)$ under the observation $\hat{\boldsymbol{y}}$ is analogously given by using the *conditional density* $\pi_{(Q|Y)}(q_\xi|\hat{\boldsymbol{y}})$: $\mathbb{E}(\psi(q) \mid \hat{\boldsymbol{y}}) := \int_Q \psi(q) \pi_{(Q|Y)}(q|\hat{\boldsymbol{y}})\, \mathrm{d}q$. This defines the conditional expectation in terms of the conditional pdf $\pi_{(Q|Y)}(q|\hat{\boldsymbol{y}})$, but this is only valid [7, 72] in the cases where a conditional density exists, which is tied to the existence of a joint pdf $\pi_{(Q,Y)}(q, \boldsymbol{y})$ in (38). It was hence turned around by Kolmogorov (who axiomatized probability in terms of measures and densities) himself, and he defined conditional probabilities via the conditional expectation which is thus the mathematically more fundamental notion, and probabilities can afterwards be defined from the expectation and conditional probabilities from the conditional expectation operator [57].

It turns out [57] that the conditional expectation of q is a function $\mathbb{E}(q \mid \boldsymbol{y}_f) = \phi_q(\boldsymbol{y}_f)$ of $\boldsymbol{y}_f$, which induces an orthogonal decomposition

$$q = \mathbb{E}(q \mid \boldsymbol{y}_f) + (q - \mathbb{E}(q \mid \boldsymbol{y}_f)) = \phi_q(\boldsymbol{y}_f(q)) + (q - \phi_q(\boldsymbol{y}_f(q))). \tag{41}$$

This decomposition may be used to build a first version of a filter to produce an assimilated RV q_a which has a correct conditional expectation. As the new information from the observation $\hat{\boldsymbol{y}}$ comes from the measurement map $\boldsymbol{y}_f$ one may define

$$q_a := \phi_q(\hat{\boldsymbol{y}}) + (q_f - \phi_q(\boldsymbol{y}_f(q_f))), \tag{42}$$

where the first component in (41) has been changed to the constant $\phi_q(\hat{\boldsymbol{y}}) = \mathbb{E}(q \mid \hat{\boldsymbol{y}})$, and the orthogonal component $q_f - \phi_q(\boldsymbol{y}_f(q_f))$ has been left as it is. Note that this orthogonal component is a RV, as $q_f(\theta)$ is, whereas $\phi_q(\hat{\boldsymbol{y}})$ is a constant vector. While the RV $\phi_q(\boldsymbol{y}_f)$ is the conditional expectation of q_f, we call the constant $\phi_q(\hat{\boldsymbol{y}})$ the *conditioned expectation*, which can only be computed *after* the observation $\hat{\boldsymbol{y}}$ on which one is conditioning. From the above observation on projections it is clear that in (42) the second summand on the right — the orthogonal component — has a vanishing conditional expectation, and thus q_a has the correct conditional expectation $\mathbb{E}(q_a \mid \hat{\boldsymbol{y}}) = \mathbb{E}(q \mid \hat{\boldsymbol{y}})$. We call q_a in (42) the *analysis*, *assimilated*, or *posterior* RV, incorporating the new information at least in form of the correct conditional expectation, which is in many circumstances the most important part of the update.

One should emphasize that it is the vector space setting of Q and $\mathcal{Y}$ which has made this formulation possible [57], also allowing for easy numerical computation. In case the parameters $q \in Q$ are not without constraints, or not in a vector space, then they should be mapped to such quantities. For example, if q is the elasticity tensor, then it has to be symmetric and positive definite. The symmetric tensors are of course a subspace, but the sub-manifold of positive definite ones is not a subspace, but an open cone and a Riemannian manifold. A simple case of this are positive scalars either used for bulk modulus or shear modulus; through the logarithm they are transformed into a vector space without constraints, and the same is true for positive definite tensors. So the update equation (42) should only be used for these transformed vector-space like quantities.

The function $\phi_q(\boldsymbol{y}_f)$ may not be easy to compute, and usually has to be approximated. But the vector space setting allows a simplification or approximation, and the simplest one is a linear map $\phi_q(\boldsymbol{y}_f) \approx K\boldsymbol{y}_f$. As is well known, the linear orthogonal projector associated with (41) is the *Kálmán-gain* $K \in \mathcal{L}(\mathcal{Y}^N; \mathcal{Q})$, see [40, 52], which is given by:

$$K := C_{q_f,\boldsymbol{y}_f} C_{\boldsymbol{y}_f}^{-1}, \quad \text{with} \quad C_{\boldsymbol{y}_f} := \mathbb{E}(\tilde{\boldsymbol{y}}_f(q_f) \otimes \tilde{\boldsymbol{y}}_f(q_f)) \quad \text{and} \quad C_{q_f,\boldsymbol{y}_f} := \mathbb{E}(\tilde{q_f} \otimes \tilde{\boldsymbol{y}}_f(q_f)), \tag{43}$$

where for any RV like q for the sake of brevity we set $\bar{q} := \mathbb{E}(q)$ such that $\tilde{q} := q - \bar{q}$ is the zero-mean part. So one obtains [74, 68] the so-called *Gauss-Markov-Kálmán* filter (GMKF) as an approximation of (42)

$$q_a := K(\hat{\boldsymbol{y}}) + (q_f - K(\boldsymbol{y}_f(q_f))) = q_f + K(\hat{\boldsymbol{y}}) - K(\boldsymbol{y}_f(q_f)) = q_f + K(\hat{\boldsymbol{y}} - \boldsymbol{y}_f(q_f)). \tag{44}$$

The name of this filter [57, 76, 58, 59] is due to the fact that it is a generalized version of the Gauss-Markov theorem [52], and gives as well a generalization of the well-known Kálmán filter [40]. In case $C_{\boldsymbol{y}_f}$ is not invertible or close to singularity, its inverse in (43) should be replaced by the Moore-Penrose pseudo-inverse. This update is in some ways very similar to the 'Bayes linear' approach, see [24]. If the mean is taken in (44), one obtains the familiar Kálmán filter (KF) formula [40, 52] for the update of the mean. But the filter (44) operates on the random variable and does not require a separate update for the covariance, in fact one may show [74, 68] that (44) also contains the Kálmán update for the covariance and is thus a non-Gaussian generalization of the KF and various of its more recent cousins. It is well known [40] that for everything Gaussian and linear forward and observation models the linear update in (44) is in fact exact and not an approximation.

The above procedure — which is not yet computationally operational, this will be described in the next Subsection 4.4 — is what is carried out for each single realization $\varpi \in \Omega$ resp. one specimen. It describes the update resp. identification considering only the epistemic uncertainty. To describe also the aleatoric uncertainty, we only have to remember that the quantities $q_f, \hat{y}$ in (42) and (44), and hence also y_a and q_a, are functions of the aleatoric variable $\omega \in \Omega$, and those update equations stay formally correct also in this case. For actual computations, this dependence on $\omega \in \Omega$ has to be considered separately, which also will be done in the next Subsection 4.4.

4.4. Discrete approximation and the computational filter

Again, as in Subsection 4.2, first we shall describe the updating resp. identification for just one sample $\varpi \in \Omega$, resp. one specimen. The only variability considered initially is the one due to the epistemic uncertainty $\vartheta \in \Theta$.

Let us point out that the RVs of the macro-model 'live' in the spaces $\mathcal{U} = \mathcal{U} \otimes \mathcal{S}$ and $\mathcal{Q} = \mathcal{Q} \otimes \mathcal{S}$, where $\mathcal{S} = L_2(\Theta)$ is the usual space of scalar RVs on Θ of finite variance. In the instances where we want to employ the theory detailed in the previous sections, the spaces $\mathcal{U}$ and $\mathcal{Q}$ are often infinite dimensional, as is the space $\mathcal{S} = L_2(\Theta)$. For an actual computation they have to be discretized or approximated by finite dimensional spaces. This was already described for the forward problem in Subsection 2.3.

Let $\mathcal{Q}_M := \text{span}\{\varrho_m : m = 1, \dots, M\} \subset \mathcal{Q}$ be an M-dimensional subspace with basis $\{\varrho_m\}_{m=1}^M$. An element of $\mathcal{Q}_M$ will be represented by the vector of RVs $\boldsymbol{q} = \left[q^1, ..., q^M\right]^T \in \mathcal{S}^M$ such that $\sum_{m=1}^M q^m \varrho_m \in \mathcal{Q}_M = \mathcal{Q}_M \otimes \mathcal{S}$. The space of possible measurements $\mathcal{Y}$ can usually be assumed to be finite dimensional, whose elements similarly are represented by a vector of coefficients $\boldsymbol{y} \in \mathbb{R}^R$. Observe that then $\hat{\boldsymbol{y}} \in \mathbb{R}^{R \times N}$ and $\boldsymbol{y}_f \in \mathbb{R}^{R \times N} \otimes \mathcal{S}$.

With this discretization, the MCMC-method can be carried out after the obvious modifications. For the conditional expectation and the GMK filter, things are also straight forward, as is shown next. On $\mathbb{R}^M$, representing $\mathcal{Q}_M$, the update corresponding to (44), more precisely its spatial semi-discretization, is

$$\boldsymbol{q}_a := \boldsymbol{q}_f + \boldsymbol{K}(\hat{\boldsymbol{y}} - \boldsymbol{y}_f(\boldsymbol{q}_f)), \quad \text{with} \tag{45}$$

$$\boldsymbol{K} = \boldsymbol{C}_{\boldsymbol{q}_f,\boldsymbol{y}_f} \boldsymbol{C}_{\boldsymbol{y}_f}^{-1}, \quad \text{with} \quad \boldsymbol{C}_{\boldsymbol{y}_f} = \mathbb{E}(\tilde{\boldsymbol{y}}_f(\boldsymbol{q}_f) \otimes \tilde{\boldsymbol{y}}_f(\boldsymbol{q}_f)) \quad \text{and} \quad \boldsymbol{C}_{\boldsymbol{q}_f,\boldsymbol{y}_f} = \mathbb{E}(\tilde{\boldsymbol{q}}_f\, \tilde{\boldsymbol{y}}_f^T) = \mathbb{E}(\tilde{\boldsymbol{q}}_f \otimes \tilde{\boldsymbol{y}}_f) \tag{46}$$

In case $\boldsymbol{C}_{\boldsymbol{y}_f}$ is singular, its Moore-Penrose pseudo-inverse [70] has to be used. Let us note that, in contrast to the usual Kálmán filter, here the quantities $\boldsymbol{q}_a, \boldsymbol{q}_f$, and $\boldsymbol{y}_f$ in (45) are RVs. With these specifications, a Monte Carlo sampling or particle filter version of (45) can be carried out, this is the *Ensemble Kálmán filter* (EnKF), see [19, 20, 75]. Here we shall follow a different path, by using a *spectral or polynomial chaos projection*, which was already introduced in Subsection 2.2. Namely, sampling the model (32) and the measurement operator (34) or even the spatially discretized RVs $\boldsymbol{y}_f$ which appear in all the algorithms may be computationally quite expensive. Therefore it

is quite natural to try and find simpler representations for this, something what is known often as proxy- or surrogate models. Mathematically we can see this with the variables $q_f \in \mathcal{Q} \otimes \mathcal{S} = \mathfrak{Q}$, $u \in \mathcal{U} \otimes \mathcal{S} = \mathfrak{U}$, and $y_f \in \mathcal{Y} \otimes \mathcal{S} = \mathfrak{Y}$. In the preceding section these were already discretized in the first factor of the tensor product to $\boldsymbol{q}_f \in \mathcal{Q}_M \otimes \mathcal{S}$ and $\boldsymbol{y}_f \in \mathbb{R}^{R\times N} \otimes \mathcal{S}$. As $\mathcal{Y}$ was assumed finite dimensional ($\mathcal{Y} \equiv \mathbb{R}^R$), no further discretization was needed here in the first factor; and $\boldsymbol{y}_f$ — a RV with values in $\mathbb{R}^{R\times N}$ — comes from N measurement of R quantities at a time. Along with the discretization of $\mathcal{Q}_M \subset \mathcal{Q}$ typically one also has to discretize the model (32) in space by $\mathcal{U}_L \subset \mathcal{U}$, something what is standard (e.g. finite elements), and will not be further discussed.

But the second factor in those tensor products, the space of real-valued RVs $\mathcal{S}$, is typically an infinite dimensional space and has to be discretized as well for real computations. In a numerical sense the Monte Carlo sampling alluded to earlier for the EnKF is of course also a discretization. But here we want to introduce another one by explicitly choosing a subspace $\mathcal{S}_B \subset \mathcal{S}$ as was already described for the forward problem in Subsection 2.3. As for $\mathcal{Q}_M$ one picks a finite set $\{\Psi_b\}_{b=1}^B$ of B independent vectors in $\mathcal{S}$ which span the B-dimensional subspace $\mathcal{S}_B = \operatorname{span}\{\Psi_b\}_{b=1}^B$. One may assume without loss of generality that the function / RV $\Psi_1 = 1$ is actually constant, whereas the Ψ_b for $b > 1$ satisfy $\mathbb{E}(\Psi_b) = 0$, as well as that the Ψ_b are orthonormal, i.e. $\mathbb{E}(\Psi_{b_1}\Psi_{b_2}) = \delta_{b_1,b_2}$. As $\mathcal{S} = L_2(\Theta)$, these independent vectors are in fact RVs with finite variance. Here we will use *Wiener's polynomial chaos* expansion (PCE) as basis. This is well-known by now and was used already in Subsection 2.2; further references are in text-books [100] and monographs [50, 90, 37]. Other possibilities [101] are the generalized PCE, or even other systems of RVs which are dense [37] in $\mathcal{S}$. A quantity like $\boldsymbol{q}_f(\theta)$ is then approximated by expanding each $q_f^m(\theta) = \sum_b q_{f,b}^m \Psi_b(\theta)$ and setting

$$\boldsymbol{q}_{f,b} = \left[q_{f,b}^1, \ldots, q_{f,b}^M\right]^\mathsf{T}, \quad \text{giving} \quad \boldsymbol{q}_f(\theta) = \sum_{b=1}^{B} \boldsymbol{q}_{f,b}\Psi_b(\theta). \tag{47}$$

Completely analogous expansions exist for $\boldsymbol{q}_a(\theta)$ and $\boldsymbol{y}_f(\theta)$. Inserting this approximation in (45), one obtains [67, 74, 68, 75, 57, 76, 58, 59] the stochastic discretization of (45):

$$\boldsymbol{q}_{a,1} = \boldsymbol{q}_{f,1} + \boldsymbol{K}(\hat{\boldsymbol{y}} - \boldsymbol{y}_{f,1}), \quad \text{and} \tag{48}$$

$$\boldsymbol{q}_{a,b} = \boldsymbol{q}_{f,b} - \boldsymbol{K}\boldsymbol{y}_{f,b} \quad \text{for } b > 1. \tag{49}$$

The filter in (48) is the classical Kálmán filter (KF) for the mean, the relations in (49) are a non-Gaussian extension of the Kálmán filter, where it can be shown that it really extends the Kálmán filter [67, 74, 68]. This filter is called the *spectral projection* Kálmán-filter (SPKF) or *polynomial chaos* Kálmán-filter (PCKF), where the former (SPKF) seems preferable. In contrast to the EnKF, this filter is formulated in an orthogonal basis, and hence does not suffer from the breakdown of the EnKF analyzed in [85]. It remains to show how to compute the covariances in (46), see also [67, 74, 68, 75, 57, 76, 58, 59]. Given the expansion of the RVs $\boldsymbol{q}_a, \boldsymbol{q}_f$, and $\boldsymbol{y}_f$, this is actually quite simple as any moment can be computed directly from the expansion. Hence, thanks to the orthonormality of the $\{\Psi_b\}$:

$$\boldsymbol{C}_{\boldsymbol{y}_f} = \mathbb{E}\left(\sum_{b>1} \boldsymbol{y}_{f,b}\Psi_b \otimes \sum_{c>1} \boldsymbol{y}_{f,c}\Psi_c\right) = \sum_{b,c>1} \boldsymbol{y}_{f,b} \otimes \boldsymbol{y}_{f,c}\mathbb{E}(\Psi_b\Psi_c) = \sum_{b>1} \boldsymbol{y}_{f,b} \otimes \boldsymbol{y}_{f,b}, \quad \text{and } \boldsymbol{C}_{\boldsymbol{q}_f,\boldsymbol{y}_f} = \sum_{b>1} \boldsymbol{q}_{f,b} \otimes \boldsymbol{y}_{f,b}. \tag{50}$$

It turns out that sometimes it is more advantageous to update the mean free part of the RV $\boldsymbol{q}_f$ in (49) in a slightly different way [69], which was already known from the classical KF for the update of the covariance, and used with various cousins of the KF in order to improve numerical stability (e.g. [96, 89, 19, 73]), namely the so called *square root* filter which uses the eigen-decomposition [70] of the positive semi-definite covariance $\boldsymbol{C}_{\boldsymbol{y}_f} = \boldsymbol{B}\boldsymbol{\Lambda}\boldsymbol{B}^\mathsf{T}$. Following the derivation in [69], and collecting the PCE coefficients with index $b > 1$ associated to mean zero Ψ_b's in $\boldsymbol{Y}_f := [\boldsymbol{y}_{f,2}, \ldots, \boldsymbol{y}_{f,b}, \ldots, \boldsymbol{y}_{f,B}]$, and similarly $\boldsymbol{Q}_f := [\boldsymbol{q}_{f,2}, \ldots, \boldsymbol{q}_{f,B}]$ and $\boldsymbol{Q}_a := [\boldsymbol{q}_{a,2}, \ldots, \boldsymbol{q}_{a,B}]$, one computes the transformed forecast observation $\boldsymbol{W} := \boldsymbol{\Lambda}^{-1/2}\boldsymbol{B}^\mathsf{T}\boldsymbol{Y}_f$ and its singular value decomposition [70] $\boldsymbol{W} = \boldsymbol{U}\boldsymbol{\Sigma}\boldsymbol{V}^\mathsf{T}$, which is used to update the mean free part of the forecast $\boldsymbol{Q}_f$, substituting (49):

$$\boldsymbol{Q}_a = \boldsymbol{Q}_f\boldsymbol{V}(\boldsymbol{I} - \boldsymbol{\Sigma}^\mathsf{T}\boldsymbol{\Sigma})^{1/2}\boldsymbol{V}^\mathsf{T}. \tag{51}$$

Observe that $\boldsymbol{\Lambda}$ and $\boldsymbol{\Sigma}^\mathsf{T}\boldsymbol{\Sigma}$ are diagonal matrices, and so is $(\boldsymbol{I} - \boldsymbol{\Sigma}^\mathsf{T}\boldsymbol{\Sigma})$, thus computing the square roots and inverses in $\boldsymbol{\Lambda}^{-1/2}$ and $(\boldsymbol{I} - \boldsymbol{\Sigma}^\mathsf{T}\boldsymbol{\Sigma})^{1/2}$ is inexpensive. In case that the positive semi-definite $\boldsymbol{\Lambda}$ contains vanishing or nearly vanishing

eigenvalues, the Moore-Penrose pseudo-inverse has to be used to compute $\mathbf{\Lambda}^{-1/2}$, which is also inexpensive for a diagonal matrix. This version of the PCKF is called [69] the *Square Root Polynomial Chaos based Linear Bayesian Update* or the square root PCKF (SQRT), and is the one actually used later in the computations.

The final important topic which still needs to be addressed is that one has to *distinguish at least two cases how the computational upscaling may occur*. They may be best differentiated by looking at the meso- (33) and macro-scale (35) evolution and equations and their corresponding observation models, (34) for the meso-scale and (36) for the macro-scale. The parameters to be identified are $q(\omega, \vartheta, \epsilon)$, where $\epsilon(\vartheta)$ represents all the errors in model, computation and approximation, and observation — although the latter may be argued to be very small in the usual computational environment. So what happens is that one tries to find the map / random variable (RV)

$$\Omega \times \Theta \ni (\omega, \vartheta) \mapsto (\omega, \vartheta, \epsilon(\vartheta)) \mapsto q(\omega, \vartheta, \epsilon(\vartheta)) \in \mathcal{Q}, \tag{52}$$

which will transform the measure on $\Omega \times \Theta$ into the distribution measure of q, the posterior measure from Bayes's theorem. The variable $\vartheta \in \Theta$ (and $\epsilon(\vartheta)$), which jointly represent the epistemic uncertainty and error terms, will always be present in any kind of upscaling. The dependence on the variable $\omega \in \Omega$ on the other hand, which represents the aleatoric uncertainty about the meso-scale as detailed in Subsection 2.2, which are the realizations of the random fields describing it, can be used in two distinct modes. One mode of upscaling may be seen to be one where one fixes the meso-scale, i.e. chooses a fixed $\varpi \in \Omega$ and performs the upscaling to the macro-scale for this *fixed and unique realization of the meso-scale ike in [26, 27, 81, 82, 83]*. This means that we are identifying macro-scale parameters for one particular realization of the meso-scale. Mathematically, in this case one only looks in (52) at the partial map

$$\Theta \ni \vartheta \mapsto (\vartheta, \epsilon(\vartheta)) \mapsto q(\varpi, \vartheta, \epsilon(\vartheta)) \in \mathcal{Q},$$

and the variable ϖ plays no rôle. It is this last situation which leads to algorithms to determine the coefficients in the expansion (47) for the discretized parameters $\boldsymbol{q}_a$, and to which the discretization and algorithms as described above can directly be applied, where a RV $q \in \mathcal{Q} = \mathcal{Q} \times \mathcal{S} \cong L_2(\Theta; \mathcal{Q})$ is identified, and where the only uncertainty is the epistemic one residing in the space of scalar RVs $\mathcal{S} = L_2(\Theta)$.

If, on the other hand, one wants to perform the upscaling for the *whole ensemble* of meso-scale structures described by the probability measure on Ω in Subsection 2.2, one has to look at the whole map in (52). Let us for a moment consider not only computational upscaling, but also identification tasks when the observations $\hat{\boldsymbol{y}}$ are *real* experiments. This situation is present in some form or other in many real world identification problems, and has been analyzed e.g. in [64] in a hierarchical Bayesian (hyper)-parametric framework, and in a different non-parametric fashion in the frame of chaos expansions in [11, 91, 2, 92, 71]. In the context of multi-scale analysis this has been addressed in [77, 84]. The difference to computational upscaling is that in real-experiment-type situation one does not know what realization $\varpi \in \Omega$ 'nature' has presented us with, whereas in a computational environment this is all controlled. Mathematically, the situation may be described by saying that the space $\mathcal{Q}$ is really a space of random variables living on Ω, i.e. $\mathcal{Q} = \mathcal{Q}' \otimes \mathcal{T}$, where $\mathcal{T} = L_2(\Omega)$ is a space of scalar RVs on Ω, and $\mathcal{Q}'$ is now *really* a space of deterministic variables. Thus the final map we are looking for is in $\mathcal{Q} = \mathcal{Q} \otimes \mathcal{S} = \mathcal{Q}' \otimes \mathcal{T} \otimes \mathcal{S} \cong L_2(\Omega \times \Theta; \mathcal{Q}') \cong L_2(\Omega; \mathcal{Q}' \otimes \mathcal{S})$. If one takes the last of these congruences, this may be interpreted as saying that in (47), when the parameters are a function of $(\omega, \theta) \mapsto q(\omega, \theta)$, or rather $(\omega, \theta) \mapsto \boldsymbol{q}_f(\omega, \theta)$ — and similarly for $\boldsymbol{q}_a$ and $\boldsymbol{y}_f$, the coefficients $\{\boldsymbol{q}_{f,b}\}_{b=1}^B$ are not deterministic, but rather random variables $\boldsymbol{q}_{f,b}(\omega)$ on Ω themselves:

$$\Omega \ni \omega \mapsto \boldsymbol{q}_f(\omega, \theta) = \sum_{b=1}^{B} \boldsymbol{q}_{f,b}(\omega) \Psi_b(\theta) \in \mathcal{Q}' \otimes \mathcal{S}. \tag{53}$$

The updating in (48) and (49) (or (51)) is then one of updating a RV living on Ω, and needs further discretization to be really computable. Here we choose an approach in the spirit of what was used in [1] by combining PCE and Monte Carlo (MC) for the forward problem, and extend this also to the inverse identification problem as it was also proposed on [91, 2]. The random coefficients $\boldsymbol{q}_{f,b}(\omega)$ in (53) could thus be developed in their own PCE expansion as the RFs in Subsection 2.2, $\boldsymbol{q}_{f,b}(\omega) = \sum_\alpha \boldsymbol{q}_{f,b}^{(\alpha)} H_\alpha(\boldsymbol{\eta}(\omega))$, and the coefficients $\boldsymbol{q}_{f,b}^{(\alpha)}$ identified as in [91, 2]. A Bayesian approach in this regard was also used in [84]. The approach chosen here is simpler in that regarding the variable $\omega \in \Omega$ which describes the RFs in Subsection 2.2 we choose a pure MC sampling approach, just reverse to what is in [2]. If we take

the view of the quantities $\boldsymbol{q}_f$ and $\boldsymbol{q}_a$ as elements of $L_2(\Omega \times \Theta; Q')$, then our approximation of e.g. $\boldsymbol{q}_f$ is as

$$\boldsymbol{q}_f(\omega_z, \theta) = \sum_{b=1}^{B} \boldsymbol{q}_{f,b}(\omega_z)\Psi_b(\theta) \quad \text{for samples } \omega_z \in \Omega,\ z = 1, \ldots, Z, \tag{54}$$

i.e. a PCE in $\theta \in \Theta$ and MC sampling in $\omega \in \Omega$. In case one wants to compute a pdf for such a RV as in (54), one has to proceed as before in Subsection 4.2: one computes a pdf $\pi_{(Q|Y)}(q|\hat{\boldsymbol{y}}[\omega_z])$ representing the epistemic uncertainty for each sample $\boldsymbol{q}_f(\omega_z, \cdot)$, and the final pdf representing *both the epistemic and aleatoric* uncertainty is the obtained from (39).

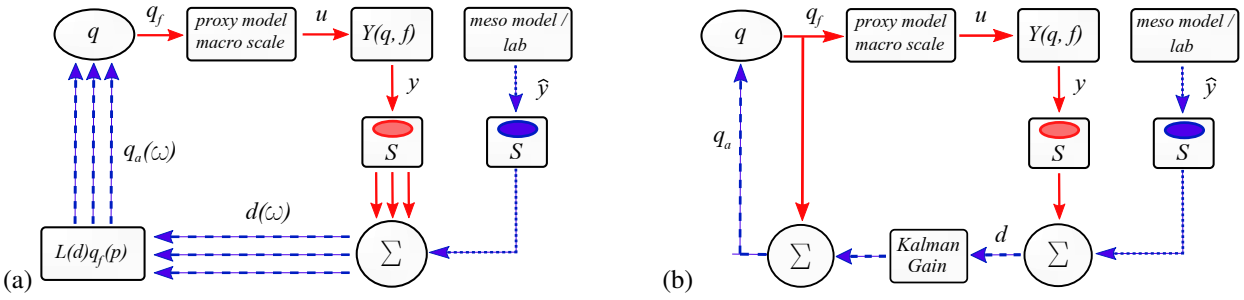

Figure 7: The algorithmic scheme of an inverse problem solved by (a) proxy MCMC filtering; (b) Polynomial Chaos Kalman Filter (PCKF)

Now all the terms needed for the update (45) have been explicitly stated and are readily computable. The discrete approximation in probability space, or proxy model, is further used to enhance the computational efficiency for both the Markov chain Monte Carlo (MCMC) method and the Polynomial Chaos based Kalman filter (PCKF). A simplified representation and flow-chart for the two proposed methods (PCKF and MCMC) for each set of parameters to be identified separately by taking into account different tests and measurements are shown in Figure 7. In the case of the MCMC method, the posterior is described by changing the distribution of the underlying RVs, while in case of PCKF the posterior is obtained by changing the RV. While the MCMC algorithm (Figure 7a) can be quite simple to use as model independent method, its main drawback is its slow convergence or an increased cost to compute the system response for each new sample. Here, we speed up the assimilation process by introducing a proxy model on the macro-scale for the forecast measurements, with the computation starting with samples that are used as input in the deterministic proxy model on the macro-scale. As already indicated, the issue of high computational cost in MCMC can be improved by using Bayesian linear methods, such as the polynomial chaos based [75] PCKF. The algorithm which is used in this work is presented in Figure 7b, and the whole update process can be represented by only one loop. This all has then to be put into an outer loop over the different realizations of the aleatoric variable $\omega_z \in \Omega$, $z = 1, \ldots, Z$ as described previously.

5. Numerical examples of parameter identification

An important point for discussion is related to the proper choice of measurements $Y_m(\cdot)$ (or cost function), which are made in agreement with the corresponding parameters that are identifed. Such a choice is made in order to favor the role of certain parameters of interest and ensure well-posedness of the corresponding identification procedure. All measurements are obtained by numerical simulations, which results in corresponding macro-scale model parameters. Based upon our previous practical experience on failure model parameter identification in a deterministic setting (e.g. see [43]), we first propose to split the identification into elastic, hardening, and softening parameters in order to reduce the computational cost. The simultaneous parameter identification is then given in order to validate our approach and further illustrate eventual cross-correlations among the model parameters.

5.1. Identification of elastic parameters

Given that concrete is a statistically isotropic material (see [41]), the elastic response of a specimen defining the linear part of the global response on a stress-strain diagram is well described by only two parameters, the bulk modulus

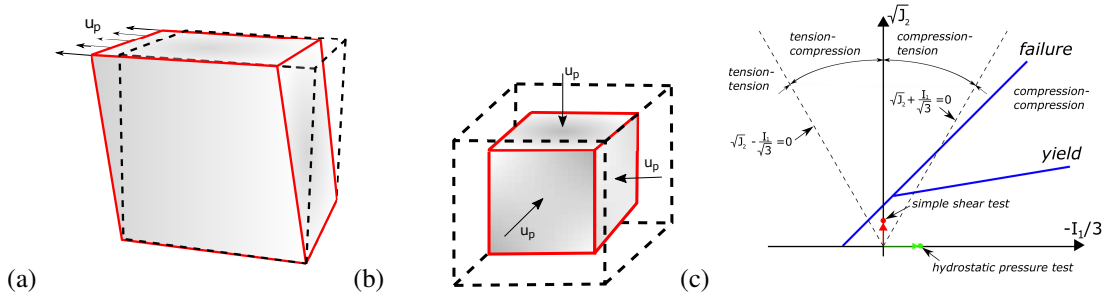

Figure 8: Numerical tests : (a) simple shear test; (b) hydrostatic pressure test; (c) loading path

K and the shear modulus G. In order to identify the shear modulus, which controls the resistance to the change of shape, one can use a simple shear test (Figure 8a). For the identification of the bulk modulus, which controls the material resistance to volume change, one may preferably use hydrostatic compression test (Figure 8b).

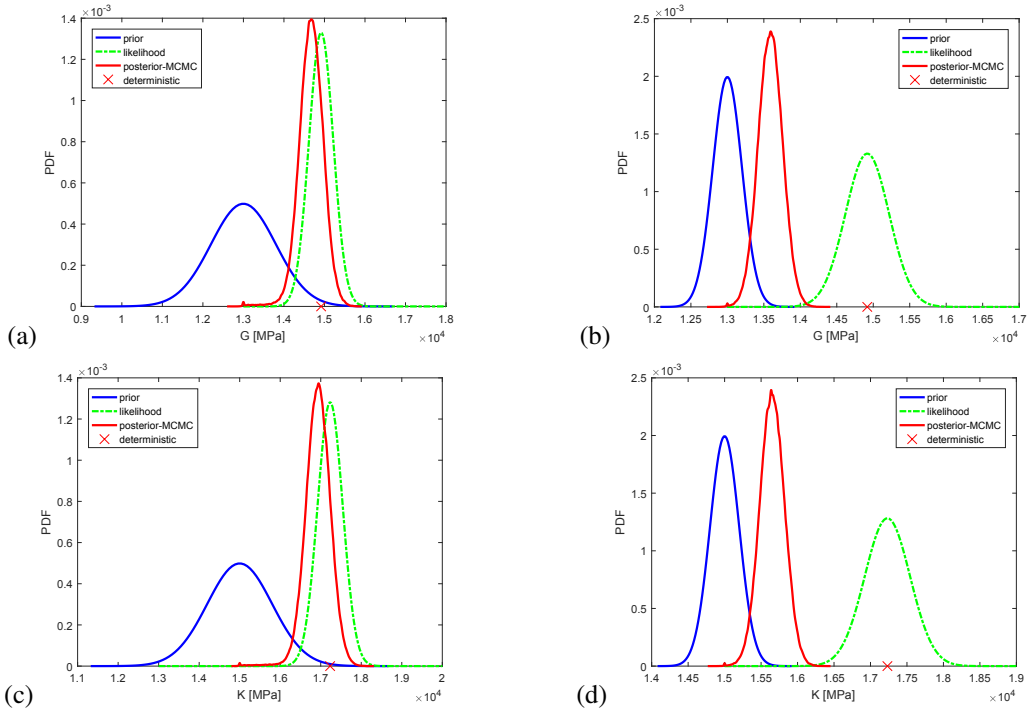

Figure 9: Comparison of prior and posterior pdf and the likelihood function for the shear modulus G — simple shear test (upper row), and bulk modulus K — hydrostatic compression test (lower row) obtained with different choices for the prior standard deviation σ_p = 500 MPa (left) and σ_p = 200 MPa (right) — energy measurements

Our prior for both elastic parameters, on which the posterior distribution will depend, can be based on standard values for concrete of Young's modulus E = 30 GPa, and of Poisson's ratio ν = 0.16. In Figure 9 we display the shape of the prior, the likelihood function, and the posterior probability density function (pdf) obtained by the MCMC method. The value obtained by deterministic identification in [43] by minimizing mean square error for the shear modulus is G = 14.918 GPa, and for the bulk modulus K = 17.232 GPa. These are obtained from simple shear and hydrostatic compression tests, respectively. One may see that the mean and mode of the posterior have moved in the direction of the deterministic value, when compared to the prior (Figure 9a and Figure 9c). In Figure 9b and Figure 9d, the posterior moved to the prior due to a smaller standard deviation of the prior compared to the likelihood, which can be observed in the case when our prior knowledge is more relevant than measurements.

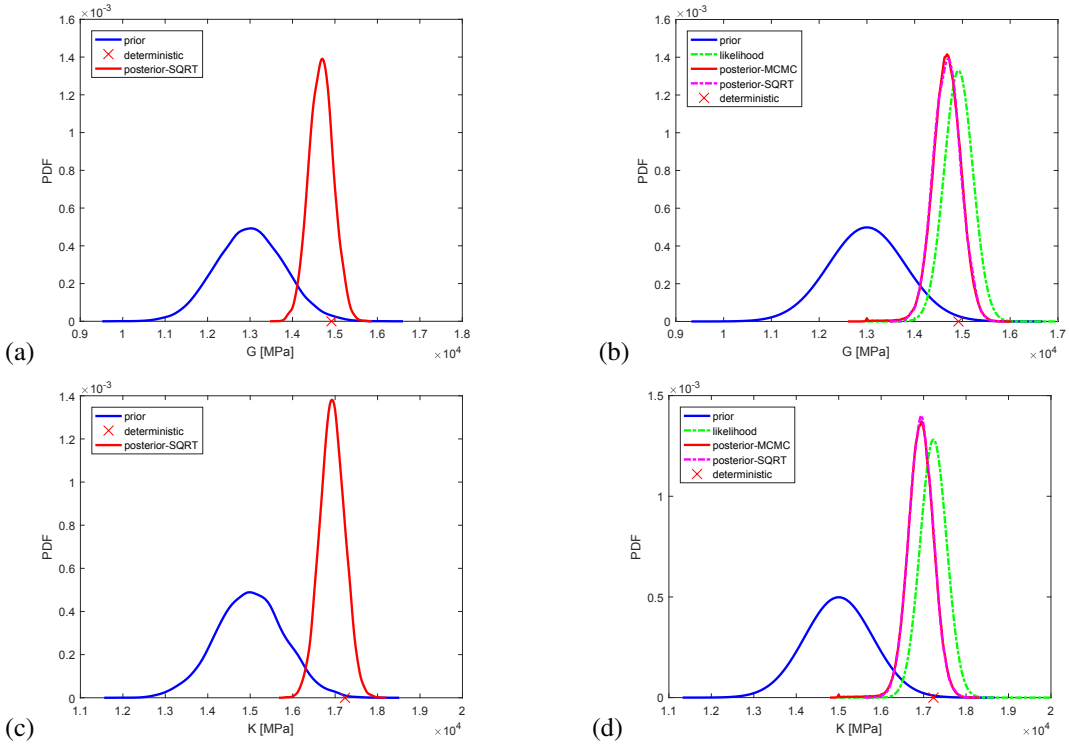

Figure 10: Prior and posterior pdf for the shear modulus G — simple shear test, and the bulk modulus K — hydrostatic compression test, obtained by the SQRT Kalman filter (left — force measurements) and comparison with MCMC (right — energy measurements)

The dependence on the choice of measurements is presented in Figure 10, where one may observe that either measuring the force (suitable for a real experiment), or measuring the elastic energy (suitable for numerical tests), the resulting posterior distribution remains here the same, regardless of the chosen method, MCMC or PCKF.

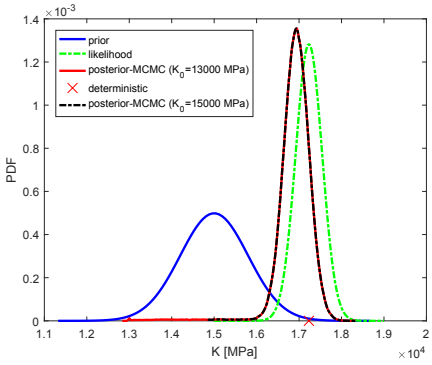

Figure 11: Comparison of prior and posterior pdf and the likelihood function for bulk modulus-hydrostatic compression test for different initial points of the MCMC algorithm

The samples used for computation in the MCMC method are drawn from a proposal distribution with some probability r, thus forming the corresponding sampling sequence. As presented in Figure 11, this sequence converges in distribution to our target posterior distribution, regardless of the starting point. Updates with 10^6 samples are used in the MCMC procedure in order to estimate the value of the particular parameter for given observations, either measuring elastic energy or force (see Table 1). The update process is performed only once using the complete measurement

data with a proposal distribution defined as Gaussian with a standard deviation of $\sigma_{proposal} = 0.001\sigma_{prior}$.

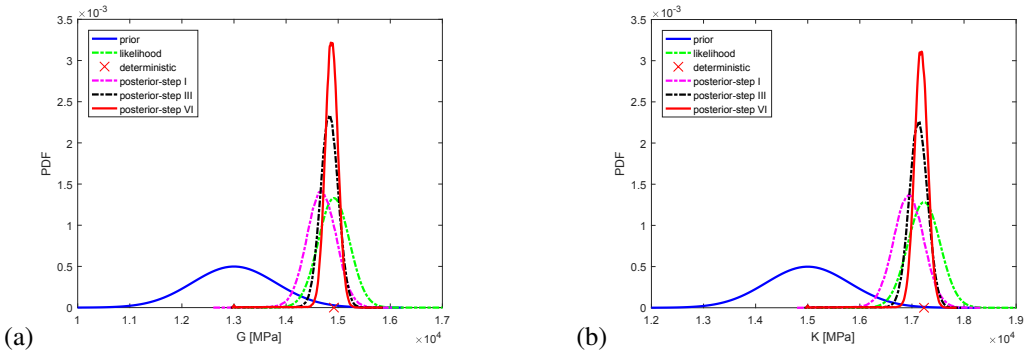

Figure 12: MCMC update of elastic material parameters $\{K, G\}$ using an elastic load step: (a) simple shear test; (b) hydrostatic compression test

In Figure 12 it is shown that each new information from an experiment is updating our knowledge about the bulk modulus K, resulting in a sharper posterior distribution (i.e. the standard deviation is decreasing). The posterior distribution after the first update is used as prior for the next one. The measurements used in updating are taken from three elastic loading steps in the case of a simple shear test and a hydrostatic compression test. Moreover, one finds that the same updates and posterior distribution are obtained with PCKF method (see Figure 13 and Table 1), which allows to validate both methods for the simplest case of elastic parameter identification.

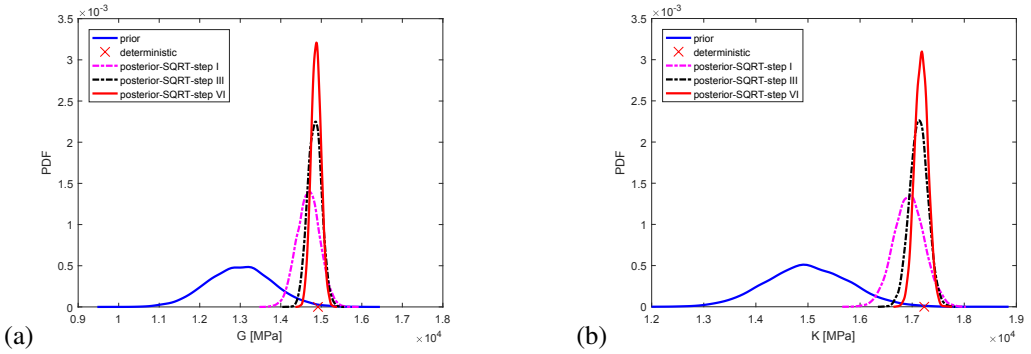

Figure 13: The square root update of elastic material parameters $\{K, G\}$ using an elastic load step: (a) simple shear test; (b) hydrostatic compression test

Another interesting illustration is presented in Figure 14, with an inadequate choice of the test used for a particular parameter identification. In particular, one may note in Figure 14 that the information obtained in a simple shear test does not change the bulk modulus posterior distribution, which remains the same as the prior. The same conclusion holds for deterministic identification, which reveals — as expected — that a simple shear test is not relevant for the identification of the bulk modulus. A similar conclusion can be drawn for the shear modulus that cannot be identified — as may be expected — from a hydrostatic compression test. But in contrast to a deterministic error minimization, which may either not converge or stop at some algorithm dependent point thinking it has found a minimum, in the Bayesian update one sees through the fact that the posterior is equal to the prior that the measurement contained no useful information for the update.

The previous results are also supported by the plots of posterior 95% confidence intervals shown in Figure 15. With every new successive measurement, the probability region narrows down such that the interval becomes practically deterministic after only a few performed measurements, with a very narrow posterior 95% confidence interval.

Figure 16 shows the macroscopic response in the elastic stage for a specimen under uniaxial compression with the mean values of the identified parameters. One may note that the difference between computed response and

RV	prior log-normal		QoI	Gaussian likelihood		1st upd.		posterior 3rd upd.		6th upd.	
	$\bar{X}$ [GPa]	σ_p [GPa]		σ_ψ [J/m^3]	σ_F [kN]	$\bar{X}$ [GPa]	σ_p [GPa]	$\bar{X}$ [GPa]	σ_p [GPa]	$\bar{X}$ [GPa]	σ_p [GPa]
MCMC (n=10^6 samples)											
G	13.0	0.8	ψ or	6.67E-02	4.5E-02	14.68	0.28	14.84	0.16	14.86	0.12
K	15.0	0.8	F	1.29E-12	3.5E-06	16.95	0.28	17.14	0.17	17.19	0.12
PCEKF (p=3 polynomial order)											
G	13.0	0.8	ψ or	6.67E-02	4.5E-02	14.68	0.28	14.83	0.16	14.87	0.12
K	15.0	0.8	F	1.29E-12	3.5E-06	16.94	0.28	17.13	0.17	17.18	0.12

Table 1: Prior and likelihood distribution input data and obtained posterior distribution data for the shear modulus G — simple shear test, and for the bulk modulus K — hydrostatic compression test; $\bar{X}$ is the mean value and σ_p the standard deviation for the particular distribution (log-normal prior, Gaussian likelihood, and posterior).

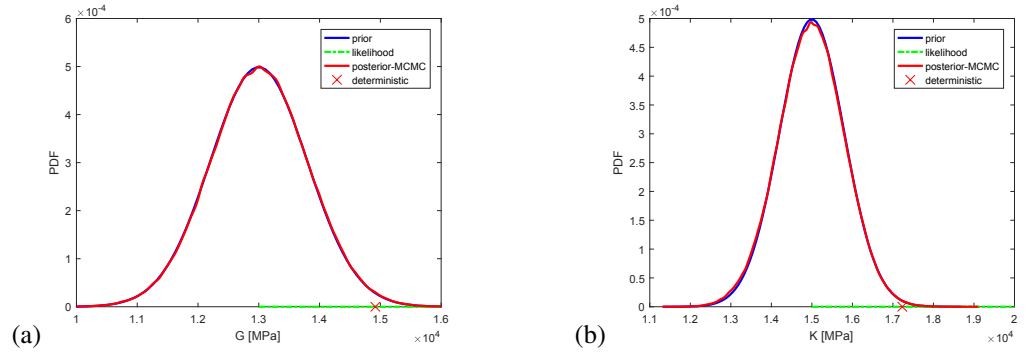

Figure 14: Comparison of prior and posterior pdf and the likelihood function for the shear modulus G — hydrostatic compression test, and for the bulk modulus K — simple shear test

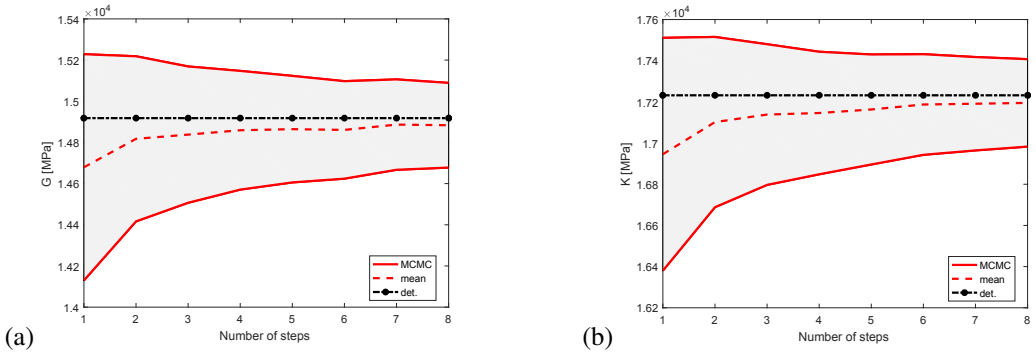

Figure 15: Comparison of posterior pdf for different measurement points describing elastic material parameters: (a) shear modulus G — simple shear test; (b) bulk modulus K — hydrostatic compression test

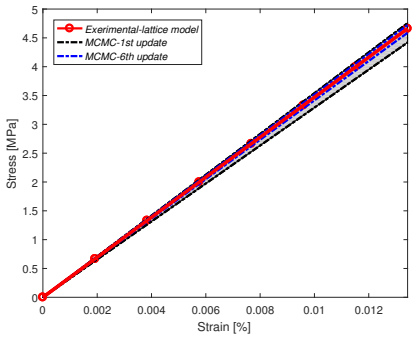

Figure 16: Macroscopic response in the elastic range with computed parameters

measurements is small enough even when only one measurement is taken into account. This difference is even smaller if we perform identification with several measurements in the elastic stage.

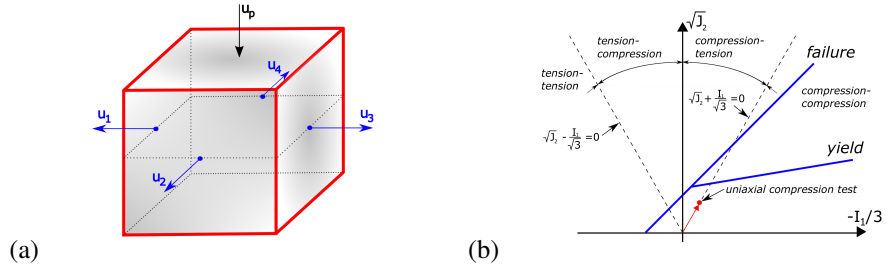

Figure 17: (a) Displacements measured to evaluate the expansion $\Delta l = 0.25 \cdot (u_1 + u_2 + u_3 + u_4)$ of the specimen; (b) loading path

Although this kind of calibration procedure is robust and accurate in the proposed procedure for model reduction, the experiments dealing with a simple shear test, and especially the hydrostatic pressure test, are rather difficult to generalize to an experimental setting. For that reason, we study the possibility of parameter pfd estimates by using measurements that would correspond to standard experiments, such as uniaxial compression test (see Figure 17b). The distribution of elastic parameters (K,G) can still be recovered by using the measurements obtained from the uniaxial compression test, but the identification is well conditioned only if the cost function with measurements of force or energy is expanded to include the measurements of the specimen expansion (Figure 17a). The choice of such an elaborate QoI clearly leads to non-Gaussian distribution of the parameter variation; see Figure 18a-b. Figure 18c-d and Table 2 shows the results obtained for the same QoI by using the SQRT Kalman filter, where the Bayesian updates for the parameter distributions are exploiting the measurements obtained for different meso-structure realizations, revealing that a uniaxial compression test improves our knowledge about the shear modulus better than about the bulk modulus, for each of chosen methods. Moreover, as it is known that all realizations for a large enough RVE will give the same homogenized value as the aleatoric uncertainty will average out, using as prior the posterior distribution of the previous measurement clearly allows to obtain sharper bounds.

These findings are also in agreement with Figure 19, revealing that the two moduli remain correlated. We note that the particular joint pdf shown in Figure 19, and all subsequent ones, are plotted for the final updated step.

The dependence of the PCE on the polynomial order is investigated in Figure 20, where the accuracy of the sum of all reaction force approximations on the uniaxial compression test is plotted for different polynomial orders. By comparing the approximate solution against the reference value obtained by the forward model, one concludes that only the third order PCE approximation is sufficiently accurate to use. In such a case only, the response for K and G both match with the one obtained by forward model response. For the lower order PCE polynomial approximations, the mean value is still estimated correctly (with the cross point), but that is no longer true for the higher order moments (since the lines do not match); see Figure 20.

In conclusion, the concrete can be considered as a statistically isotropic material, since the response for loading in

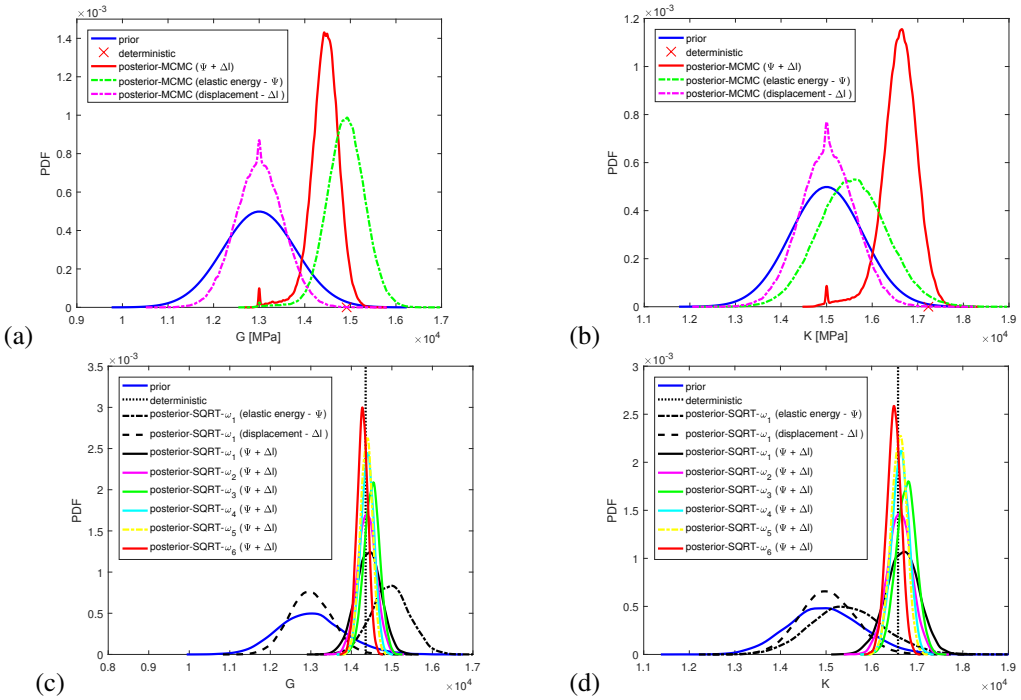

Figure 18: Comparison of prior and posterior pdf functions for: (a) shear modulus; (b) bulk modulus performed on uniaxial compression test obtained by MCMC (upper row) and by SQRT Kalman filter (lower row)

RV	QoI	Gaussian likelihood			posterior (PCEKF)						average (epist.+alea.) [GPa]
		σ_ψ [J/m^3]	$\sigma_{\Delta u}$ [mm]		ω_1	ω_2	ω_3	ω_4	ω_5	ω_6	
G	ψ Δu	3.87	5.0E-08	$\bar{X}$:	14.42	14.38	14.50	14.40	14.37	14.27	14.35
				σ_p:	0.31	0.23	0.19	0.16	0.14	0.13	
K	ψ or Δu			$\bar{X}$:	16.80	16.62	16.76	16.63	16.60	16.49	16.58
				σ_p:	0.36	0.26	0.22	0.19	0.17	0.15	

Table 2: Likelihood input data and obtained posterior distribution data for 6 realizations ω_j, $j = 1, \ldots, 6$, for the shear modulus G and for the bulk modulus K — uniaxial compression test. $\bar{X}$ is the mean and σ_p the standard deviation in [GPa]. Prior distribution data are given in Table 1.

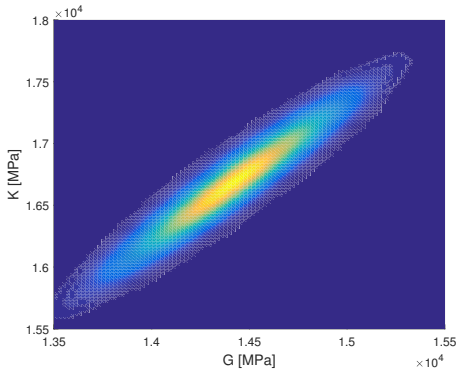

Figure 19: Joint pdf of bulk K and shear modulus G for the uniaxial compression test

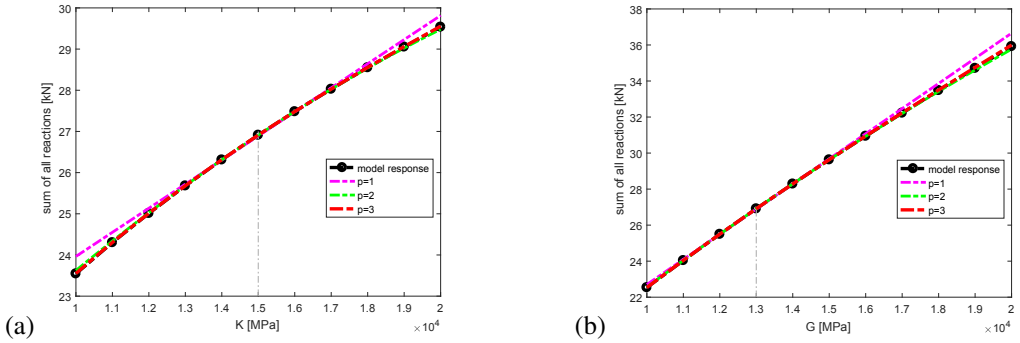

Figure 20: Polynomial chaos approximation of the model response for the uniaxial compression test: (a) bulk modulus K; (b) shear modulus G

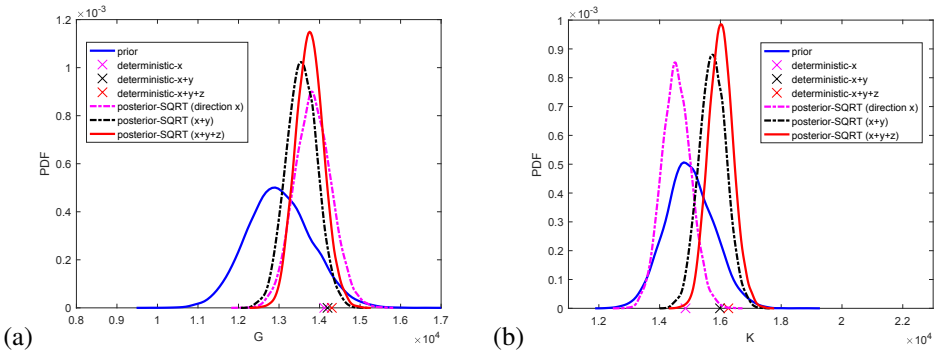

Figure 21: Comparison of prior and posterior pdf functions obtained by SQRT Kalman filter for: (a) shear modulus G; (b) bulk modulus K performed on uniaxial tension tests for three loading directions

RV	QoI	Gaussian likelihood		posterior (PCEKF) direction x			direction x+y			direction x+y+z		
		σ_ψ [J/m^3]	$\sigma_{\Delta u}$ [mm]	$\bar{X}$ [GPa]	σ_p [GPa]	det. [GPa]	$\bar{X}$ [GPa]	σ_p [GPa]	det. [GPa]	$\bar{X}$ [GPa]	σ_p [GPa]	det. [GPa]
G	ψ	3.87E-02	5.0E-08	13.83	0.46	14.12	13.56	0.38	14.20	13.75	0.34	14.30
K	Δu			14.55	0.48	14.85	15.75	0.44	15.99	16.01	0.40	16.26

Table 3: Likelihood input data and obtained posterior distribution data for the shear modulus G and for the bulk modulus K — uniaxial tension test. Prior distribution data are given in Table 1.

any of three directions differs only a little. Here, we provide the identification of both elastic parameters in a sequential manner by using one measurement from a uniaxial tension test with loading in three directions. We note in Figure 21 that the updating is similar to the one performed on one test with multiple measurements, given that the response in the three directions is almost the same. All these measurements are taken from uniaxial tension tests obtained by the meso-scale model with a 50% volume fraction of aggregates. Here, we use the modulus obtained by a deterministic identification for the x direction as part of the prior for the first update, and subsequently we use the mean value of these moduli in the x, y and z directions for a second and third update (see Table 3).

5.2. *Identification of hardening parameters*

Once we have identified the elastic parameters from the appropriate tests, we can continue towards the estimate of the hardening parameters. Namely, the parameters that we are trying to recover are now $q = (\sigma_y, \beta, \tan(\phi), \tan(\psi), \sigma_{\text{inf}})$, denoting the yield stress, the hardening parameter, the angle of internal friction, the angle of internal dilatancy, and the ultimate limit stress for saturation type of hardening, respectively. Note that hardening in the macro-scale model follows after an elastic response in the compression test, whereas in the tension test the elastic response is directly followed by the softening part. The stress in hardening increases until it reaches σ_∞, which can be directly computed as $\sigma_\infty = \sigma_{max,ref} + \sigma_y$, where $\sigma_{max,ref}$ is the limit stress from a stress-strain diagram obtained with numerical or experimental tests. With a such simplification there are four material parameters to be identified. Performing deterministic identification, we note that when identifying these four parameters simultaneously, the cost function remains quite demanding to optimize. When defining the yield function and of the plastic potential function, these four parameters can further be split into two groups. First, the yield stress and the angle of internal friction $(\sigma_y, \tan(\phi))$, which are sufficient to define the yield function, and then the hardening parameter and the angle of internal dilatancy $(\beta, \tan(\psi))$, which are sufficient to define the plastic potential function. In addition to this simplification, and to keep this optimization step efficient, the simulations are restricted to a limited loading range.

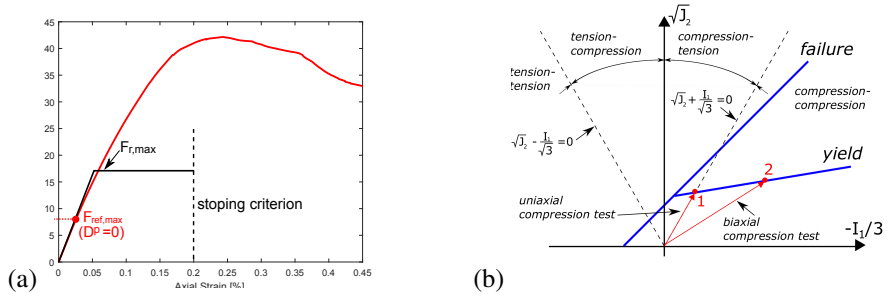

Figure 22: (a) force measured on the meso-scale model (red) and the 3D solid model (black) with a simplified model for the identification of the yield function; (b) loading path

Thus, for the purpose of the identification of σ_y and $\tan(\phi)$, the first step can be performed by setting the macro-scale model to the ideally-plastic model (Figure 22a). The measurements of free potential energy ψ and dissipation D^p are taken here from uniaxial and biaxial compression tests performed on a plate specimen with dimension 150 x 30 x 150 cm (Figure 22b).

Figure 23 and Table 4 shows that we update our knowledge only if measurements from both biaxial and uniaxial test are taken into account, proving that the yield function can be recovered with a minimum two measurements (red points in Figure 22b). If only measurements from uniaxial or biaxial compression tests are included into the identification procedure, it results in a wide range of parameters that can match the measurements, which is again in agreement with the deterministic identification (Figure 24).

The accuracy of the proxy model for different polynomial orders obtained on the combined uniaxial and biaxial compression tests is presented in Figure 25. Here, the elastic energy given by (20) represents the sum of elastic energies for both tests at the end of computation. One may note that the response in both directions (direction of σ_y and $\tan(\phi)$) match with the forward model only for the third polynomial order, which is the same polynomial order that is needed for the proxy model solution in the case of elastic parameters.

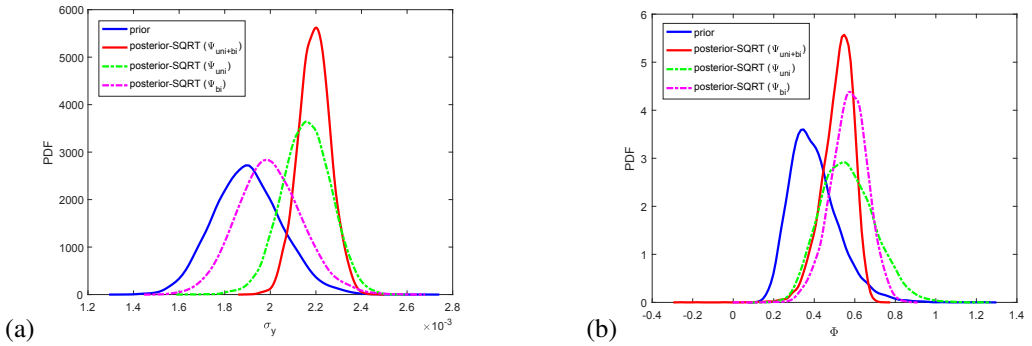

Figure 23: Updates for plastic parameters $\{\sigma_y, \tan(\phi)\}$ obtained with a SQRT Kalman filter

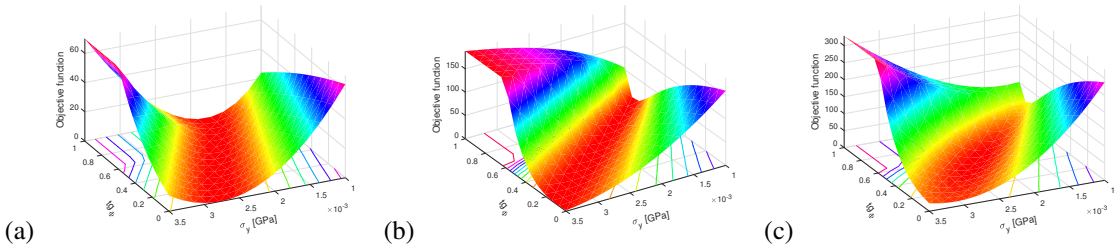

Figure 24: Objective function with measurements taken from: (a) uniaxial test; (b) biaxial test; (c) uniaxial and biaxial test combined

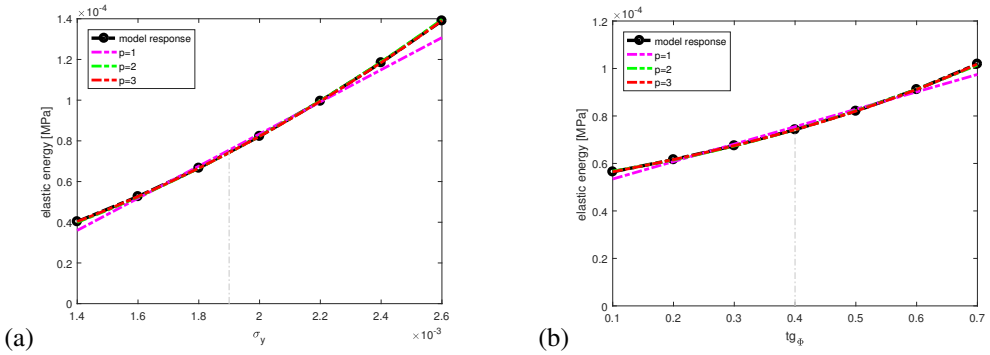

Figure 25: Polynomial chaos approximation of the model response for combined uniaxial and biaxial compression test: (a) yield stress — σ_y; (b) angle of internal friction - $\tan(\phi)$

RV	prior log-normal		QoI	Gaussian likelihood		posterior (PCEKF) uniaxial		biaxial		uni+biaxial	
	$\bar{X}$ [GPa]	σ_p [GPa]		σ_ψ [J/m^3]	σ_{D^p} [MPa]	$\bar{X}$ [GPa]	σ_p [GPa]	$\bar{X}$ [GPa]	σ_p [GPa]	$\bar{X}$ [GPa]	σ_p [GPa]
σ_y (E-03)	1.90	0.15	ψ	1.71E-06	1.30E-06	2.15	0.11	1.99	0.14	2.19	0.07
$tan(\phi)$	0.40	0.12	D^p			0.56	0.13	0.57	0.09	0.52	0.08

Table 4: Prior and likelihood distribution input data and obtained posterior distribution data for the yield stress σ_y , and for the angle of internal friction $tan(\phi)$. $\bar{X}$ is the mean value and σ_p the standard deviation for the particular distribution (log-normal prior, Gaussian likelihood, and posterior).

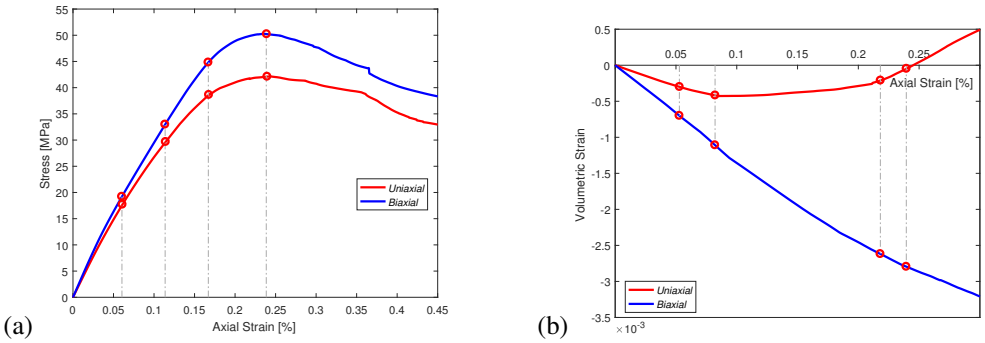

Figure 26: Measurements for the objective function for the hardening parameters $(\beta, \tan(\psi))$ (a) stress-strain curve; (b) volumetric strain—axial strain

The second stage of the identification of the hardening parameters involves the angle of dilatancy $\tan(\psi)$ and the hardening parameter β for a saturation type of hardening. There are two requirements for the choice of measurements in this stage. First, the measurements should be chosen between the yield strain — ϵ_y — and a strain which corresponds to the limit stress. Second, the number of measurements should ensure a convex objective function. If the first requirement is fulfilled, the corresponding objective function depends only on the values of the hardening parameter and the dilatancy angle, because bulk and shear moduli, as well as the yield stress and the angle of internal friction, are kept fixed with the optimal values determined during the previous stage. To identify these two parameters we propose to include four measurements not only of force or dissipation, but also of volumetric strain (Figure 26).

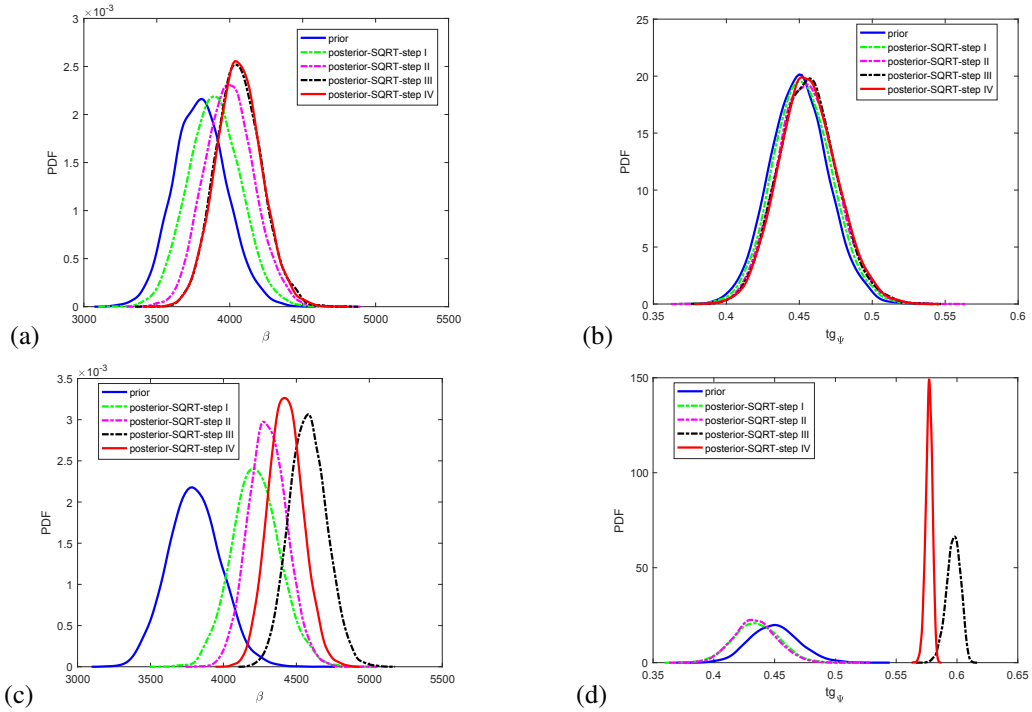

Figure 27: Updates for plastic parameters $\{\beta, \tan(\psi)\}$ obtained with a SQRT Kalman filter with four measurements (plastic dissipation — D^p) shown in (a)–(b) and (plastic dissipation — D^p + volumetric strain) shown in (c)–(d), taken from uniaxial compression tests

The choice of the QoI for different measurements is explored in Figure 27. From Figure 27 one may note that measuring only the plastic dissipation is not sufficient in order to recover an updated distribution for both parameters.

Namely, our prior knowledge about the angle of internal dilatancy remains unchanged due to a lack of information. If we include in the updating process information about the volumetric strain, then the updated distribution is moving towards the deterministic value for each new measurement for the hardening parameter β, while for the angle of internal dilatancy $\tan(\psi)$ only the third and fourth measurements provide adequate information (see Table 5).

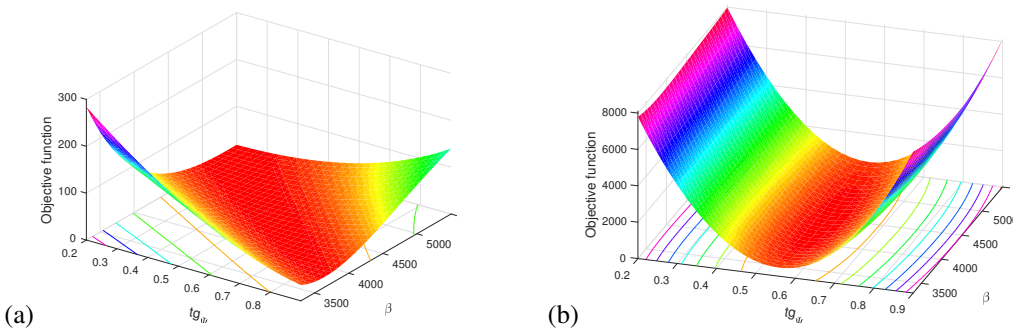

Figure 28: Objective function J_9 with measurements taken from uniaxial compression test (a) plastic dissipation (D^p); (b) plastic dissipation (D^p) + volumetric strain

The cost function used in the deterministic identification is presented in Figure 28. One may note that the optimal parameters are in a wide range in the direction of β, in contrast to the narrow range for the angle of internal dilatancy $\tan(\psi)$. These findings are in agreement with results obtained with the stochastic identification, where the deviation from mean value is much higher for the hardening parameter than for the dilatancy angle.

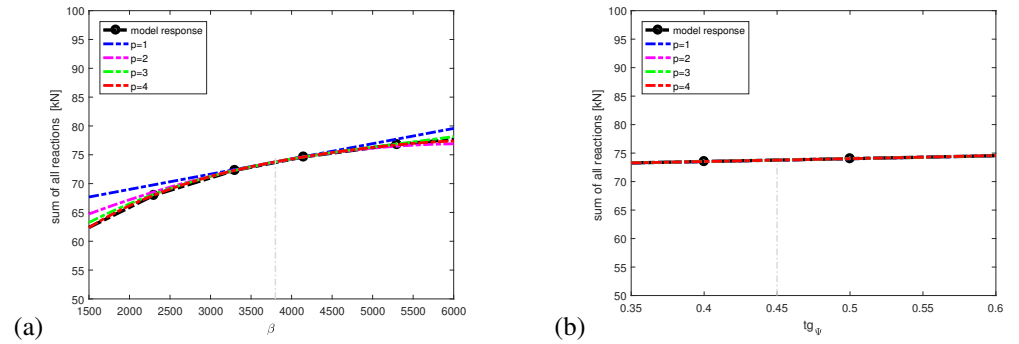

Figure 29: Polynomial chaos approximation of the model response for combined uniaxial and biaxial compression test: (a) hardening parameter — β; (b) angle of internal dilatancy — $\tan(\psi)$

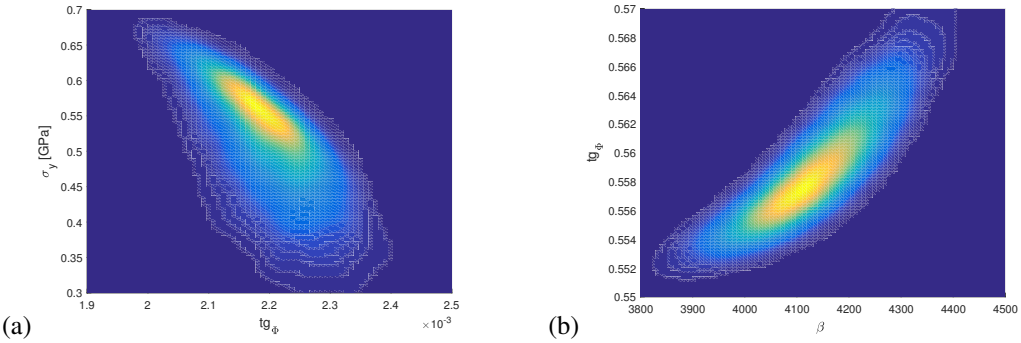

Figure 30: Joint pdf of: (a) yield stress — σ_y and angle of internal friction — $\tan(\phi)$; (b) hardening parameter — β and angle of internal dilatancy — $\tan(\psi)$ for a combined uniaxial and biaxial compression test

In order to safely use the forward model approximation in the case of computing the distributions of the hardening parameters with the QoI chosen as the plastic potential function, we have found the sufficient accuracy with fourth-order PCE polynomial used in the proxy model (Figure 29). From Figure 30 one may note that hardening parameters are also correlated, as much as the elastic parameters.

RV	prior log-normal		QoI	Gaussian likelihood		posterior (PCEKF) 1st upd.		3rd upd.		4th upd.	
	$\bar{X}$ [GPa]	σ_p [GPa]		σ_ψ [J/m^3]	$\sigma_{\Delta u}$ [mm]	$\bar{X}$ [GPa]	σ_p [GPa]	$\bar{X}$ [GPa]	σ_p [GPa]	$\bar{X}$ [GPa]	σ_p [GPa]
β	3800.0	180.0	ψ	6.94E-05	3.00E-06	4241.6	165.6	4587.3	125.3	4437.5	115.2
$tan(\psi)$	0.450	0.020	Δu			0.434	0.018	0.598	0.009	0.576	3.51E-03

Table 5: Prior and likelihood distribution input data and obtained posterior distribution data for the hardening parameter β , and for the angle of dilatancy $tan(\psi)$. $\bar{X}$ is the mean value and σ_p the standard deviation for the particular distribution (log-normal prior, Gaussian likelihood, and posterior).

5.3. Identification of softening parameters

The last stage of the identification involves the limit stress σ_u, the fracture energy in tension $G_{f,t}$, and the fracture energy in compression $G_{f,c}$. The variable σ_u represents a limit of the hardening response phase of the material in compression, and the elasticity limit in tension. Either is followed by the appearance of macroscopic cracks typically placed in the direction of principal elastic strain, but with a different number or different fracture energy release rates for tension versus compression. There are two possibilities to determine the corresponding limit stress. The first is based on a comparison of the displacement corresponding to this event on the meso-scale model or in experimental results with a macro-scale model. The second is based on a comparison of the maximum stress on reference curve with a maximum stress of the macro-scale model. Determination of the displacement at which the limit stress is reached is a rather difficult task, and thus we turn to the second possibility. In order to recover the ultimate stress σ_u leading to softening and fracture energy both in tension $G_{f,t}$ and in compression $G_{f,c}$, we take measurements of the limit stress on the meso-scale model as well as the measurements of the total energy in two steps that belong to the softening response.

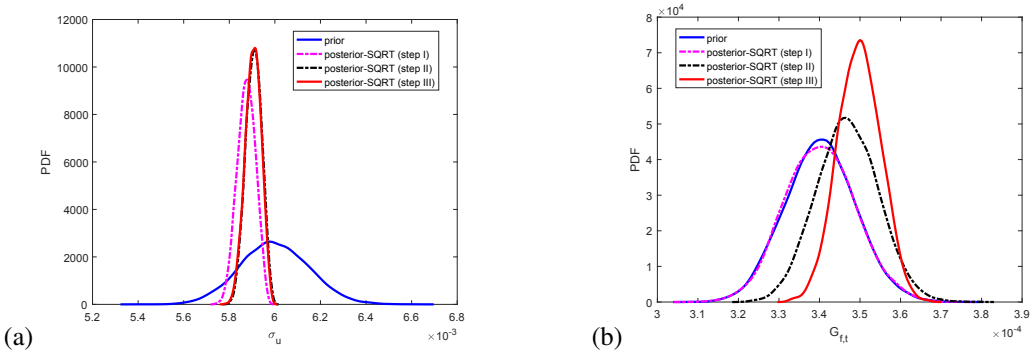

Figure 31: Updates for softening parameters σ_u,and $G_{f,t}$ obtained by SQRT Kalman filter with three measurements taken from uniaxial tension test

In Figure 31 and Table 6 we show updated probability distributions for macro-scale model parameters governing the softening response σ_u,and $G_{f,t}$ One may note that the first measurement (step I) does not change the posterior distribution of the fracture energy release rate, simply due to an inadequate choice of the measurement. Namely, the first measurement represents the limit stress on the meso-scale model, and thus the full information about the fracture energy is not yet completed. In the subsequent steps the total energy becomes more relevant for the fracture energy, and it moves the distribution towards the deterministic value. Again, one may find that the distribution of the limit

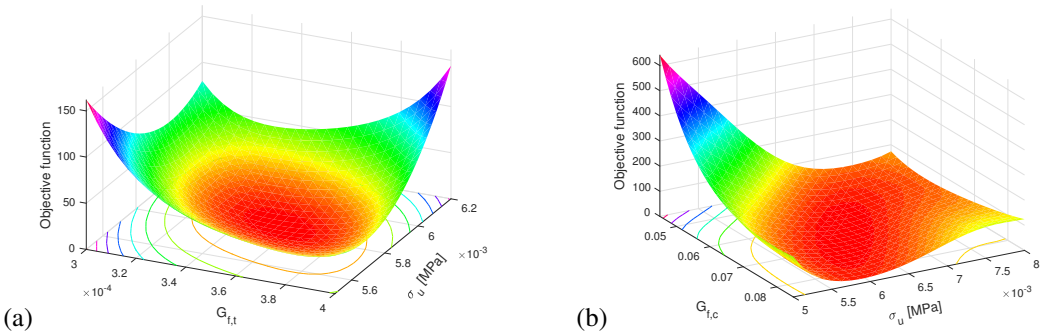

Figure 32: Objective function for: (a) uniaxial tension test; (b) uniaxial compression test

RV	prior log-normal		QoI	Gaussian likelihood		1st upd.		posterior (PCEKF) 2nd upd.		3rd upd.	
	$\bar{X}$ [GPa]	σ_p [GPa]		σ_ψ [J/m^3]	σ_{D^p} [MPa]	$\bar{X}$ [GPa]	σ_p [GPa]	$\bar{X}$ [GPa]	σ_p [GPa]	$\bar{X}$ [GPa]	σ_p [GPa]
σ_u	5.95E-03	1.50E-04	ψ	4.15E-07	5.80E-06	5.88E-03	4.06E-05	5.91E-03	3.69E-05	5.91E-03	3.65E-05
$G_{f,t}$	3.40E-04	8.75E-06	D^p			3.40E-04	8.75E-06	3.45E-04	7.77E-06	3.51E-04	4.87E-06

Table 6: Prior and likelihood distribution input data and obtained posterior distribution data for the ultimate stress σ_y , and for the fracture energy in tension $G_{f,c}$. $\bar{X}$ is the mean value and σ_p the standard deviation for the particular distribution (log-normal prior, Gaussian likelihood, and posterior).

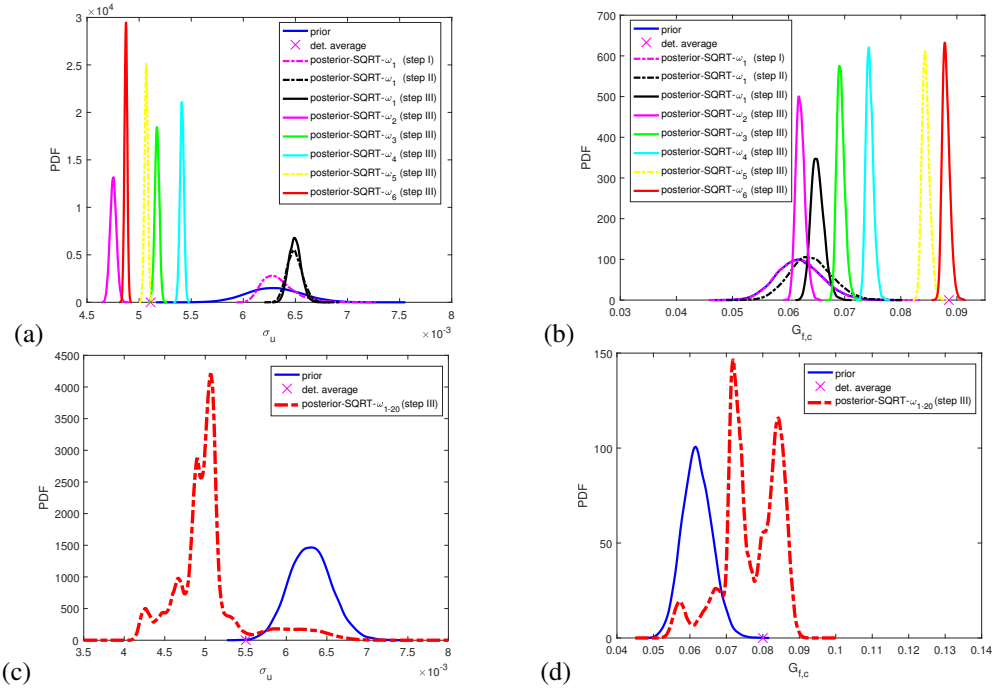

Figure 33: Updates for softening parameters σ_u and $G_{f,c}$ obtained by SQRT Kalman filter with three measurements taken from uniaxial compression test for six different realizations - ω: a-b) with subsequent updating of the prior with previous realization results; c-d) keeping the same prior (blue solid line) for each realization and increasing number of realization.

stress is sharper compared to the distribution of fracture energy, which is in agreement with results obtained with the corresponding results of deterministic identification (Figure 32).

When it comes to the softening parameters, one has to be precise about what one wants to identify. For a statistically homogeneous (and isotropic) medium, as is assumed here for concrete, it is known that for the elastic parameters it is possible to achieve homogenization; the latter implies that doing the identification over larger and larger volumes, the upscaled quantities converge to a deterministic result, i.e. in this case to a real number. The elastic energy of the heterogeneous, but statistically homogeneous, meso-structure will in the limit of an infinite volume covering the whole space be exactly equal to a deterministic homogeneous material with the homogenized coefficients. In the computations one can not simulate an infinite volume, but one may view different realizations of the meso-structure, which, as described in Subsection 4.4 correspond to different values of the random variables ω, as different spatial parts of an infinitely large volume. This means that we assume that the stochastic description of the elastic parameters is *ergodic*. Therefore, when identifying these elastic parameters in Subsection 5.1, which should be identified as fixed numbers with the remaining uncertainty only an epistemic uncertainty described by the random variables θ in Subsection 4.4, one can instead of averaging over the infinite volume do the averaging over different realizations. The same is true in a certain sense when identifying hardening parameters in Subsection 5.2, as hardening behavior will usually lead to a large FPZ rather than localization, and one may again assume ergodicity. In contrast to elasticity, where the macro-model has no model error for homogeneous deformations, one may not expect the sharpening or 'convergence' towards a deterministic value, as the yield stress parameter σ_y describes in a way the transition between reversible and irreversible behavior, and this happens locally. Thus one might expects a residual epistemic uncertainty due to upscaling and model errors. However, when identifying finally the softening parameters, the assumption of ergodicity is not a good one, as the softening behavior goes hand in hand with localization. Thus the goal must be to keep the aleatoric uncertainty of the meso-scale represented in the macro-scale.

The results of different Bayesian updates for the probability distributions of the parameters governing compressive softening obtained from the uniaxial compression test are shown in Figure 33. In particular, Figures 33a-b show the probability distributions for the softening parameters σ_u and $G_{f,c}$ obtained by using the sharper estimates for the prior obtained by the posteriori result from previous realizations. However, this strategy clearly does not meet the same success as the same kind of computations for the elastic parameters, as shown previously in Figures 18. This is not surprising, since the homogenization-type approach (with increasing the number of realizations and relying on ergodicity) no longer guarantees 'convergence' for larger and larger volumes when it comes to the softening regime representing localized failure, which is very sensitive to imperfections. As, due to a lack of ergodic behavior, it makes no sense to average over the random variable ω in Subsection 4.4, what has to be identified for the softening behavior are random variables, i.e. functions of ω, and not a fixed number as in the case of the elastic parameters. In order to identify the softening parameters as random variables, representative only for the chosen averaging volume, we first identified for each Monte Carlo realization ω_j of the meso-structure the posterior distribution (conditioned on that realization) which only represents epistemic uncertainties tied to the θ-variables in Subsection 4.4. As the total behavior may be viewed as a mixture of the different ω-realizations, the unconditioned posterior distribution — which describes both the aleatoric and epistemic uncertainty of the desired random variable — is a convex combination of the conditioned (on $\omega = \omega_i$) posteriors. In a Monte Carlo sample all realizations have the same weight, hence this is just the average of the conditioned posteriors, see (39). Such posterior pdfs for σ_u and $G_{f,c}$ are shown in Figure 33c-d by averaging the pdfs of 20 realizations (this number is chosen only to illustrate our arguments); one may note that both are clearly non-Gaussian. With an increasing number of samples, what is to be expected is *convergence in probability*, i.e. point-wise convergence of the distribution function, the integral of the densities. This kind of results also fits quite well with experimental results for compressive strength of concrete, which usually require several tests to obtain valid statistics-based estimates.

The accuracy of the proxy model solution for different polynomial orders is presented in Figure 34, where one may note that only fourth or higher order polynomials provide a satisfactory solution. These findings of polynomial order used in the proxy model solution for each stage confirm the proposed split in the identification procedure.

In Figure 35 we show the joint pdf for softening parameters for the identification performed on a uniaxial tension test and on a uniaxial compression test. One may find that the limit stress and the fracture energy release rate are much more correlated in the compression test than in the tension test, due to the choice of measurements. Namely, in both cases we use the total energy as a measurement, which for a failure in tension consists only of elastic and fracture energy, whereas in compression there is an additional energy contribution in the fracture process zone.

RV	prior log-normal		QoI	Gaussian likelihood		posterior - ω_1 (PCEKF) 1st upd.		2nd upd.		3rd upd.	
	$\bar{X}$ [GPa]	σ_p [GPa]		σ_ψ [J/m^3]	σ_{D^p} [MPa]	$\bar{X}$ [GPa]	σ_p [GPa]	$\bar{X}$ [GPa]	σ_p [GPa]	$\bar{X}$ [GPa]	σ_p [GPa]
σ_u	6.30E-03	2.60E-04	ψ	1.15E-05	8.70E-06	6.22E-03	1.75E-04	6.49E-03	9.69E-05	6.50E-03	8.07E-05
$G_{f,t}$	6.20E-02	4.00E-03	D^p			6.19E-02	3.99E-03	6.29E-02	3.81E-03	6.45E-02	1.51E-03

Table 7: Prior and likelihood distribution input data and obtained posterior distribution data for the ultimate stress σ_y , and for the fracture energy in compression $G_{f,t}$. $\bar{X}$ is the mean value and σ_p the standard deviation for the particular distribution (log-normal prior, Gaussian likelihood, and posterior).

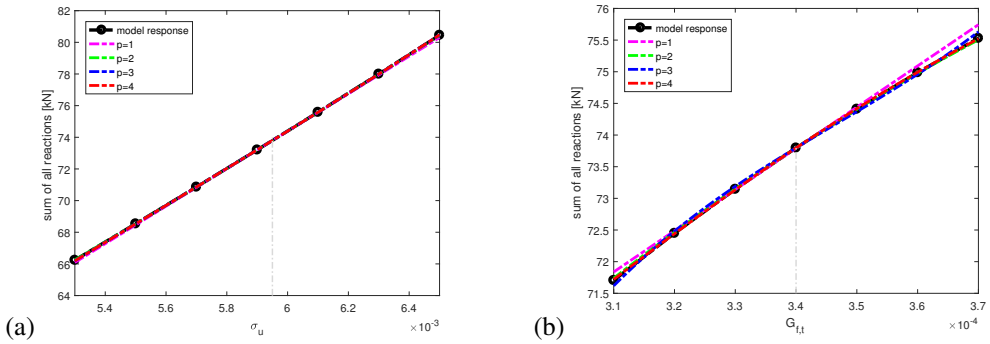

Figure 34: Polynomial chaos approximation of the model response for combined uniaxial tension test: (a) limit stress — σ_u; (b) fracture energy — $G_{f,c}$

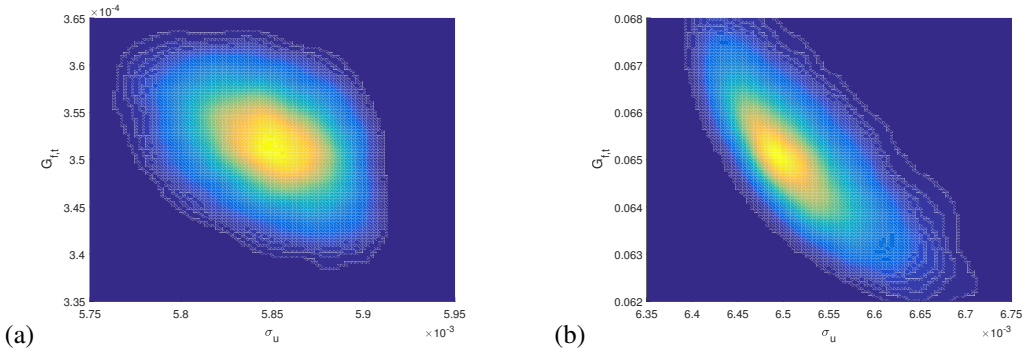

Figure 35: Joint pdf of limit stress — σ_u and fracture energy — $G_{f,t}$: (a) for a uniaxial tension test ; (b) for a uniaxial compression test

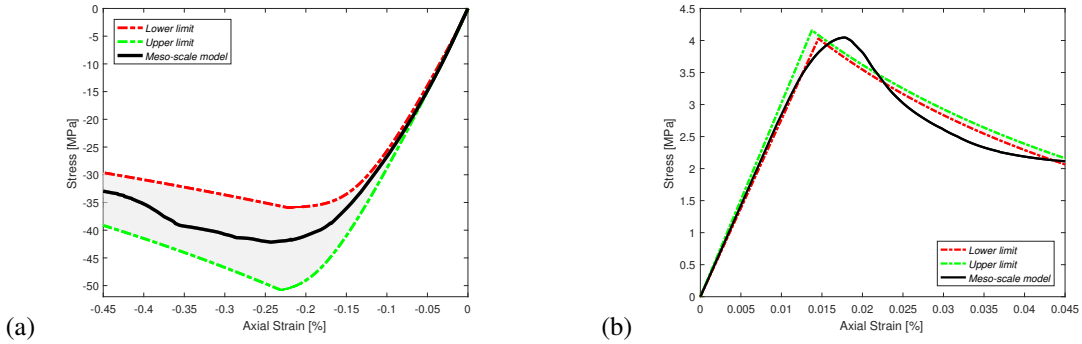

Figure 36: Global response computed with a 95% confidence interval of the posterior distribution for: (a) uniaxial compression test; (b) uniaxial tension test

In Figure 36 is shown the global response with parameters corresponding to a 2.5% fractile value, marked as a lower limit curve, and with parameters which correspond to a 97.5% fractile value of the posterior distribution marked as an upper limit curve. One may note that the elasticity parameters remains almost deterministic, while the limit stress in compression varies much more than the limit stress in tension.

5.4. Simultaneous identification of all macro-scale model parameters and use of standard experiments

In this last example we want to illustrate two important points concerning a possible difficulty in solving such identification problems: first using only standard experimental results, and second an alternative strategy to the one advocated herein that would attempt to identify all model parameters simultaneously. As for the former, we show that the standard uniaxial compression test for concrete is often insufficient to allow for robust identification of all parameters of the proposed model, at least not in a unique manner. For illustration, we performed an identification on the specimen presented in Figure 37, where the only measurements are those for a force-displacement diagram, which is the usual type of results obtained by real experiments. We show that in such a case even the elastic parameters can not be fully identified. Namely, the updated probability distribution of the shear modulus indeed moves towards the deterministic value, but all updates for the bulk modulus stay only close to the prior. As for the other two parameters we identified, the distribution of the yield stress remains unchanged compared to the prior, while the distribution of the angle of internal friction moves towards the deterministic value, but only after the third plastic step. This clearly illustrates the need for more elaborate measurements in the standard tests, or using the computational results obtained by the presented meso-scale model to provide a very robust identification.

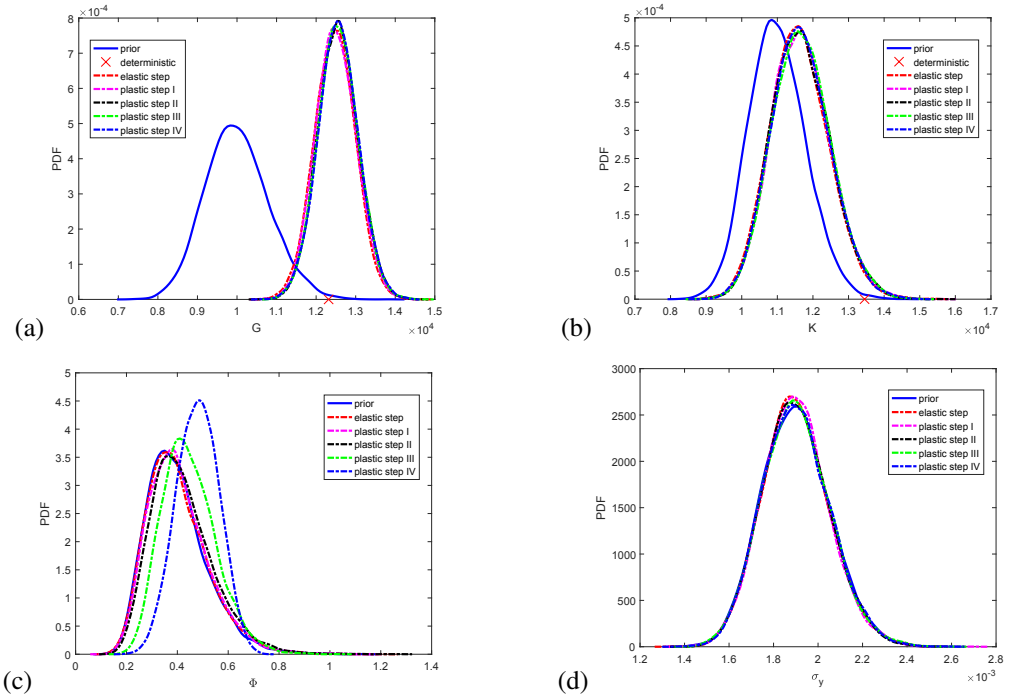

Figure 37: Updates for elastic and hardening parameters performed simultaneously on a uniaxial compression test with measurement of the force-displacement diagram

If the model does not offer a clear split between the groups of parameters controlling different response phases (e.g. micro-plane model of concrete [44]), one has to use an alternative approach in which the identification of all macro-scale model parameters and their probability distributions are computed simultaneously. The first difficulty with such an approach is its excessive computational cost. Namely, the simultaneous identification of all parameters requires the computation of a proxy model for eight parameters in 4^8 integration points for third order polynomials (if p is the polynomial order and N is the problem dimension, then number of integration points is equal to $(p+1)^N$). Such an identification would be very expensive computationally, resulting with days of computations.

For the sake of illustration, we here perform the identification by using a proxy model with four parameters, which still requires a considerable computations with 4^4 integration points for third polynomial order. More precisely, we perform computations for three different groups of parameters where the elastic parameters are simultaneously identified with either the yield stress and the angle of internal friction in the first group, or with the hardening parameter and the angle of internal dilatancy in the second group, or yet with the limit stress and the fracture energy release rate in compression in the third group.

The usual measurements of force-displacement diagrams would not be sufficient to carry out any such identification procedure. Thus, one needs to complement these measurement with computational results, or 'measurements'. In particular, in the elastic stage we take one measurement of the elastic energy, in hardening we take four measurements of the plastic dissipations along with volumetric strain, while in the softening stage we take measurements of the limit stress as well as measurements of the total energy in two arbitrary steps. All these 'measurements' are made in fact by using the meso-scale model computations. The results for the corresponding updates of the distributions of elastic and plastic parameters are presented in Figure 38.

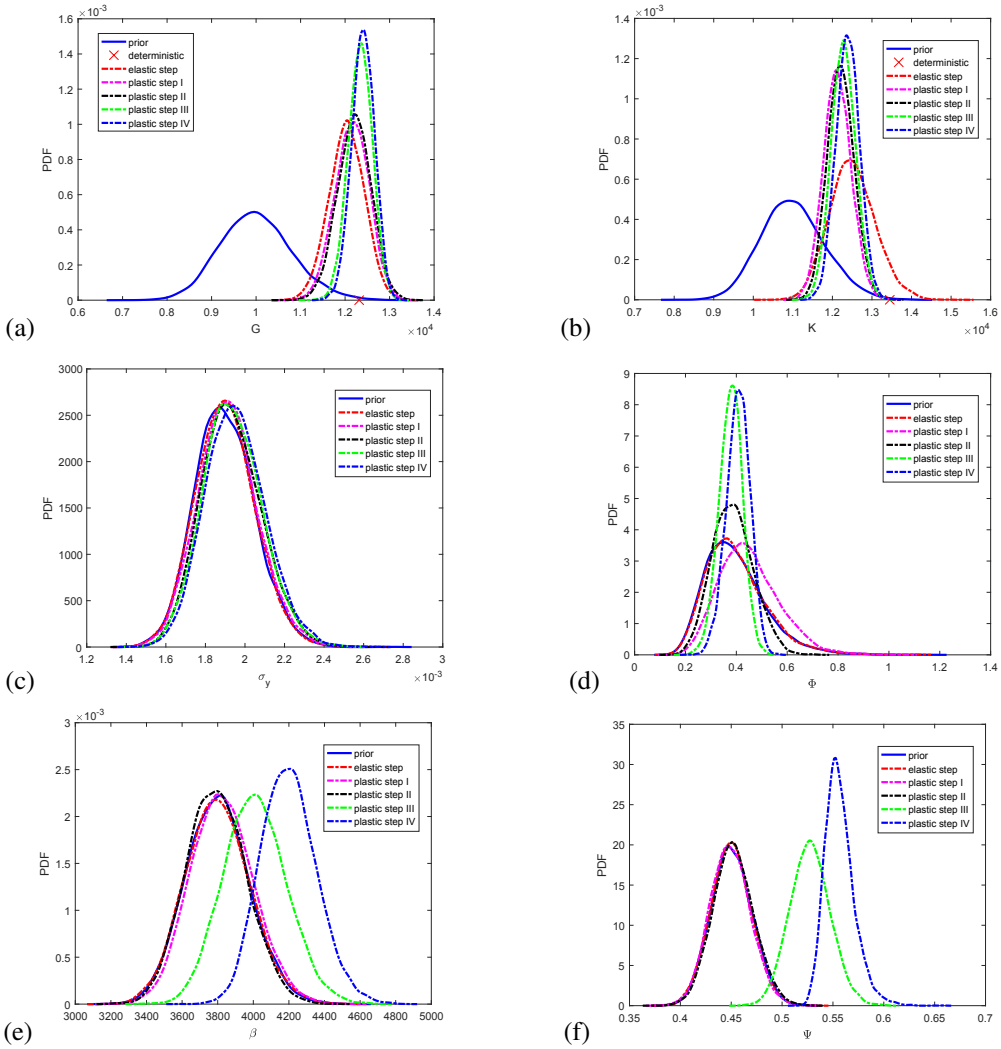

Figure 38: Updates for elastic and plastic parameters performed simultaneously on a uniaxial compression test

One may note in Figure 38a and Figure 38b that the prior knowledge about the elastic parameters is moved to the deterministic value after the elastic step, while subsequent measurements taken in the hardening stage would no longer

move their distribution towards the deterministic value. This indicates that the elastic parameters can be identified by only using the measurements made in the elastic response stage. Moreover, one may see from Figure 38 that the elastic measurements do not change the prior knowledge about plastic parameters. Namely, the identification of the yield stress and angle of internal friction can not be performed only with uniaxial compression test measurements (Figure 38c and Figure 38d). The measurements that are taken at a later stage of hardening provide much more information about the angle of internal dilatancy and the hardening parameter than any measurement made at an early stage. Similarly, from Figure 39 one may glean that the elastic measurements do not affect the prior knowledge about the softening parameters (e.g. see Figure 39a-b).

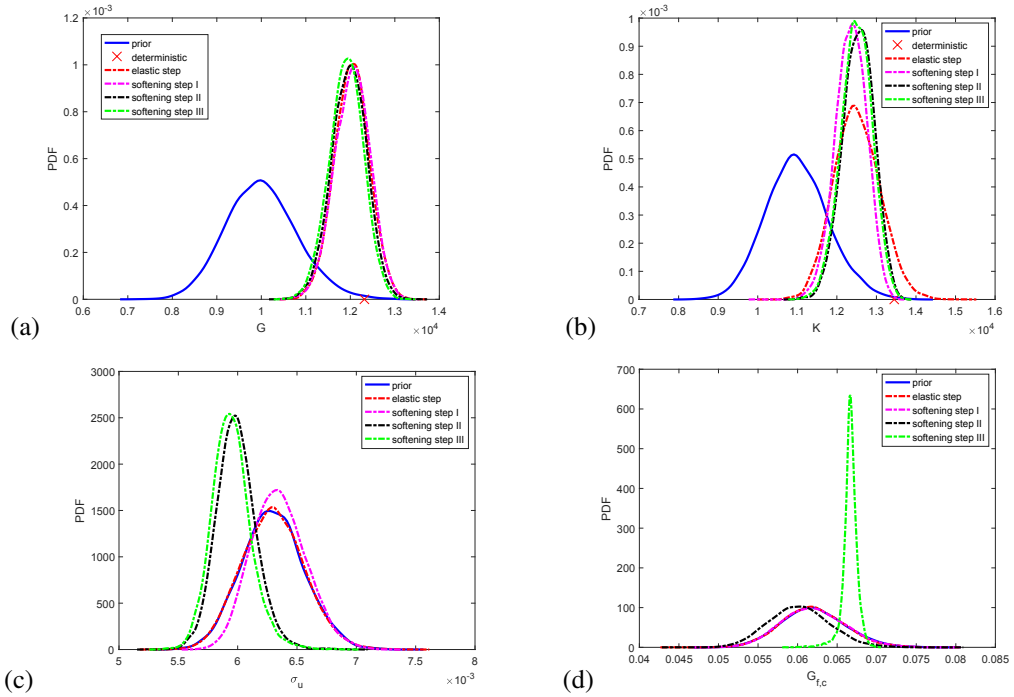

Figure 39: Updates for elastic and softening parameters performed simultaneously on a uniaxial compression test

The final parameter identification attempt is here carried out with a group of six parameters that consists of two hardening parameters in compression, the hardening parameter and the angle of internal dilatancy in shear, and two softening parameters. Again we find that the measurements made in the softening stage do not provide any additional information neither about the elastic parameters, nor about the hardening parameters. In Figure 40a-b, as well as in Figure 40c and Figure 40d, one may find that the measurements in the hardening stage are irrelevant for the softening parameters. In such a case, a reduced computational cost of splitting the parameter identification produces the same results as with the simultaneous computations of all parameters. This fully confirms the interest of the identification procedure split which we used in the previous examples. The CPU times are gathered in Table 8 in order to illustrate a significant gain in computational efficiency for proposed PCKF Bayesian updates, especially when combined with the identification procedure split. Furthermore, the overall cost reduction and efficiency gain in switching to reduced model proposed herein can be quantified with the results listed in Table 9, where we compare CPU times for meso-scale and macro-scale computations for typical realizations.

test type	RV	CPU time (seconds) PC - 1		PC - 2*	
		MCMC	PCEKF	MCMC	PCEKF
simple shear hydrostatic compression uniaxial compression uniaxial tension	G/K	1.6E+04	2.5	2461.5	1.0
uni/biaxial compression	$\sigma_y/tan(\phi)$	-	5.0	-	1.5
uni/biaxial compression	$\beta/tan(\psi)$	-	40.0	-	7.0
uniaxial tension	$\sigma_u/G_{f,t}$	-	24.3	-	4.3
uniaxial compression	$\sigma_u/G_{f,c}$	-	76.0	-	11.7

Table 8: Computation time for different type of tests; * PC-1 - Processor: Intel(R) Core(TM) i5-5200U CPU @ 2.20GHz, RAM: 4.0 GB, PC-2 - Processor: Intel(R) Xeon(R) W-2123 CPU @ 3.60GHz, RAM: 32.0 GB.

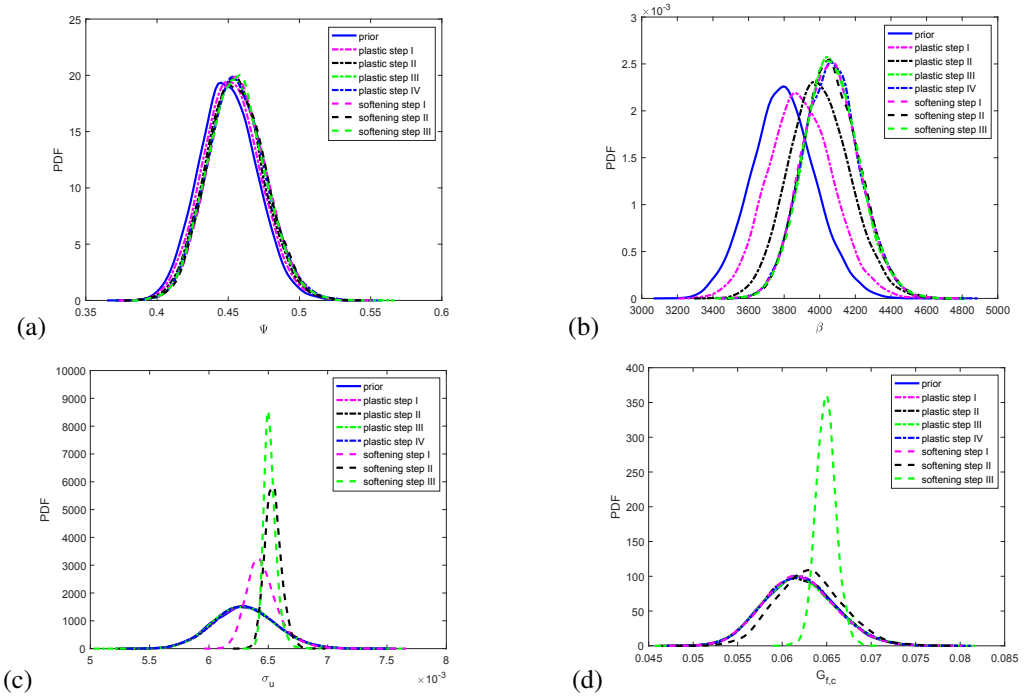

Figure 40: Updates for hardening and softening parameters performed simultaneously on a uniaxial compression test

test type	response stage	CPU time (seconds) / PC - 1	
		meso-scale model	macro-scale model
simple shear	elastic (2 steps)	4.01	0.02
hydrost. compression	elastic (2 steps)	5.62	0.05
uniaxial tension	elastic + softening	2264.35	0.97
uniaxial compression	elastic + hardening + softening	4419.80	3.04

Table 9: CPU time for meso-scale and macro-scale model performed for different type of tests

6. Conclusions

In this paper we propose a reduced stochastic macro-scale model for concrete, where each particular realization combines multi-surface plasticity criteria for the fracture process zone with the embedded-discontinuity finite element localized failure criteria. The proposed model can better reproduce the behavior in complete failure of massive structures by taking into account different types of dissipative mechanisms: a bulk dissipation characterized by the development of micro-cracks (by using the Drucker-Prager citerion with a non-associative flow rule), and a surface dissipation in localization zones in terms of macro-cracks (with the St. Venant plasticity criterion). The main advantage of such 'multi-surface plasticity' model is in its ability to represent the complete set of global 3D failure modes for concrete in tension, compression, or shear. Another advantage of the proposed model is in the solid physical basis of its parameters with ability to represent three different stages of failure process in compression, with initial elastic behavior, followed by plastic hardening, and finally by localized softening behavior, whereas in tension it is sufficient to take the elastic stage followed by the unstable softening response. We note that all such elaborate features have to be combined in a single macro-scale model in order to provide the best possible match with the capabilities of fine, meso-scale models of concrete, presented in Part I [41].

In order to quantify the loss of information of scale coarsening in bridging the scales from meso- to macro-scale, we account for the crucial role of uncertainties at both scales. Namely, the model parameters at the meso-scale are here considered as random fields, used to describe the cement-aggregate interface parameters' probability distributions. Moreover, the macro-scale model is also one of stochastic plasticity, with parameters considered as random variables. We used the Bayesian inference to compensate for the model reduction and scale coarsening, by computing probability distributions of macro-scale model parameters, which can provide better predictive properties to such models for any choice of plasticity criteria (and not only those used herein). As shown here, the information that renders efficiency to such Bayesian updates can be obtained from simulation results performed with the meso-scale model for concrete with parameters expressed as random fields. The meso-scale simulation results serve for constructing the reduced model by scale-coarsening approach, by replacing in standard Bayesian inference the experimental measurements that can be obtained through tomography (e.g. digital image correlation or digital volume correlation). The latter cannot easily be performed for a large size specimen, such as those used in testing of concrete, and thus the proposed use of meso-scale simulations is often the only alternative. The most significant finding on the proposed Bayesian inference updates, which are used for computing the macro-scale model parameters' probability distributions, is in its computational efficiency obtained with the sound choice of the macro-scale parameters that directly control intrinsic deformation modes — e.g. bulk and shear moduli as opposed to Young's modulus and Poisson's ratio — as well as the strain energy functional as QoI for measurement in elastic phase.

Similar finding holds for plastic hardening and softening phase, where the sound choice for QoI concerns, respectively, the plastic dissipations in FPZ and in softening. The reduced macro-scale model for concrete will have local (point-wise) multi-surface plasticity criteria for the fracture process zone, along with the embedded-discontinuity finite element localized failure criteria, with all macro-scale model parameters defined as random variables. The scale bridging allows to obtain their probability distributions by considering the sources of uncertainty both at meso-scale and at macro-scale, i.e. both initial and induced defects in the failure process, resulting in multiplicative format of RVs. The latter provides the computational efficiency of the proposed stochastic scale coarsening. Namely, the particular choice of Voronoi cell discretization results in rather limited number of sources of uncertainty at meso-scale,

which can be expressed in terms of random fields, and further transferred by the KLE into uncorrelated Gaussian random variables, which renders the stochastic Galerkin approach feasible.

The computational cost at macro-scale required for constructing probability distributions in terms of Bayesian updates is controlled as follows. Two different methods for Bayesian inference have been tested and compared in the proposed approach that allows incorporating new information generated in a particular loading program. The first method — Markov Chain Monte Carlo (MCMC) — updates the measure, whereas the second method — Polynomial Chaos Expansion Kalman Filter (PCKF) updates the random variable. We carried out various numerical tests and show that when the identification approach is split into three stages, this leads to not only substantial computational savings, but also provides more reliable results. We confirm that posterior distributions of elastic parameters are the same for both methods, as well as for different choice of the cost function or measurements (with either energy, dissipation or applied force). We propose an identification procedure for loading program corresponding to the tests which are not difficult to set in a laboratory environment, like a uniaxial compression test. We observe that such kind of test favors the shear modulus due to restrained lateral displacements corresponding to higher friction between the load plates and the specimen. Hardening parameters which characterize the behavior of concrete in compression are identified in two steps. First one for the parameters which define the yield function, and second one for the parameters which define the plastic potential function. We show that local measurements of volumetric strain provide essential information about the angle of internal dilatancy. The measurement of ultimate stress on a reference curve along with the total energy is sufficient to obtain the posterior distribution of softening parameters. We also find that the limit stress and the fracture energy release rate varies more in compression than in tension.

Our current work pertains to extending the proposed approach to short fiber reinforced concrete [78] and reinforced concrete structures [35], in order to obtain the probability distribution of parameters controlling the structure durability, such as crack spacing and opening. Future work will also target the probability distribution of cyclic behavior of concrete under dynamic loads by using as a starting point our coupled damage-plasticity model [38].

Acknowledgements: This work was supported jointly by ANR and DFG (project SELF-TUM). AI was also supported by IUF-Institut Universitaire de France, as well as Haut-de-France Region (CR Picardie 120-2015-RDISTRUCT-000010) and EU funding (FEDER) for Chaire-de-Mecanique. This support is gratefully acknowledged.

[1] Arnst M., C. Soize, and R. Ghanem, Hybrid Sampling/Spectral Method for Solving Stochastic Coupled Problems, SIAM/ASA J. Uncertainty Quantification, 1, 218–243, (2013). doi: 10.1137/120894403

[2] Arnst M., R. Ghanem, C. Soize, Identification of Bayesian posteriors for coefficients of chaos expansions, Journal of Computational Physics, 229, 3134–3154, (2010. doi: 10.1016/j.jcp.2009.12.033

[3] Bazant Z.P., Probability distribution of energetic-statistical size effect in quasit-brittle failure, Prob. Eng. Mech., 19, 307–319, (2004)

[4] Belytschko T., J.-H. Song, Coarse-graining of multiscale crack propagation, Int. J. Numer. Meth. Engng., 81, 537–563, (2010)

[5] Benkemoun N., M. Hautefeuille, J.-B. Colliat and A. Ibrahimbegovic, Failure of heterogeneous materials: 3D meso-scale FE models with embedded discontinuities, Int. J. Numer. Methods Eng., 82, 1671–1688, (2010)

[6] Bentz, D.P., CEMHYD3D: A three-dimensional cement hydration and microstructure development modeling package. version 3.0., (2005)

[7] Bobrowski A., Functional Analysis for Probability and Stochastic Processes, Cambridge University Press, Cambridge, 2005.

[8] Boyard S., C. Lebris, T. Lelievre, Y. Madey, Reduced basis techniques for stochastic problems, Arch. Comput. Methods Eng., 17, 435–454, (2010)

[9] Chinesta F., P. Ladeveze, A. Ammar, E. Cueto, A. Nouy, Proper Generalized Decomposition in Extreme Simulations, IACM Expressions, 26, 1–6, (2009)

[10] Clément A., C. Soize, J. Yvonnet, Uncertainty quantification in computational stochastic multiscale analysis of nonlinear elastic materials, Comput. Methods Appl. Mech. Engrg., 254, 61–82, (2013). doi: 10.1016/j.cma.2012.10.016

[11] Das S., R. Ghanem, J. Spall, Asymptotic sampling distribution for polynomial chaos representation of data : A maximum-entropy and fisher information approach, SIAM Journal on Scientific Computing 30(5), 2207–2234, (2008).

[12] Delaplace A., A. Ibrahimbegovic, Performance of time-stepping schemes for discrete models in fracture dynamic analysis, Int. J. Numer. Meth. Engng., 65, 1527–1544, (2006)

[13] Dolgov S., B. N. Khoromskij, A. Litvinenko, H. G. Matthies, Polynomial Chaos Expansion of random coefficients and the solution of stochastic partial differential equations in the Tensor Train format. SIAM/ASA Journal on Uncertainty Quantification 3, 1109–1135, (2015). doi: 10.1137/140972536

[14] Eigel M., C. Gittelson, Ch. Schwab, E. Zander, Adaptive stochastic Galerkin FE, Comput. Methods Appl. Mech. Eng., 270, 247–269, (2014)

[15] Engl H. W., Groetsch C. W., Inverse and Ill-Posed Problems, Academic Press, New York, NY, 1987.

[16] Engl H. W. , Hanke M. , Neubauer A., Regularization of inverse problems, Kluwer, Dordrecht, 2000.

[17] Espig M., W. Hackbusch, A. Litvinenko, H. G. Matthies, Ph. Wähnert, Efficient low-rank approximation of the stochastic Galerkin matrix in tensor formats, Computers & Mathematics with Applications, 67, 818–829, (2014). doi: 10.1016/j.camwa.2012.10.008

[18] Eu B.C., Nonequilibrium Statistical Mechanics: Ensemble Method, Springer, Berlin, 1998

[19] Evensen G., Data Assimilation, The Ensemble Kalman Filter. Springer, Berlin, 2007.

[20] Evensen G., The ensemble Kalman filter for combined state and parameter estimation, IEEE Control Systems Magazine 29, 82–104, (2009).

[21] Gamerman D, H. F. Lopes, Markov Chain Monte Carlo: Stochastic Simulation for Bayesian Inference, Chapman & Hall, Boca Raton, FL, 2006.
[22] Ghavamian Sh., I. Carol, A. Delaplace, Modèles de fissuration de béton : projet MECA, Revue française de génie civil, 7, 543–581, 2003
[23] Gilks W. R. , S. Richardson, D. Spiegelhalter, Markov Chain Monte Carlo in Practice, Chapman & Hall, Boca Raton, FL, 1995.
[24] Goldstein M. , D. Wooff, Bayes linear statistics, Wiley Series in Probability and Statistics, John Wiley & Sons, Chichester, 2007.
[25] Graham-Brady L. L., S. R. Arwade, D. J. Corr, M. A. Gutirrez, D. Breysse, M. Grigoriu, N. Zabaras, Probability and materials: from nano-to macro-scale: a summary. Probabilistic Engineering Mechanics, 21, 193–199, (2006). doi: 10.1016/j.probengmech.2005.10.005
[26] Hautefeuille M., J.-B. Colliat, A. Ibrahimbegović, H. G. Matthies, Multiscale Zoom Capabilities for Damage Assessment in Structures, In: A. Ibrahimbegović, M. Zlatar (eds.), Damage Assessment and Reconstruction after Natural Desasters and Previous Military Activities, NATO-ARW series. Springer, Berlin, 2008.
[27] Hautefeuille M., J.-B. Colliat, A. Ibrahimbegović, H. G. Matthies, P. Villon, A multi-scale approach to model localized failure with softening. Computers & Structures 94–95, 83–95, (2012). doi: 10.1016/j.compstruc.2011.11.007
[28] Hofstetter G., H. A. Mang, Computational Mechanics of Reinforced Concrete Structures, Vieweg, (1995) ISBN-10: 3528063904
[29] Ibrahimbegovic A., H. C. Chen, E. L. Wilson, R. L. Taylor, Ritz Method for Dynamic Analysis of Linear Systems with Non-Proportional Damping, Int. J. Earthquake Engng. Structural Dynamics, 19, 877–889, (1990)
[30] Ibrahimbegovic A., E. L. Wilson, A modified method of incompatible modes, Commun Appl Numer Method 7, 187–194, (1991)
[31] Ibrahimbegovic A., D. Markovič, Strong coupling methods in multi-phase and multi-scale modeling of inelastic behavior of heterogeneous structures, Computer Methods in Applied Mechanics and Engineering, 192, 3089–3107, (2003)
[32] Ibrahimbegovic A., D. Brancherie, Combined hardening and softening constitutive model for plasticity: precursor to shear slip line failure, Computational Mechanics, 31, 88–100 (2003)
[33] Ibrahimbegovic A., S. Melnyk, 'Embedded discontinuity finite element method for modeling of localized failure in heterogeneous materials with structured mesh: an alternative to extended finite element method', Comput. Mech., 40, 149–155 (2007)
[34] Ibrahimbegovic A., Nonlinear Solid Mechanics: Theoretical Formulations and Finite Element Solution Methods, Springer, London, (2009). ISBN 978-9958-638-23-7
[35] Ibrahimbegovic A., A. Boulkertous, L. Davenne, D. Brancherie, Modelling of reinforced-concrete structures providing crack-spacing based on X-FEM, ED-FEM and novel operator split solution procedure, Int. J. Numer. Meth. Engng., 83, 452–481 (2010)
[36] Ibrahimbegovic A., H. G. Matthies, Probabilistic Multiscale Analysis of Inelastic Localized Failure in Solid Mechanics, Computer Assisted Methods in Engineering and Science, 19, 277–304, (2012)
[37] Janson S., Gaussian Hilbert spaces, Cambridge University Press, Cambridge, 1997.
[38] Jehel P., L. Davenne, A. Ibrahimbegovic, P. Lger, Towards robust viscoelastic-plastic-damage material model with different hardenings/softenings capable of representing salient phenomena in seismic loading applications, Computers and Concrete, 7(4), 365–386, (2010)
[39] Jirasek M., T. Zimmerman, Embedded crack model. Part II: Combination with smeared cracks, Int. J. Numer. Meth. Engng., 50, 1291–1305, (2001)
[40] Kálmán R. E., A new approach to linear filtering and prediction problems, Transactions of the ASME — J. of Basic Engineering (Series D) 82, 35–45, (1960).
[41] Karavelić E., M. Nikolić, A. Ibrahimbegovic, A. Kurtović, Concrete meso-scale model with full set of 3D failure modes with random distribution of aggregate and cement phase. Part I: Formulation and numerical implementation, Comp. Methods Appl. Mech. Eng., 344, 1051–1072, (2019)
[42] Karavelić E., A. Ibrahimbegovic, S. Dolarević, Multi-surface plasticity model for concrete with 3D hardening/softening failure modes for tension, compression and shear, Computers and Structures, 221, 74–90, (2019)
[43] Kučerová A., D. Brancherie, A. Ibrahimbegovic, J. Zeman, Z. Bittnar, Novel anisotropic continuum-discrete damage model capable of representing localized failure of massive structures. Part II: identification from tests under heterogeneous stress field, International Journal of Engineering Computations, 26, 128–144 (2009)
[44] Kučerová A., M. Leps, Soft computing-based calibration of microplane M4 model parameters: Methodology and validation, Advances in Engineering Software 72, pp. 226–235, (2014)
[45] Ladevèze P., G. Puél, T. Romeuf, Lack of knowledge in structural model validation, Comput. Methods Appl. Mech. Eng., vol. 197, pp. 4697–4710, (2006)
[46] Ladevèze P., D. Néron, Model Order Reduction for nonlinear problems involving complex time-varying loadings, Proceedings ECCM-ECFD, 6th European Conf. Comp. Solid Mech. 7th European Conf. Comp. Fluid Dynamics, 11–15 June, (2018)
[47] Lamón J., Ceramics reliability: Statistical analysis of multiaxial failure using Weibull approach and the multiaxial elemental strength model, Compos. Sci. Tech., 69, 1607–1614, (2009)
[48] Larsson F., F. Fritzen, On goal-oriented error estimation for model order reduction in computational homogenization of hyperelastic microstructures, Proceedings ECCM-ECFD, 6th European Conf. Comp. Solid Mech. 7th European Conf. Comp. Fluid Dynamics, 11–15 June, (2018)
[49] Lura P., J. Couch, O. M. Jensen, J. Weiss, Early-age acoustic emission measurements in hydrating cement paste: Evidence for cavitation during solidification due to self-desiccation, Cement and Concrete Research 39, 861–867, (2009)
[50] Le Maître O. P., O. M. Knio, Spectral methods for uncertainty quantification, Scientific Computation, Springer, Berlin, (2010)
[51] Lions J.-L., Asymptotic calculus of variations, Academic Press, (1980)
[52] Luenberger D. G., Optimization by Vector Space Methods, John Wiley & Sons, Chichester, 1969.
[53] Madras N., Lectures on Monte Carlo Methods, American Mathematical Society, Providence, RI, 2002
[54] Marzouk Y.M., H. N. Najm, L. A. Rahn, Stochastic spectral methods for efficient Bayesian solution of inverse problems, Journal of Computational Physics, 224, 560–586, (2007)
[55] Matthies H. G., Uncertainty quantification with stochastic finite elements, in (E. Stein et al. eds.), Encyclopedia Comp. Mechanics, Wiley. Ch.44, 1–70, (2007)
[56] Matthies H. G., A. Ibrahimbegović, Stochastic Multiscale Coupling of Inelastic Processes in Solid Mechanics, In: M. Papadrakakis, G.

Stefanou (eds.), Multiscale Modelling and Uncertainty Quantification of Materials and Structures, 3, 135–157, (2014). Springer, Berlin. doi: 10.1007/978-3-319-06331-7_9

[57] Matthies H. G., E. Zander, B. V. Rosić, A. Litvinenko, O. Pajonk, Inverse problems in a Bayesian setting, in: A. Ibrahimbegovic (Ed.), Computational Methods for Solids and Fluids - Multiscale Analysis, Probability Aspects, and Model Reduction, Vol. 41 of Computational Methods in Applied Sciences, Springer, Berlin, 2016, pp. 245–286. doi: 10.1007/978-3-319-27996-1

[58] Matthies H. G., E. Zander, B. V. Rosić, A. Litvinenko, Parameter estimation via conditional expectation: a Bayesian inversion, Advanced Modeling and Simulation in Engineering Sciences 3, 24, (2016). doi:10.1186/s40323-016-0075-7

[59] Matthies H. G., A. Litvinenko, B. V. Rosić, E. Zander, Bayesian parameter estimation via filtering and functional approximations, arXiv: 1611.09293 [math.NA] (2016). URL http://arxiv.org/abs/1611.09293

[60] Matthies H. G., E. Zander, Solving stochastic systems with low-rank tensor compression. Linear Algebra and its Applications 436, 3819–3838, (2012) doi: 10.1016/j.laa.2011.04.017

[61] Meschke G., B. Pichler, J. G. Rots (eds.), Computational modeling of concrete structures, CRC Press, pp. 1–1034, (2018), ISBN 9781138741171

[62] Metropolis N, A. W. Rosenbluth, M. N. Rosenbluth, A. H. Teller, E. Teller, Equation of state calculations by fast computing machines, Journal of Chemical Physics 21, 1087–1092, (1953). doi:10.1063/1.1699114.

[63] Moes N., T. Belytschko, Extended finite element method for cohesive crack growth, Engineering fracture mechanics 69, 813-833, (2002)

[64] Nagel J.B., B. Sudret, A unified framework for multilevel uncertainty quantification in Bayesian inverse problems, Probabilistic Engineering Mechanics, 43, 68–84, (2016)

[65] Nikolić M., X. N. Do, A. Ibrahimbegovic, Ž. Nikolić, Crack propagation in dynamics by embedded strong discontinuity approach: Enhanced solid versus discrete lattice model, Comp. Methods Appl. Mech. Eng., 340, 480–499, (2018)

[66] Nouy A., A priori model reduction through Proper Generalized Decomposition for solving time-dependent partial differential equations, Comp. Meth. Appl. Mech. Eng., 199, 1603–1623, (2010)

[67] Pajonk O., B. V. Rosić, A. Litvinenko, H. G. Matthies, A deterministic filter for non-Gaussian state estimation, Proc. Appl. Math. and Mech. (PAMM) 11, 703–704, (2011). doi: 10.1002/pamm.201110341

[68] Pajonk O., B. V. Rosić, A. Litvinenko, H. G. Matthies, A deterministic filter for non-Gaussian Bayesian estimation — applications to dynamical system estimation with noisy measurements. Physica D: Nonlinear Phenomena 241, 775–788, (2012). doi: 10.1016/j.physd.2012.01.001

[69] Pajonk O., B. V. Rosić, H. G. Matthies, Sampling-free linear Bayesian updating of model state and parameters using a square root approach, Computers & Geosciences, 55, 70–83, (2013). doi: 10.1016/j.cageo.2012.05.017

[70] Parlett B. N., The Symmetric Eigenvalue Problem, SIAM Classics in Applied Mathematics, (1998). doi: 10.1137/1.9781611971163

[71] Perrin G., C. Soize, D. Duhamel, C. Fünfschilling, Identification of polynomial chaos representations in high dimensions from a set of realizations, SIAM J. Sci. Comput., 34(6), A2917–A2945, (2012). doi: 10.1137/11084950X

[72] Rao M. M., Conditional Measures and Applications, CRC Press, Boca Raton, FL, (2005).

[73] Rhudy, M., Y. Gu, J. Gross, M. R. Napolitano, Evaluation of Matrix Square Root Operations for UKF within a UAV-Based GPS/INS Sensor Fusion Application, Int. Journal of Navigation and Observation, 2011, 1–11, (2011). doi: 10.1155/2011/416828

[74] Rosić, B V., A. Litvinenko, O. Pajonk, H. G. Matthies, Sampling-free linear Bayesian update of polynomial chaos representations, J. Comp. Phys. 231, 5761–5787, (2012). doi: 10.1016/j.jcp.2012.04.044

[75] Rosić B. V. , A. Kučerová, J. Sýkora, O. Pajonk, A. Litvinenko, H. G. Matthies, Parameter identification in a probabilistic setting, Engineering Structures 50, 179–196, (2013). doi: 10.1016/j.engstruct.2012.12.029

[76] Rosić B. V. , J. Sýkora J., O. Pajonk, A. Kučerová, H. G. Matthies, Comparison of numerical approaches to Bayesian updating, in: A. Ibrahimbegovic (Ed.), Computational Methods for Solids and Fluids- Multiscale Analysis, Probability Aspects, and Model Reduction, Vol. 41 of Computational Methods in Applied Sciences, Springer, Berlin, (2016), pp. 427–461. doi: 10.1007/978-3-319-27996-1

[77] Rosić B. V., M. S. Sarfaraz, H. G. Matthies, and A. Ibrahimbegović, Stochastic upscaling of random microstructures, PAMM 17, 869–870, (2017), doi: 10.1002/pamm.201710401.

[78] Rukavina T., A. Ibrahimbegovic, I. Kožar, Fiber-reinforced brittle material fracture models capable of capturing a complete set of failure modes including fiber pull-out, Comput. Methods Appl. Mech. Engrg. 355, 157–192, (2019)

[79] Sa De C., N. Benkemoun, J.-B. Colliat, F. Benboudjema, Modélisation à l'échelle méso-scopique du comportement hydro-mécanique des matériaux à matrice cimentaire, Proceedings colloque du CSMA, Giens, (2009)

[80] Sanchez-Palencia E., Non homogeneous media and vibration theory. Lecture notes in physics, Springer, (1980)

[81] Sarfaraz M. S., B. Rosić, H. G. Matthies, Stochastic upscaling of heterogeneous materials, PAMM 16, 679–680, (2016), doi: 10.1002/pamm.201610328.

[82] Sarfaraz M. S., B. V. Rosić, H. G. Matthies, A. Ibrahimbegović, Stochastic upscaling via linear Bayesian updating, Coupled Systems Mechanics, 7(2), 211–232, (2018). doi: 10.12989/csm.2018.7.2.211

[83] Sarfaraz M. S., B. V. Rosić, H. G. Matthies, A. Ibrahimbegović, Stochastic Upscaling via Linear Bayesian Updating, in: Multiscale Modeling of Heterogeneous Structures (J. Sorić, P. Wriggers, and O. Allix, eds.), Lecture Notes in Applied and Computational Mechanics, vol. 86, Springer, pp. 163–181, (2018), doi: 10.1007/978-3-319-65463-8_9.

[84] Sarfaraz M. S., B. Rosić, H. G. Matthies, A. Ibrahimbegović, Bayesian stochastic multi-scale analysis via energy considerations, arXiv: 1912.03108 [math.ST] (2019). url: https://arxiv.org/abs/1912.03108

[85] Schillings C., A. M. Stuart, Analysis of the ensemble Kalman filter for inverse problems, SIAM Journal on Numerical Analysis 53(3), 1264–1290, (2017). doi: 10.1137/16M105959X

[86] Shell M.S., The relative entropy is fundamental to multiscale and inverse thermodynamic problems, J. Chem. Phys. 129(14), 114108, (2008)

[87] Shinozuka, M., M. Feng, J. Lee, T. Naganuma. Statistical Analysis of Fragility Curves, J. Eng. Mech., 126, 1224–1231, (2000)

[88] Simo J. C., J. Oliver, F. Armero, An analysis of strong discontinuities induced by strain-softening in rate-independent inelastic solids. Computational Mechanics, 12, 277–296, (1993)

[89] Skliar M., W. F. Ramirez, Square Root Implicit Kalman Filtering, IFAC Proceedings Volumes, 29(1), 4676–4681, (1996). doi: 10.1016/S1474-6670(17)58420-7

[90] Smith R. C., Uncertainty Quantification: Theory, Implementation, and Applications, Vol. 12 of Computational Science & Engineering, SIAM, Philadelphia, PA, (2014)
[91] Soize C., Identification of high-dimension polynomial chaos expansions with random coefficients for non-Gaussian tensor-valued random fields using partial and limited experimental data, Comput. Methods Appl. Mech. Engrg., 199, 2150–2164, (2010). doi: 10.1016/j.cma.2010.03.013
[92] Soize C., A computational inverse method for identification of non-Gaussian random fields using the Bayesian approach in very high dimension, Comput. Methods Appl. Mech. Engrg., 200, 3083–3099, (2011).
[93] Stefanou G., M. Georgiudakis, M. Papadrakakis, Sequentially linear analysis of structures with stochastic material properties, in M. Papadrakakis, G. Stefanou (eds.) 'Multiscale Modeling and Uncertainty Quantification of Materials and Structures', Springer, pp. 19–39, (2014)
[94] Tarantola A., Inverse Problem Theory and Methods for Model Parameter Estimation, SIAM, Philadelphia, PA, (2005)
[95] Terada K., N. Kikuchi, A class of general algorithms for multi-scale analysis of heterogeneous media, Comput. Methods Appl. Mech. Engrg., 190, 5427–5464, (2001).
[96] Thornton C. L., Triangular covariance factorizations for Kalman filtering, PhD thesis, Caltech, JPL — NASA Tech. Memorandum 33-798, (1976). url: https://ntrs.nasa.gov/archive/nasa/casi.ntrs.nasa.gov/19770005172.pdf
[97] Wähnert Ph., A. Litvinenko, M. Espig, H. G. Matthies, W. Hackbusch, Approximation of the stochastic Galerkin matrix in the low-rank canonical tensor format, Proc. Appl. Math. and Mech. (PAMM) 12, 785–788, (2012). doi: 10.1002/pamm.201210380
[98] Wriggers P., S. O. Moftah, Mesoscale models for concrete: Homogenisation and damage behaviour, Finite Elements in Analysis and Design, 42(7), 623–636, (2006). doi: 10.1016/j.finel.2005.11.008
[99] Wriggers P., M. Hain, Material Characterization Based on Micro-Structural Computations and Homogenization. In: Reddy B.D. (eds) IUTAM Symposium on Theoretical, Computational and Modelling Aspects of Inelastic Media. IUTAM BookSeries, vol 11. Springer, Dordrecht, (2008)
[100] Xiu D., Numerical methods for stochastic computations: a spectral method approach, Princeton University Press, Princeton, NJ, (2010)
[101] Xiu D., G. E. Karniadakis, The Wiener-Askey polynomial chaos for stochastic differential equations, SIAM Journal of Scientific Computing 24, 619–644, (2002)
[102] Zienkiewicz O. C., R. L. Taylor, The Finite Element Method, Elsevier, Amsterdam, (2005)
[103] Zohdi T. I., P. Wriggers, An introduction to computational micromechanics, Springer, Berlin, (2008)
[104] Zohdi T. I., Homogenization Methods and Multiscale Modeling, In: Encyclopedia of Computational Mechanics, Second Edition, (eds E. Stein, R. Borst and T.J.R. Hughes), Wiley, (2017) doi: 10.1002/9781119176817.ecm2034